Molecular Photoacoustic Contrast Agents (MPACs):Design Principles & Applications

Raymond E. Borg and **DR. Jonathan Rochford**[*]

Department of Chemistry, University of Massachusetts Boston, 100 Morrissey Boulevard, Boston, MA 02125.

Abstract

Photoacoustic imaging (PAI) is a rapidly growing field which offers high spatial resolution and high contrast for deep-tissue imaging in vivo. PAI is non-ionizing, non-invasive and combines the optical resolution of fluorescence imaging with the spatial resolution of ultrasound imaging. In particular, the development of exogenous PA contrast agents has gained significant momentum of late with a vastly expanding complexity of dye materials under investigation ranging from small molecules, to macromolecular proteins, polymeric and inorganic nanoparticles. The goal of this review is to survey the current state-of-the-art in *molecular photoacoustic contrast agents* (MPACs) for applications in biomedical imaging. The fundamental design principles of MPACs is presented and a review of prior reports spanning from early-to-current literature is put forth.

Graphical Abstract
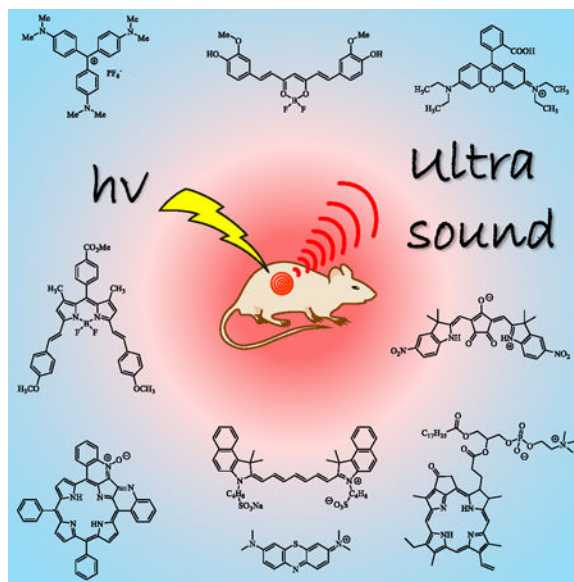
The development of exogenous PA contrast agents has gained significant momentum of late with a vastly expanding complexity of dye materials under investigation. The goal of this review is to survey the current state-of-the-art in *molecular photoacoustic contrast agents* (MPACs) for

[*]Corresponding author's: Jonathan.Rochford@umb.edu (Jonathan Rochford).

applications in biomedical imaging. The fundamental design principles of MPACs is presented and a review of prior reports spanning from early-to-current literature is put forth.

INTRODUCTION

The conversion of light energy into acoustic waves, known as the photoacoustic (PA) effect was first reported by Alexander Graham Bell in 1880 while investigating ways to communicate over long distances (1). Interest in the PA effect has experienced a great resurgence of late due to its advancement of application in biomedical imaging (2–16). The first application of the PA effect in biomedical imaging can be traced back to a 1974 study by Lemons et al. who developed a scanning acoustic microscopy (SAM) technique for cell imaging with a resolution of close to 1 μm using ultrasound frequencies of 1500 MHz in water (17). PAI is similar to SAM in that it uses an ultrasound transducer to detect the acoustic waves, however it differs from SAM in that it uses a pulsed laser to generate the PA waves. In 1981, Bowen et al. conducted theoretical and experimental studies of thermoacoustic waves with a goal of optimizing their sensitivity for imaging in biological tissue (18). This groundbreaking research paved the way for the PAI modality which has gained great popularity over the last decade and occupies a unique niche in the world of biomedical imaging as it bridges the gap between the microscopic and macroscopic scales (2, 6, 10, 14, 15). Optical imaging techniques can typically provide high resolution images of ca. 1 μm with a tissue depth penetration of ca. 1 mm (7). However, optical imaging techniques are constrained by an intrinsic trade-off between depth of penetration and spatial resolution due to light scatter by biological tissue. PAI couples the high contrast benefits of fluorescence imaging with the deep tissue penetration of ultrasound serving as a nexus between macroscopic and microscopic imaging techniques. Biological tissue is several orders of magnitude more transparent to soundwaves than electromagnetic radiation allowing PAI to obtain high contrast images of biological tissue at depths up to 5 cm. By coupling two well-established technologies in optical and ultrasound imaging, PAI has the capability of generating high contrast images in deep tissue at a lower cost when compared with traditional diagnostic imaging. PAI also uses non-ionizing radiation in contrast to common biomedical imaging techniques such as CT scanning, and position emission tomography (PET). PAI can also be considered non-invasive. For example, hemoglobin can be used as an endogenous contrast agent to obtain histological imaging, and has even been investigated ex vivo for nonlinear PAI (19). However, the addition of exogenous PA contrast agents allows for microscopic imaging with far greater selectivity and contrast at a cellular and molecular level. So although the endogenous PA response of hemoglobin is advantageous when imaging, for example, vasculature tissue an exogenous contrast agent is often required.

The variety of PA contrast agents reported to date can be categorized into five sub-categories including (i) molecular dyes (ii) semiconducting polymers (iii) carbon-based nanomaterials (iv) metallic nanomaterials and (v) PA-enhanced hybrid nanocomposites. In particular, MPACs are of great interest for PA contrast agents due to the structural diversity available to allow tuning of their absorption and photoacoustic properties, in addition to their inherently small size which can be optimized for *enhanced retention and permeability* (EPR) of cancer

cells for improved contrast (20). Various classes of molecular dyes have been employed as MPACs to date since the technique was first developed. Current design of MPACS for in vivo PAI has been recently reviewed (21), however, the goal of this review article is to provide a comprehensive account with a greater focus on the structural diversity and design of MPACs. While the topic of optoacoustic, a.k.a. photoacoustic spectroscopy, is briefly mentioned, our primary focus is on the summary of molecular dyes reported as contrast agents for PA imaging (PAI); this is inclusive of molecular dyes self-assembled in micelle and liposome nano- or micro-scale materials. For readers interested in polymeric organic-based, or inorganic-based, nanoparticles or nanocomposites for PAI applications this work has been reviewed in some excellent articles (3, 5, 8, 9, 11, 13, 16, 22). Firstly, another classification of PA contrast agents is here introduced, irrespective of structure or material composition, but based solely upon the photophysical mechanism by which a MPAC generates its PA response. Furthermore, although a discussion of experimental apparatus is beyond the scope of this review, the authors wish to recommend a basic starting point for interested readers should they wish to learn more about the practical aspects of fundamental PA characterization (23–25), as well as in-vitro and in-vivo PAI techniques (2, 3, 10, 15, 26–30). Finally, for readers interested in exploring the clinical applications of PAI in more detail this area of research has been reviewed elsewhere (31, 32).

CLASSES OF PHOTOACOUSTIC CONTRAST AGENTS

In PAI the acoustic response of the contrast agent is equally important to its ability to absorb within the biological imaging window (33). It is commonly assumed that a low fluorescence quantum yield is necessary for a molecule to generate a strong PA contrast. Under low intensity irradiation the PA response exhibits a linear dependence with respect to the incident light intensity as described by Eq. 1

$$PA = \varepsilon_g C_g \Gamma\, I\, \Phi_{nr} \quad (1)$$

where ε_g is the ground state molar extinction coefficient of the contrast agent at the incident wavelength, C_g is the ground state concentration of dye molecules (note: that for non-molecular systems the product of $\varepsilon_g C_g$ can be replaced in Eq. 1 by a materials ground state absorption coefficient, α_g), Γ is the Grüneisen coefficient, I is the incident photon fluence, and Φ_{nr} is the quantum yield for non-radiative decay. The Grüneisen coefficient, Γ, is a constant that quantifies a medium's ability to conduct sound efficiently that is defined by Eq. 2

$$\Gamma \;=\; \frac{V_s^2 \alpha}{C_p} \quad (2)$$

where V_s is the velocity of sound, α is the thermal expansion coefficient of the medium, and C_p is the specific heat of the medium at constant pressure (34). While it is true, for the most part, that a low fluorescence quantum yield can correlate to a respectable PA response, this

approach to the design of MPACs is limited and only tells part of the story. For instance, it has been reported that two-photon absorption can lead to a greatly enhanced PA response in dyes that have a relatively high fluorescence quantum yield (35, 36). Thus, at higher laser intensities a nonlinear optical absorption and an ensuing amplified PA response can be observed as described by Eq. 3

$$PA = \varepsilon_g C_g \Gamma \quad I \, \Phi_{nr} + \varepsilon_e C_e \Gamma \, I^2 \ldots + \; \varepsilon_n C_n \Gamma I^{n+1} \quad (3)$$

where ε_e is the first excited state molar extinction coefficient at the incident wavelength and C_e is the concentration of excited state dye molecules (36). It should be noted that Φ_{nr} is only relevant for the initial linear term in Eq. 3, consistent with Kasha's rule (37), as $\Phi_{nr} \sim 1$ for excited state non-radiative decay, i.e. $S_n \rightarrow S_1$ or $T_n \rightarrow T_1$. Thus, using Eq. 3 is a more comprehensive descriptor of a contrast agent's PA response, three distinct categories of MPACs can be defined based upon their characteristic optical absorption and resulting PA response to a low or a high laser fluence:

i) *Linear absorber (LA)* → *linear PA emitter* ($\varepsilon_g \quad 0, \tau \ll \tau_{laser}$)

    If the dye possesses an excited-state lifetime significantly shorter than the laser pulse this permits rapid non-radiative decay back to the ground state (bleaching does not occur). Subsequent photon absorption can then occur within the same laser pulse. Excited state absorption is does not occur and a linear dependence of the PA signal amplitude on laser fluence is observed as described by Eq. 1.

ii) *Saturable absorber (SA)* → *weak PA emitter* ($\varepsilon_g \quad 0, \varepsilon_e < \varepsilon_g, \tau > \tau_{laser}$)

    Saturable absorbers exhibit negligible or zero excited state absorption but, in contrast to linear absorbers, do possess an excited state lifetime comparable to, or greater than, the laser pulse width. As such, ground-state photo bleaching occurs evident by an increased transmission with increasing laser fluence.

iii) *Reverse-saturable absorber (RSA)* → *nonlinear PA emitter* ($\varepsilon_g \quad 0, \varepsilon_e \quad 0, \tau > \tau_{laser}$).

    With an excited-state lifetime comparable to, or greater than, the laser pulse width, concomitant with a non-zero excited-state absorption cross-section, a nonlinear increase in absorption and PA response may be observed with increasing laser fluence as described by Eq. 3. Ground-state photobleaching occurs but does not impede excited-state absorption (38).

Thus, in contrast to the conventional design of MPACs using Eq. 1, molecular dyes with large fluorescence (Φ_{fl}), or phosphorescence (Φ_{ph}), quantum yields that also exhibit excited-state absorption are capable of generating an amplified PA response via a nonlinear photon absorption and enriched non-radiative decay pathway (Eq. 3). However, two important variables that must be considered in this process are the laser fluence and also the lifetime of the laser pulse, which should be optimized with respect to the lifetime of the excited-state. In summary, the molecular photophysical characteristics which determine the class of an MPAC as either an *LA*, *SA* or *RSA* material are (i) the ground state molar extinction

coefficient (ε_g) (ii) the excited state molar extinction coefficient (ε_e) and (iii) the excited state lifetime (τ). *RSA* materials will show a greater PA amplification as the ratio of excited-state vs. ground-state absorption coefficients increases ($C_e.\varepsilon_e:C_g.\varepsilon_g$) at the incident wavelength, keeping in mind that the relative concentrations of C_e versus C_g are dependent upon the excited-state lifetime, the laser fluence and the laser pulse width.

Although nonlinear *RSA* materials are anticipated to be the most promising dye category for generation of an enhanced nonlinear PA response it must be kept in mind that their application is very much limited to scenarios where the application of high laser fluences are feasible. While a number of studies addressing nonlinear PAI have emerged (19, 24, 25, 35, 39–60) very few have involved in vivo studies (54, 56, 57), none of which have relied solely on a molecular based contrast agent. As such, all of the in vivo imaging applications of MPACs discussed in this review have been conducted under low laser fluence conditions where the dye either behaves as a *LA* or *SA* material. Nonlinear optical absorption still represents a great challenge for biomedical imaging, not just in PAI, due to the American National Standards Institute (ANSI) laser fluence thresholds (61). However, with the mechanism of a nonlinear PA response now well established this opens up a previously unexplored avenue of research within the field of PAI itself. Although much work is required to reduce the laser fluence required to observe a nonlinear PA amplification below ANSI recommended laser fluence thresholds, in vitro methods using nonlinear NIR absorbing contrast agents for high-resolution photoacoustic microscopy (PAM) is an area where *RSA* materials have not yet been investigated but which hold great promise as PAM is not restricted by ANSI limitations (10, 29, 30, 42, 45, 47, 49, 51, 62, 63).

MOLECULAR PHOTOACOUSTIC CONTRAST AGENTS

In all cases a desirable MPAC should satisfy at least the following criteria; (i) possess a high ground-state molar absorptivity at a desired excitation wavelength within the near infrared (NIR) biological transparency window (9) (ii) exhibit a quantitative photoacoustic response (*LA* or *RSA* depending upon the laser fluence applicable) (iii) have a high solubility and stability in vivo (iv) exhibit a low toxicity. There are limited commercially available dyes that meet each of these criteria and only select few have been investigated for PAI. With a rapidly growing interest in PAI the library of available MPACs will assuredly grow in coming years. It is the author's aim that this review may serve as a point of reference for researchers exploring established and alternative MPACs, and also for those researchers who wish to contribute to the design of more efficient MPACs. There is no class of commercial NIR dyes that have been studied more than cyanine based dyes, which makes this an appropriate starting point to review the various dyes investigated for PAI to date.

Cyanine dyes

Cyanine dyes are structurally composed of two nitrogen containing moieties, typically indoline, oxazole, thiazole or quinoline heterocycles, joined by a linear polymethine chain. In all cases one of the nitrogen atoms is quarternized and the positive charge is resonant with the opposite N-heterocyclic ring system through the conjugated polymethine chain, typically composed of 1, 3, 5 or 7 carbon atoms (64). By extending the polymethine chain the

absorption and emission properties can be predictably red-shifted. Generally, extending the chromophore by one vinylene moiety will give rise to a bathochromic shift of about 100 nm. Examples of Cy3 (**1**), Cy5 (**2**) and Cy7 (**3**) based indocyanine dyes are provided in Figure 1 below (65).

For nearly 25 years researchers have been investigating the PA properties of cyanine dyes. This began with Braslavsky's groundbreaking laser-induced optoacoustic spectroscopy (LIOAS) method to determine the volume changes and thermodynamics associated with the *E-Z* photoisomerization of carbocyanines (66, 67). Laser-induced optoacoustic spectroscopy is a photoacoustic method that has been used by photochemists as a tool that complements existing methods used to determine quantum yield, lifetime decay, and energy content of excited-state molecules (66). In 1994, Braslavsky and coworkers used Cy3 and Cy5 in photoacoustic calorimetry experiments to record the volume change caused by a photo-induced *E-Z* isomerization in the polymethinic chain of the cyanine dyes (67). Around this time there were similar experiments that used simultaneous luminescence and photoacoustic experiments as a method to determine the absolute fluorescence quantum yield of Cy5 in an ethanol solution (68). At this point, the photoacoustic properties of molecular dyes were being used solely to investigate their fundamental photophysical properties; monitoring PA amplitude and applying it to PAI did not occur until 15 years later. Today, the majority of PA investigations of cyanine based dyes are primarily related to applications in biological imaging.

The Cy3, Cy5 and Cy7 dyes were initially designed for fluorescence imaging applications due to their tunable absorption and emission spectra, in addition to their possessing high molar extinction coefficients often reaching 200,000 M^{-1} cm^{-1} (64, 69, 70). In particular, the water soluble indocyanine green (ICG, Fig. 2 **4**) dye has been studied intensely for in vivo fluorescence imaging ever since it was approved for ophthalmic angiography by the Food and Drug Administration (FDA) due to its low toxicity (69, 71–76). ICG is a Cy7.5 derivative containing a benzoindole heterocycle (indicated by the 7.5 nomenclature) with butane sulfonic acid/sodium sulfonate chains at both its indole N-atoms (Figure 2).

As the sodium salt it is water soluble with a λ_{max} at 780 nm, well within the biological transparency window, which has made this cyanine dye and its analogues a popular choice in a wide variety of medical diagnosis, imaging and therapy applications (64, 77). The NIR absorption, commercial availability, and tunability of cyanine dyes has given rise to a wide variety of cyanine compounds that are highly stable and soluble in water while maintain high solubility and fluorescence quantum yields in water (74). FDA approval for cardiocirculatory monitoring, liver function tests and ophthalmological imaging has made ICG arguably the most studied NIR dye to date (78). In 1996 Abels and co-workers published a comprehensive study of the absorption and fluorescence properties of the disodium iodide salt of ICG (70). While this study did not entail any PA experiments, it did give critical insight to the photophysical behavior of cyanine dyes in aqueous solutions in the absence and presence of a protein macromolecule. It was demonstrated that ICG dimerizes in an aqueous solution at concentrations of less than 3×10^{-8} M significantly reducing its fluorescence quantum yield (monomer $\Phi_{fl} = 0.027$, dimer Φ_{fl} not reported). However, simply in the presence of the albumin protein (7.3×10^{-4} M), dimerization was not observed

until higher ICG concentrations of $\sim 10^5$ M attributed to adsorption of ICG at the protein macromolecule which increased Φ_{fl} to 0.040. Similar conclusions were later reported by Mordon et al. regarding the fluorescence properties of ICG dye in vivo with respect to its interaction with blood components and/or vessel walls (75).

The earliest PAI investigation of any cyanine dye was by Kim et al. where ICG was investigated as a bi-functional theranostic agent for early-stage cancer detection by PAI combined with photodynamic therapy (PDT) (79). The ICG molecule was embedded in an 'organically modified silicate' (ormosil) matrix of 100 nm diameter nanoparticles. Conjugation of the ICG-ormosil nanoparticles to the HER-2 antibody was accomplished using the PEBBLE (*photonic explorers for biomedical use by biologically localized embedding*) method to target LNCaP prostate cancer cells. It was determined that 10^{11} PEBBLEs/cm^3 were required at a laser fluence of 2.6 mJ/cm^2 at 800 nm laser excitation to optimize the PA response. Kim et al. also reported improved stability of ICG embedded in a silicate matrix when compared to the free ICG dye. This enhanced stability was attributed to isolation of the ICG molecule within the silicate matrix, preventing dye-dye interactions. ICG has since been utilized in a similar fashion in the design of many nanoparticle and polymer based materials for PAI applications (80–90).

In 2010 Laufer et al. reported on the PAI for a series of modified water soluble cyanine dyes ADS$_{740}$WS (**5**) and ADS$_{830}$WS (**6**) in tissue phantoms (Fig. 3) (91). Unfortunately the authors concluded that the cyanine dyes were not suitable for quantitative photoacoustic measurements for three reasons; 1) photoisomerization gave rise to changes in their ground state absorption spectra 2) dye aggregation caused a similar change in their absorbance spectra and 3) all three dyes were prone to irreversible oxidative photobleaching.

A 2014 study by Guo et al. incorporated the bis-carboxy cypate cyanine dye (Fig. 4(a) **7**) into mPEG-*b*-Pas(DA) derived micelles for in vivo tumor imaging using both PA and fluorescence detection (92). Enhanced photostability, tumor cell permeability and retention was reported. Co-encapsulation of the chlorin based Ce6 photosensitizer alongside cypate allowed for PDT subsequent to imaging studies using a dual photothermal therapy/ photodynamic therapy (PTT/PDT) approach. Using an impressive trojan-horse type approach, PTT was deemed to rupture the micelle assembly leading to cellular release of the Ce6 photosensitizer and an enhanced PDT efficacy.

In their 2014 study Temma et al. compared the cyanine derivative IC7–1-Bu (Fig. 5 **8**) to the ICG reference dye, in the absence of any conjugated targeting strategy, for in vivo PAI of subcutaneously HeLa inoculated mice (93). In vivo PA tomography performed 24 h and 48 h post intravenous injection of **8** exhibited a 2.3-fold higher PA contrast relative to ICG, combined with a high tumor fluorescence. Biodistribution studies confirmed a rapid clearance of ICG from the liver to the intestine suggesting bioconjugation is required for its effective application as a PA (or fluorescent) contrast agent to prevent rapid elution. In vitro fluorescence of tumor homogenates estimated a $10.0 \pm 0.3\%$ uptake of **8** per gram of tumor, indicating an improved specificity of **8** relative to free ICG, in the absence of antibody conjugation, confirming its potential as both as a fluorescence and PA contrast agent.

Although **8** is an improved PA contrast agent relative to ICG, it still lacks photostability consistent with ICG (91).

The latter study motivated Onoe et al. to later develop asymmetrical derivatives of **8** functionalized with a 4-nitrobenzyl alcohol group to serve as a triplet quencher moiety (Fig. 6 **9** - **11**) (94). It was found that these triplet quencher functionalized derivatives displayed in vitro PA signals that were equivalent to **8** while showing a 1.5-fold increase in photostability. Interestingly, the singlet oxygen generating property of cyanine dyes, the very characteristic that was originally deemed undesirable, has since been exploited by researchers to create theranostic dyes (compounds that have the ability to both image cancer cells and destroy them using PTT) (77, 95, 96), as well as to trigger the release of therapeutic agents in-vivo from heptamethine cyanine derived photocages (97).

In their 2014 study Kanazaki et al. conjugated the human serum albumin (HSA) protein with ICG to enhance its permeability and retention for improved in vivo PAI of allografted tumors in mice (98). ICG was later conjugated with the poly(ethylene glycol) (PEG) polymer, again to enhance permeability and retention (99). PEG has demonstrated EPR (20) in tumor cells, however PEG has a prolonged half-life in the bloodstream which decreases the desired PA response in targeted tumor tissue, increasing the PA response in healthy vascular tissue (99, 100). Nanoparticles derived from ICG-PEG conjugates varied in diameter from 4 – 14 nm depending upon the PEG mass (5 – 40 kDa). By also doping the PEG polymer with a ^{111}In label (Fig. 7 **12**), the in vivo biodistribution of PEG derived nanoparticles was determined in colon26 tumor-bearing mice using a combination of single-photon emission computed tomography (SPECT) and PAI (99).

Related to the earlier porphyrin-based study by Huynh et al. (vide infra) (101), Hannah et al. reported a bimodal ultrasound (US) and PA study on ICG-loaded perfluorocarbon nanodroplets (average diameter = 600 nm) containing an albumin protein shell (102). These nanodroplets were demonstrated to exhibit an enhanced PA contrast in polyacrylamide-based tissue phantoms by an optically triggered liquid-to-gas phase transition of the perfluorocarbon into microbubbles contributing to an enhanced US contrast.

In 2016, Kanazaki et al. also conjugated ICG with partially hydrolyzed polyoxazoline (POZ-ICG) as a tumor-targeted PA probe, again optimizing the in vivo tumor EPR effect (103). It was observed that increased ICG loading of the polyoxazoline probes significantly enhanced the PA contrast at equal ICG concentrations (lower probe dosage), likely due to ICG aggregation induced enhancement of non-radiative decay, consistent with analogous PA studies in protein submicrospheres which have a low density and good compressibility for acoustic wave transduction (104). Variation of the polymer weight as well as ICG loading revealed that 5% hydrolyzed 50 kDa POZ conjugated with 7.8 equivalents of ICG exhibited optimum tumor uptake and PA contrast by 39% relative to free ICG.

Lin et al. have polymerized a heptamethine cyanine derivative (similar to **6**) directly into a poly(ethylene glycol)$_{2k}$-*block*-poly($_{D,L}$-lactide)$_{zk}$ (PEG-PLA) based nanoparticle (Fig. 8 **13**) (105). This approach resulted in a nanoparticle with a particularly high theranostic agent

loading capacity of greater than 50% with both PAI and near-infrared fluorescence imaging properties, as well as phototherapeutic properties.

In one of the most ambitions molecular modifications of the cyanine template reported by An et al. a supramolecular bis-pyrene cyanine dye **14** (Fig. 9) was engineered to self-assemble into hollow nanovesicles for PAI applications at 10 mM concentration in a DMSO:H_2O (v:v = 1:99) mixed solution (106). Nanovesicle diameters of 46.6 ± 6.0 nm were reported with a wall thickness of just 4.2 ± 0.7 nm confirming a head-to-head aggregation within the particles. Compared with the monomeric and reference ICG dyes, stable nanovesicles derived from **14** exhibited an enhanced contrast during PAI of breast-tumor-xenografted mice, in addition to improved in vitro and in vivo half-lives.

Scarfe et al. utilized photoacoustic tomography (PAT) of the of IRDye800CW carboxylate cyanine derivative (Fig. 10 **15**) to quantify clearance and thus kidney function in severe combined immunodeficient (SCID) mice with adriamycin-induced nephropathy (107). As a result, successfully confirming the loss of renal function in experimental animals versus controls. In a 2016 study Shi et al. incorporated the IR780 cyanine dye (Fig. 10 **16**) within an amphiphilic camptothecin@poly(ɛ-caprolactone) copolymer (108). Self-assembly of this copolymer with **16** at its core, within a helical poly(phenyl isocyanide) (PPI) micellar nanoparticle shell (60 – 77 nm diameter) was reported including the pH-responsive rhodamine B (RhB) fluorophore at the micelle core-shell interface. The hydrophilic helical PPI coronas provided excellent cell membrane permeability whilst in vitro and in vivo studies confirmed a pH-dependent fluorescence of RhB and strong PA contrast of **16** allowing for bimodal cancer diagnosis. Furthermore, 808 nm irradiation of **16** ruptured the micelle camptothecin release which was demonstrated to effectively decrease tumor recurrence rates in HeLa tumor-bearing mice.

In a 2016 study by Biffi et al. stable core–shell silica-PEG nanoparticles, composed of a ~10 nm silica core and a ~5 – 8 nm PEG shell, were covalently doped with both Cy5.5 (**17**) and Cy7.5 (**18**) dyes (Fig. 11) (109). By tuning the ratio of Cy5.5 and Cy7 dyes, which absorb at 670 nm and 810 nm respectively, the fluorescence imaging, PAI and PTT properties of the nanoparticles were optimized. The authors were keen to highlight how selective photoexcitation of either **17** or **18** could allow for multiplexing PAI in future studies.

Also in 2016, Wang et al. reported on the fluorescence and PAI dual modal-guided PTT treatment of Hela tumor bearing mice using a rapamycin/Cy7 (**3**) loaded lipid-polyaniline nanoparticle (RDLPNP) where rapamycin is an antiangiogenesis chemotherapeutic drug (110). This particular study actually utilized the *N,N'*-dioctadecyl Cy7 dye as a fluorescent probe and photosensitizer for energy-transfer to the polyaniline acoustic emitter. FRET induced PTT by selective excitation of the Cy7 dye resulted in enhanced tumor eradication due to release of the rapamycin chemotherapy agent.

In a novel and recent application of cyanine dyes Mishra et al. reported the synthesis, characterization and evaluation of a reversible NIR absorbing PAI responsive Ca^{2+} chemosensor based upon the IR780 (**16**) template with an appended Ca^{2+} chelating moiety in (4-hydroxy-2-[2-(morpholin-4-yl)-2-oxoethoxy]phenyl))amino]acetic acid (Fig. 12 **19**)

(111). Selective chelation of Ca^{2+} (threefold relative to Mg^{2+}) gave rise to a reproducible loss of PA signal due to a decrease in molar extinction coefficient of the $\pi-\pi^*$ NIR absorption band.

Although cyanine dyes have been comprehensively studied, they do have several drawbacks. For example, the concentration and optical properties of ICG can change dramatically by forming aggregates in aqueous environments and binding with intercellular components such as proteins, lipoproteins, and the cell membrane phospholipid bilayer (71, 75). This problem is often encountered during optical imaging assays but may in fact be beneficial at least with respect to generation of a linear PA response. For example, it has been noted that self-quenching occurs in Cy5, Cy5.5, and Cy7 reducing their fluorescence quantum yield (74). Additionally, as the polymethine chain increases the fluorescence quantum yield and absorbance decrease (69). A more serious problem with traditional cyanine dyes is their photostability (112–116).

Phthalein and Xanthene dyes

Fluorescein (**20**) is a well-known dye that has a wide variety of uses, from the green glow often seen in anti-freeze to a reference dye used in spectroscopy for fluorescence quantum yield measurements (Fig. 13) (117, 118). Fluorescein is structurally similar to the famous pH indicator phenolphthalein (**21**) except that it has an oxygen bridge fusing both its benzene rings making it part of the xanthene family (Fig. 13). Although it is a seemingly small modification, the fused O-bridge of the xanthene core restricts the rotational freedom of its conjugated π-system and imparts fluorescein with a high fluorescence quantum yield ($\Phi_{fl} = 0.925$) (119). The increased rotational freedom exhibited by **21** (phthalein dyes lack the fused O-bridge of the xanthene family) is responsible for its increased linear PA response when compared to that of **20**. Boguta et al. reported that **21** had a PA signal two times greater than that of **20** (120). Despite the relatively low PA response of **20**, it has received a considerable amount of attention in PA studies, ironically due to its greater popularity as a fluorescence imaging contrast agent. In some cases, however, it is merely used as a fluorescent probe to compliment alternative PAI studies (121, 122). In the 1980's photoacoustic spectroscopy was used to determine the concentration of **20** adsorbed onto silica gel and demonstrate the advantage of this nondestructive method for quantitative analysis (123). McDonald et al. reported a two-fold increase in PA signal following the adsorption of fluorescein isothiocyanate to elastin submicrospheres, even when the dye concentration was decreased by four orders of magnitude (104). The increase in PA signal was caused by the low density and good compressibility of the protein submicrospheres. These results are consistent with the work of Kanazaki et al. who also reported an increased PA response by incorporating a cyanine dye into the backbone of a polyoxazoline polymer (103).

Rhodamine dyes **22** - **24** are structurally very similar to **20** except that their terminal hydroxyl and ketone moieties are replaced with more electron rich amino groups, effectively destabilizing their HOMO levels to narrow the optical band-gap and red-shifting their absorption and fluorescence emission spectra (Fig. 13). Rhodamine B (**23**) exhibits an absorption maximum (λ_{max}) at 539 nm and an emission maximum (λ_{em}) at 571 nm with a

Φ_{fl} of 0.66 (124, 125). Rhodamine 6G (**24**) exhibits a λ_{max} at 527 nm and a λ_{em} at 552 nm with an impressive Φ_{fl} of 0.95 (124, 125). In water, the Φ_{fl} decreases significantly for **23** and slightly for **24** with values of 0.40 and 0.94 respectively (124, 125). Due to their high quantum yields rhodamine based dyes are less amenable as PA contrast agents and, similar to **20**, are often used as reference fluorophores in PAI investigations (108, 126). Fluorescein and rhodamine based dyes have both been the subject of a fundamental photoacoustic spectroscopy (PAS) study to accurately determine their fluorescence emission quantum yields. Niessner et al. used pulsed laser PAS to determine the absolute fluorescence quantum yield of **24** in ethanol and in water (124). For fluorophores with small Stokes shifts and high quantum yields, as is with all rhodamine derivatives, inner-filter effects can result in an inaccurate quantum yield measurements when using the relative method of quantification (127). Indirectly quantifying Φ_{fl} by PAS has proven to be very successful as it has provided results highly consistent with the findings of previously reported fluorescence quantum yield data. The advantages of using PAS for fluorescence quantum yield determination are its simple calibration and the decreased interference of reabsorption effects, which is especially relevant for rhodamine dyes which typically has a narrow Stokes shift. The disadvantage of PAS is the degradation of samples from high laser fluence which is a requirement of the PAS method.

Fluorescein and rhodamine based-dyes are however more amenable to the emerging technique of two-photon absorption enhanced PAI as first reported by Yamaoka et al. (39, 40, 43, 51) and Raaij et al. (41), specifically for the emerging high-resolution in vitro raster scanning technique of PAM (42, 47, 49, 51). Langer et al. later conducted a comprehensive bimodal PA/fluorescence study of **23** in homogeneous aqueous solution and heterogeneous polyethylene microspheres (100 μm diameter), relative to carbon fiber and silicon wafer (44). A concerted nonlinear photon absorption amplification of the homogeneous and solid-state amplitude was confirmed upon femtosecond pulsed laser excitation (λ_{exc} = 800 nm; τ = 50 fs at 3.968 Hz) and correlated to the complimentary two-photon induced fluorescence tomography image. Apart from some photobleaching issues, this study demonstrated that two-photon absorption PAM is a powerful imaging modality that has great potential as an independent technique or even used in tandem to compliment established two-photon based fluorescence imaging.

Using the rhodamine based Atto680 dye (Fig. 14 **25**) dissolved in methanol at 0.1 M, stored in a polymer capillary and immersed in an aqueous lipid based phantom tissue, Märk et al. demonstrated how a tailored pump-probe experiment can be used to optimize the PA amplitude (55). Not to be confused with concerted two-photon or sequential nonlinear absorption approaches, Märk et al. elegantly varied the pump-probe pulse delay time (0.0 – 7.7 ns) as well as the lifetime of **25** (Φ_{fl} = 0.63 [1] τ = 2.6 ns in MeOH) using a KI dynamic quencher (e.g. Φ_{fl} = 0.33 at 0.05 M KI in MeOH) to optimize stimulated emission from the S_1 excited state of **25**. Use of the KI quencher as well as the second probe pulse to stimulate emission effectively worked in tandem to modify the PA response of **25** from a linear absorber (*LA*) to a saturable absorber (*SA*) class of MPAC.

One of the most studied MPACs is 3,7-bis[dimethylamino]phenazothionium dye, commonly known as methylene blue (**26**) which is part of the xanthene family (Fig. 14). **26** has in

common with rhodamine two terminal electron-donating amino substituents, however, it has a bridging S-atom in place of the bridging O-atom of fluorescein and rhodamine derivatives, which enhances intersystem crossing and the yield of its triplet excited state. **26** has been used as a reference material in a wide variety of PA studies for many years. As such a full summary of this work is beyond the scope of this review article. In recent years, with a growing interest in PAI for biological applications there has been a resurgence PA studies of MB. These studies have ranged from PAI in tissue phantoms (128) to in vivo PAI of sentinel lymph nodes (129), to PA lifetime studies for aggregate (130) and in vivo dissolved oxygen (131) quantification, US/PA dual-modality imaging of MB/perfluorocarbon microbubbles (Fig. 15) (132) and theranostic PAI/PTT studies of polypyrrole-methylene blue nanoparticles (133).

A highly noteworthy and very recent PA study of **26** is that by Wang et al. where PAI confirmed an impressive 492-fold increase in PA amplitude upon encapsulation in sodium dodecasulfate (SDS) micelles (134). This dramatic increase in PA amplitude was found to be highly concentration dependent (0.05 mM **26** + 3.47 mM SDS) with a 54-fold decrease in PA intensity observed upon increasing SDS to its critical micelle concentration (cmc = 8.67 mM). Using the technique of nanoparticle tracking analysis (NTA) the optimum PA amplitude observed well below the cmc of SDS was attributed to the formation of **26**/SDS clusters as a result of **26** interaction with the sulfate anion of SDS.

Squaraine & croconaine dyes

The molecular structure of squaraine dyes are characterized by a central electron deficient four membered ring, derived from squaric acid, typically substituted in a trans configuration with two electron donating moieties, generating a quadrupolar resonance stabilized donor-π-acceptor-π-donor zwitterionic structure (33, 135). Commercially available squaraine derivatives are limited both in their structural diversity as well as their absorption which typically falls just short of the NIR spectral region of the biologically relevant transparency window, thus there has been significant interest to synthesize derivatives that absorb beyond 700 nm. For example, Umezawa et al. designed the KSQ-2 dye (Fig. 16 **27**) that exhibits a λ_{max} at 737 nm and has a high fluorescence quantum yield in low polarity solvents (Φ_{fl} = 0.56 in cyclohexane) (136). Expanding on the structure of **27**, Umezawa and coworkers added several sulfonate functional groups and two *N*-hydroxysuccimide (NHS) esters into the structure (Fig. 16 **28**) (137). These modifications made **28** soluble in an aqueous solution while also facilitating additional bioconjugation for targeted imaging. **28** exhibits a λ_{max} at 787 nm and a sharp emission at 812 nm (Φ_{fl} = 0.08) in a PBS solution at a pH of 7.4 when conjugated to the bovine serum albumin protein. Water solubility, NIR absorption and low fluorescence quantum yield make **28** a good candidate for PAI.

The first PAI studies of squaraine dye for PAI emerged in 2014. An et al. (138) used the 2,4-bis(4-(dibenzylamino)phenyl)cyclobuta-1,3-diene-1,3-bis(olate) squaraine (Fig. 17 **29**), earlier reported by Arunkumar et al. (139), which possesses an absorption maximum at 637 nm (Φ_{fl} = 0.45, τ = 2.14 ns) in THF:water (v/v 4:1). This 4-(*N,N'*-dibenzylamino)phenyl substituted squaraine was loaded into aqueous dispersed albumin nanoparticles causing an aggregate induced red-shift into the NIR to almost 800 nm, albeit with a concomitant

broadening and slight reduction in its molar extinction coefficient (138). With commercial PAT equipment and pulsed laser excitation at 740 nm, 200 μL of 0.5 mM squaraine-loaded albumin nanoparticle solution generate excellent in vivo PA images of 4T1 tumor bearing mice (Fig. 17).

Ho et al. conducted a study comparing the PA properties of the commercially available 2,4-bis [4-(*N,N*-dibenzylamino)-2,6-dihydroxyphenyl] squaraine dye ($\Phi_{fl} = 0.037$) to the zinc phthalocyanine, protoporphyrin IX, chlorin e6 and methylene blue dyes in tissue phantoms (Fig. 18 **30**) (140). **30** exhibited a PA amplitude of just 0.18 relative to zinc(II) phthalocyanine, however, based upon is dual fluorescence and PA properties, as well as having a singlet oxygen quantum yield of 0.61–0.74, the authors suggested that this squaraine derivative has the potential to serve in a theranostic manner as bimodal fluorescence/PA contrast agent as well as a PDT photosensitizer.

Similarly, Zhang et al. reported that phospholipid bilayer liposomes doped with the bis-(iodo-*N*-butylindole) squaraine derivative (Fig. 19 **31**) form *H*-aggregates and producing an enhanced in vivo PA contrast in MCF-7 tumor bearing mice (141). The authors determined that a 1:10 ratio of **31**:liposome resulted in the formation of *H*-aggregates that produced a PA response two times greater than the 1:100 ratio of **31**:liposome that did not form *H*-aggregates. This method proved successful for entire body PAI of mice with the greatest PA signal recorded in the spleen, and the tumor site exhibiting the second most intense contrast at 0.7 relative to the spleen based response (Fig 19). Zhang et al. highlighted how embedding the dye within a vesicle (micelle or liposome) preserves the photo- and chemical-stability of MPACs, reducing photobleaching and cytotoxicity (142). Also in 2014, Duan et al. used a very similar bis-(chloro-*N*-butylindole) squaraine dye (Fig. 19) as a PAT agent to determine the pH dependent release profile of the anti-cancer drug doxorubicin in human breast cancer MCF-7 cells (143). Ex vivo measurements confirmed that at pH < 5 **32** formed *H*-aggregates changing the absorption ratio at 650 nm (monomer) and 698 nm (aggregate) from 0.44 to 0.79 for an enhanced PA response. Both **32** and the doxorubicin drug were sequestered within pH sensitive PEG-modified poly(β-amino ester) graft copolymer based micelles. In the mildly acidic environment of cellular lysosomes the micelles released both the PA probe and the doxorubicin drug confirmed by fluorescence and PAI of **32**. By encapsulating the MPAC within a pH responsive micelle a novel method to observe pH controlled drug release was thus established using PAT to provide a high contrast.

In a later study, Sreejith et al. validated the previous strategy by utilizing the bimodal fluorescence and PA imaging properties of a PEG-ylated squaraine dye (Fig. 19 **33**) encapsulated within a micelle for in vivo imaging of the spinal cord, lung, c. vena cava, liver, and gallbladder of a mouse (142). PAI at 840 nm excitation exhibited high contrast combined with deep tissue imaging. PAT images exhibited the strongest response in the liver and lungs of the mouse as no biomarkers were used to tag specific tissues.

In 2016, Anees et al. introduced an asymmetrical NIR absorbing squaraine dye **34** (in DMSO $\lambda_{max} = 680$ nm, $\varepsilon = 1.94 \times 10^5$ M^{-1} cm^{-1}, $\lambda_{em} = 705$ nm, $\Phi_{fl} = 0.27$) for in vitro and in vivo biomodal fluorescence/PA detection of biological thiols (Scheme 1) (144).

Addition of glutathione, cysteine and homocysteine as biologically relevant thiols to **34** in a phosphate buffer (pH 7.8) with 4% DMSO (to prevent aggregation) exhibited a decrease in the 680 nm absorption band with a concomitant decrease in Φ_{fl} and the appearance of a new band at 380 nm attributed to thiol addition at the cyclobutene ring of the squaraine core. The same response was confirmed by in vitro fluorescence imaging of human hepatoma (Huh-7) cell lines and PAT of tissue phantoms. In vivo fluorescence/PAT of severe combined immune deficiency (SCID) female mice under fasting conditions confirmed the effect of food uptake on the increased level of aminothiols in blood (Fig. 21).

To provide real-time feedback on cancer therapy, Qiao et al. used a micelle encapsulated squaraine dye to monitor in vitro reactive oxygen species (ROS) generation in U87 glioblastoma cells by PAI. Micelle encapsulated nile red dye was also investigated by the authors in parallel experiments as a fluorescent ROS sensor (145). Key to this study was the tailored ROS-sensitive micelle that was derived from the cytotoxic KLAK peptide conjugated with a ROS-sensitive amphiphilic poly(β-thioester) copolymer (H-P-K) and a hydrophillic PEG2000-SH side chain. The KLAK peptide is capable of stimulating cell mitochondria to constantly produce ROS until cell apoptosis. Upon ROS overexpression, swelling of the micelle caused release of the squaraine dye into the cytosol where it formed *H*-aggregates enabling PA signal generation. Unfortunately, the authors did not identify the structure of the squaraine dye used.

Related to squaraines are the croconaine class of dyes whose core structure is derived from the 4,5-dihydroxy-4-cyclopentene-1,2,3-trione (aka croconic acid) 5-membered ring system, and typically exhibit an impressive NIR absorption (e $\sim 10^5$ M^{-1} cm^{-1}) from 700 nm even as far as 1000 nm (146). While there has been a growing interest in the application of croconaine dye's for in vivo PTT applications (147–151), study of their PA properties has been restricted to just two reports (149, 151). In 2016 Guha et al. reported on the PTT and PAI properties of a pH sensitive croconaine dye encapsulated in a rotaxane macrocycle (**35**) to reduce aggregation and improve monomer stability and NIR absorption (Scheme 2) (149). The anionic croconaine:rotaxane assembly was made water soluble by incorporation into 1-palmitoyl-2-oleoyl-*sn*-glycero-3-phosphocholine (POPC)-cholesteryl-polyethylene glycol 600 sebacate (Cholo-PEG600) based liposomes as an amphiphilic ion-pair with the 1,2-dioleoyl-3-trimethylammoniumpropane (DOTAP) cation using a composition of POPC:Chol-PEG600:DOTAP:Croc (84:10:3:3) resulting in 194 nm diameter nanoparticles. Upon decreasing an aqueous buffer pH from 7.4 to just 5.0 the **35** doped liposomes exhibited a red shift from 697 nm to 815 nm of its the lowest-energy absorption band, which was attributed to N-protonation of the croconaine 2,3-dimethyl-7-nitro-1H-indole substituent. Ex vivo PAI of **35** doped liposomes was investigated in tissue phantoms at pH 7.4 or 5.0 at depths of up to 13 mm and exhibited PA signal maxima at 690 nm and 812 nm, respectively, correlating very well with the pH dependent absorption spectra. Thus, ratiometric in vivo PAI was subsequently conducted to determine the pH of peritoneal fluid in a living mouse. A ratiometric comparison of the deprotonated vs protonated PA peak response enabled confirmation of the in vivo peritoneal pH to be in the range 6.0 – 6.5.

Tang et al. have used PEG-ylated derivatives of the 2,5-bis[(4-carboxylic-piperidylamino)thiophenyl]-croconaine (**36**) dye to self-assemble water soluble croconaine-

PEG based nanoparticles for PAI and fluorescence imaging guided PTT of MCF-7 tumor bearing mice (Fig. 22) (151). By varying the size of the PEG chain at **36** from PEG132, PEG2K and PEG5K the nanoparticle diameter was tuned from 200 nm, to 102 nm and 13 nm, respectively, with the **36**-PEG5K based nanoparticles reducing to just 5 nm diameter in blood serum. Comparison of **36**-PEG5K nanoparticles to the water-soluble sodium salt of the **36** monomer confirmed a stronger fluorescence signal from the nanoparticles. However, its fluorescence response decreased rapidly at > 30 μM concentration with a concomitant increase in its PA amplitude exceed that of the monomer reference dye. Ex vivo incubation with MCF-7 cancers cells confirmed the endocytosis ability of both **36**-PEG5K nanoparticles and the sodium salt monomer, however the former exhibited an almost 2-fold greater PTT efficiency. NIR fluorescence imaging and PAI of **36**-PEG5K nanoparticles in MCF-7 tumor bearing mice indicated an improved EPR effect at the tumor site consistent with prior PEG-ylated studies.

Tetrapyrrole

While there are early literature reports on the application of LIOAS and PA spectroscopy to porphyrins related to their fundamental photophysical characterization (152–165), the porphyrin, and related tetrapyrrole PAI based literature is relatively sparse considering the rich photochemistry for this class of chromophore. The earliest example of a tetrapyrrole study related to PAI, to the best of our knowledge, is a 2002 report by Stolik et al. where in vivo PA spectroscopy was used to record the kinetics of δ-aminolevulinic acid (**37**) induced protoporphyrin IX (**38**) production in mice skin (Fig. 23) (166).

It was not until 2011 that a legitimate PAI study was reported by Lovell and co-workers where a porphyrin-lipid (Fig. 24 **39**) derived liposome (100 nm in diameter) was engineered to optimize light absorption, and to promote aggregate induced self-quenching to maximize the PA amplitude (167). These so-called 'porphysome' nanostructures were promoted by the authors as being enzymatically biodegradable with minimal acute toxicity in mice with intravenous doses of up to 1 g kg^{-1}. In the same study PTT by these porphysomes was demonstrated for tumor ablation in xenograft-bearing mice. In a subsequent study, Jin et al. demonstrated that the same nanostructured porphysomes are effective PTT agents for ablation of hypoxic tumors (168). Furthermore, the same porphysome nanoparticles were also later used by Ng et al. to develop a thermoresponsive in vivo sensor (169). Porphyrin aggregation in the liposome causes a 74 nm red shift and concomitant 2.7-fold increase in its Q_y band extinction coefficient. An identical shift is also observed in the fluorescence emission with aggregate emission in the liposome occurring at 824 nm relative to the monomer emission at 750 nm. Uniquely, due to thermal reorganization of the liposome, pophyrin aggregation was reversibly reduced thus allowing for a decrease and Q_y band absorption and hence its linear PA response. Monitoring the PA contrast following 824 nm irradiation, with increasing temperature an initial increase in PA signal was observed consistent with an increase in the Grüneisen coefficient, however, upon heating above the transition temperature of the phospholipid/liposome phospholipid, a rapid loss in PA signal was observed. Successful in vivo PA temperature sensing was reported in a KB-tumor bearing mice at 824 nm irradiation (allowing resolution from endogenous hemoglobin) over a temperature range of 25 – 52 °C.

In a related 2012 study by Huynh et al. a similar porphyrin–phospholipid conjugate was used to self-assemble a microshell structure (peak diameter ∼2.7 ± 0.2 μm), derived from 1-stearoyl-2-pyropheophorbide-*sn*-glycero-3-phosphocholine and 1,2-distearoyl-sn-glycero-3-phosphocholine (Fig. 24 **40**), which was used to trap microbubbles based upon a variety of fluorine based gases (101). An optimum 15 mol % of porphyrin-lipid was recommended for the phospholipid shell with perfluoropropane the primary gas studied. These microbubble/**40** microparticles were found to be excellent contrast agents for both traditional ultrasound as well as PAI with a low energy resonance frequency of 9–10 MHz. PAT was conducted with a 700 nm, 5 ns pulsed laser and a 10 MHz ultrasound transducer to demonstrate that PA contrast was not only dependent upon the pyropheophorbide presence but was also enhanced by lipid conjugation of the porphyrin to enhance aggregation in the microstructure lipid-based microbuble shell. In a later study, Huynh et al. also managed to increase the porphyrin content 3-fold in their microbubble/microparticle assemblies to 50 molar % thereby giving rise to non-aggregated pophyrin monomers and allowing for a trimodal (fluorescence, US, PA) contrast agent (170). Their potential as trimodal contrast agents was demonstrated in KB-tumor bearing mice where B-mode US imaging allowed for soft tissue contrast from the tumor, complimenting in vivo PAI studies (Fig. 24 (b) – (e)). Ex vivo fluorescence imaging was conducted following posthumous resection of the tumor.

Inspired by these microbubble/microparticle studies, Paproski et al. later reported on smaller scale porphyrin nanodroplets (185 nm diameter) with a perfluorobutane core, which enhanced permeability and retention in tumor vasculature. Irradiation of these porphyrin nanodroplets into the porphyrin Q band at 705 nm triggered the phase-changing of the perfluorobutane nanodroplets into microbubbles enhancing US contrast (171), a phenomenon earlier reported for an liposomal india ink doped (i.e. carbon nanoparticle-based) perfluorocarbon nanodroplet (172). This result was also replicated by using US B-mode (21 MHz) imaging. Multispectral US and PAI was demonstrated in a HT1080 tumor in the chorioallantoic membrane of a chicken embryo. Also a strong PA contrast was observed from porphyrin nanodroplets in Hep3-GFP and HT1080-GFP tumors in chicken embryos after intratumoral injection. Doping the nanodroplets with Rhodamine B also allowed for complimentary fluorescence imaging confirming accumulation of the nanodroplets in the HT1080 tumor model.

Also utilizing the non-toxic pheophytin-α dye, Zhang et al. have demonstrated noninvasive, nonionizing trimodal (PA, fluorescence and PET) intestinal imaging with *surfactant-stripped induced frozen micelles* (ss-InFroMs) building upon their earlier successful study which used a naphthalocyanine based micelle (173, 174). In what is probably the first quantitative structure-activity relationship study dedicated to the optimization of MPACs, Abuteen et al. reported a series of tetrapyrrole chromophores including three quinoline-annulated porphyrins and three morpholino bacteriochlorins (Fig. 25 **41 – 46**) (175). Each of these dyes absorbed strongly in the NIR (726 – 790 nm in DMF) and exhibited 2.5-fold improvement in PA contrast compared to ICG (4) in tissue phantoms. The quinolone-annulated porphyrin derivatives **41** - **43** exhibit poor fluorescence (Φ_{fl} < 1%), excited-state lifetimes an order of magnitude shorter than the free base tetraphenylporphyrin (TPP) or ICG reference dyes, and negligible quantum yields for intersystem crossing, suggesting an

almost quantitative *LA* type PA response. The bacteriochlorin **44** and morpholinobacteriochlorin derivatives **45** and **46** ranged in absorption from 700 – 790 nm with the red shift attributed to ruffling of the typically planar macrocyclic core. A similar trend was observed for Φ_{fl} values (0.01 – 1 %) with greater structural distortion enhancing the rate of nonradiative decay and contributing to a stronger PA contrast.

In a related study, Banala et al. reported on the PAI properties for a series of Co(II), Ni(II), Cu(II) and Zn(II) metallated quinone-fused porphyrins relative to the free-base analogue and the ICG reference MPAC (Fig. 26 **47** - **50**) (176). All porphyrin derivatives exhibited intense NIR absorption ($\sim$ 65,000 M^{-1} L^{-1}) in the range 706 to 732 nm. The quinone functional groups completely quenched all fluorescence properties even for the free base and Zn(II) derivatives. All porphyrins exhibited an enhanced PA amplitude in DMF relative to ICG. The Zn(II) based system exhibited a 3.2-fold increase in PA contrast relative to ICG at just half the concentration, with the free base and Cu(II) systems following just behind. PA sensitivity at concentrations of less than 3 μM were also demonstrated in addition to PA contrast studies in swine blood and in chicken muscle phantoms at depths of up to 13 mm. The Zn(II) quinone-fused porphyrin was also investigated posthumously, after 1 h intravenous injection in a live mouse, via ex vivo multispectral optoacoustic tomography (MSOT) (177) measurements which indicated a fast liver uptake.

The synthesis, photophysical properties and in vivo PAI of a water soluble NIR absorbing tetra-PEG-ylated quinolone annulated porphyrin has been reported by Luciano et al. (Fig. 27 **51**) (178, 179). A multifold contrast enhancement in PA amplitude was reported in comparison to the ICG dye attributed to a short triplet lifetimes, low fluorescence quantum yield. Ex-vivo PAI experiments at 2.5 cm depth in an Intralipid® tissue phantom demonstrated a 4-fold greater contrast than a reference sample of rat blood under identical conditions. In vivo measurements with BALB/c tumor bearing mice demonstrated a 1.6-fold greater PA contrast relative to ICG but also a low acute toxicity and rapid renal clearance of the dye was observed.

In 2014, Lee et al. demonstrated in vivo dual-color high resolution PAI of lymphatic drainage in rat lymph nodes using a single, Pluronic F127 derived, micelle (20 nm diameter) self-assembled with two different naphthalocyanine dyes having NIR absorption at 707 and 860 nm, respectively, i.e. 5,9,14,18,23,27,32,36-octabutoxy, 2,3-naphthalocyanine (**52**) and 2,11,20,29,tetra-tert-butyl-2,3-naphthalocyanine (**53**) (Fig. 28) (180). Having successfully imaged symphatic lymph nodes at approximately 2.0 – 2.5 mm depth, PAI was again proven successful at total depths of 6 mm and 10 mm when chicken breast tissue was layered on top of the rats. Zhang et al. also used the same naphthalocyanince micelles for US and PAI of the stomach and intestine to determine real-time intestinal distribution in mice (174).

In 2016 Huang et al. described how PEG-ylation of a tin(IV) chloride octabutoxy metallonaphthalocyanine NIR absorbing dye (**54**, λ_{max} = 930 nm) prolongs its retention and circulation for improved vascular PAI (Fig. 29) (100). Intravenous administration allowed for brain vessel PAI 24 hours after injection due to a 4-fold increase in half-life and a 10-fold increase in PA contrast relative to the non-PEG-ylated control.

Similarly, Zhou et al. (181) reported on the PAI of a NIR absorbing dimethoxyphosphorous metalled phthalocyanine MPAC **55** inspired by the initial report of Furuyama (Fig. 30) (182). Utilizing its strong absorption beyond 1000 nm (λ_{max} = 997 nm in aqueous Tween 80 based micelles) the authors successfully demonstrated a strong PA contrast up to a depth of 11.6 cm of chicken breast using PA computed tomography. In vivo PAI was also demonstrated in tumor bearing mice with pancreatic MIA PaCa-2 xenografts as well as for intestinal imaging following oral administration. Remarkably, a strong PA contrast was subsequently presented through the 5 cm arm of a healthy human adult.

In 2017, Mauriello-Jimenez et al. reported on the *J*-aggregate enhancement of two-photon PDT and PAI properties of porphyrin- or phthalocyanine-bridged silsesquioxane (Fig. 31 **56** and **57**) nanoparticles (50 – 250 nm diameter) (183). Endocytosis of these tetrapyrrole based nanoparticles and their efficiency for intracellular tracking was confirmed in MCF-7 cancer cells using two-photon excited fluorescence imaging. The porphyrin derived silsesquioxane nanoparticles exhibited a more effective two-photon excited PDT activity (86% cell death) relative to the phthalocyanine analogue (21% cell death) with PTT ruled out as a contributing mechanism. The phthalocyanine-bridged silsesquioxane nanoparticles and a PEG-ylated version thereof did however exhibit a strong PAI contrast upon 700 nm irradiation in living mice following 24 h with pharmacokinetic studies confirming accumulation in the liver.

Li et al. have developed a series of eight NIR absorbing free-base porphyrin derivatives (**58** – **65**) using the tetracyanoethene(TCNE), 7,7,8,8-tetracyanoquiodimethane (TCNQ) and 2,3,5,6-tetrafluoro-7,7,8,8-tetracyanoquiodimethane (F$_4$-TCNQ) electron-withdrawing click-reagents (Fig. 32) (184). The TCNE and TCNQ electron-acceptors imparted the greatest PA properties on the porphyrin core. A single derivative containing two F$_4$-TCNQ functional groups was self-assembled into aqueous PBS soluble L-a-phosphatidylcholine:cholesterol (4:1) liposome nanoparticles (62 – 71 nm diameter) with a porphyrin:liposome mass ratio of 1:10. In vivo PAI was conducted at 860 nm in human breast cancer MCF-7 cells as a model cell line.

BODIPY dyes

BODIPY is a class of dye based upon the 4,4-difluoro-4-bora-3a,4a-diaza-s-indacene structure that has gained great popularity for its use as a fluorescent probe. In 2014, Frenette et al. used a 3,5-bis-styryl substituted BODIPY dye to refute the common hypothesis that a dye with a high fluorescence quantum yield is not an appropriate PA contrast agent (36). Using 3,5-bis-styryl (MeOPh)$_2$BODIPY dye **66** (Φ_{fl} = 0.719) its PA response was compared to that of the 1,3,5,7-tetrametyl-*meso*-(4-methoxycarbonylphenyl)BODIPY analogue **67**, the crystal violet reference **68**, curcuminBF$_2$ **69** and the Cy3 dye **70** (Fig. 33). It should be noted that the non-fluorescent crystal violet dye **68** was here demonstrated as a very effective linear absorbing MPAC standard for PA studies at 532 nm photoexcitation.

This study demonstrated that fluorophores possessing a large quantum yield, and which are capable of excited state absorption, can far exceed the PA response of linear absorbing dyes with lower quantum yields albeit dependent upon the incident laser fluence which starts to display *RSA* PA response characteristics around 125 mJ cm^{-2}. This increased PA responses

is achieved by exploiting Kasha's rule where the high laser fluence promotes two-photon absorption whereby the S_1 excited state further absorbs an incident photon to generate higher energy electronic excited states which exhibit rapid non-radiative decay back to the S_1 state (37). Irradiating bis-styryl $(MeOPh)_2$BODIPY **66** at 532 nm with a higher laser fluence of 355 mJ cm^{-2} resulted in a 13-fold increase in the PA response relative to the single photon PA response of **66** at 125 mJ cm^{-2}. Under the same conditions when going from low to high laser fluence, **69** showed a 5-fold PA increase where **68** and **70** showed a linear emission and PA response.

Li et al. have developed the photostable aza-BODIPY PA responsive ratiometric probes **71** and **72** to detect Cu(II), a metal that plays a key role in Alzheimer's disease (Fig. 34) (185). Terminal 2-picolinic ester substituents on **71** and its PEG-ylated, water soluble, analogue **72** are selectively hydrolyzed in the presence of Cu(II) resulting in an irreversible change in their photophysical properties and PA response. For example, upon Cu(II) mediated hydrolysis of the picolinic ester group from **72** probe, its absorption maximum shifts from 697 nm to 767 nm due to dissociation of the low pK_a pendant dichlorophenol group. Now amenable to 767 nm photoexcitation the PA response at this wavelength was turned on giving rise to a 91.3-fold and 100.5-fold increase in PA amplitude (relative to 697 nm excitation) in the presence of 1 and 10 equivalents of Cu(II), respectively.

In 2016, Ni et al. synthesized a water soluble NIR absorbing naphthalene fused BODIPY dimer **73** that demonstrated high photostability and a greater PA response than the ICG cyanine dye (Fig. 32) (186). The BODIPY based **73** was encapsulated into a bovine serum albumin protein for in vivo PA studies in mice bearing Hep-G2-tumors. The results showed significant passive targeting capabilities due to the increased permeability and retention of the BSA nanoparticles in tumor regions.

The same authors later reported the synthesis and PAI properties for a series of NIR absorbing 3,5-bis(vinylaryl) BODIPY dyes **74** – **77** with improved photostability relative to the ICG dye (Fig. 36) (187). The NIR absorption was strategically tuned by varying the 3,5-bis(vinylaryl) substituents between 4-(dimethylamino)phenyl (**74**), 4-(diphenylamino)phenyl (**75**), 5-(diphenylamino)thien-2-yl (**76**) and 5'-(diphenylamino)2,2'-bithiophen-5-yl (**77**). Thiophene substitution exhibited an enhanced PA contrast which was attributed to a greater intramolecular charge transfer. Bovin serum albumin nanoparticles doped with **77** were subjected to PAI studies in tissue phantoms and in vivo with a Hep-G2-tumor bearing mouse model.

BODIPY dyes have also been used as PAI based theranostic agents. Hu et al. engineered micelles composed of 1,2-distearoyl-*sn*-glycero-3-phosphoethanolamine-*N*-[methoxy(polyethylene glycol)-5000] (DSPE-mPEG5000) to sequester the bis-ethynyl bis-styryl BODIPY dye **78** (Fig. 37) capable of PAI and acid-activatible PDT (188). A549 tumor bearing mice were injected with 150 μL of 10 μg/mL **78**/micelles and irradiated at 730 nm with a 6.1 mJ cm^{-2} 5 ns laser pulse. Although such bis-styryl BODIPY dyes are capable of a *RSA* nonlinear PA response, in this case *LA* is only likely due to the low laser fluence, far below the ANSI recommend limit of exposure at 730 nm (61). A strong PA contrast was recorded just 20–30 minutes post injection with micelle clearance beginning after 50

minutes and complete clearance confirmed after 24 hours. Hu et al. attributed the highly efficient PA response to the strong fluorescence quenching effect of the dyes inside the micelles. By monitoring ROS consumption of dimalonic acid, the authors reported that at a pH of 5 the **78**/micelles consumed 30% of the dimalonic acid present in the solution over a period of 10 minutes, suggesting that the **78**/micelle combination serves as a potent PDT photosensitizer as well as a very good PA contrast agent under acidic conditions.

In their 2017 study Gawele et al. reported on the efficiency of *N*-ethylcarbazole linked iodo-aza-BODIPY dyes **79** – **82** at generating ROS for PDT applications (Fig. 38) (189). It was found that the non-iodinated aza-BODIPY dyes absorbed between 610–720 nm with a molar absorptivity of 3.0 and 3.2×10^4 M^{-1} cm^{-1} for **79** and **80** respectively. The iodinated dyes were found to have a narrower absorption with a maximum at 652 nm as well as a larger molar absorptivity of 3.7 and 4.1×10^4 M^{-1} cm^{-1} for **81** and **82**, respectively. Singlet oxygen generation efficiency of **81** and **82** was quantified by UV-Vis absorption monitoring of 1,3-diphenylisobenzofuran photooxidation in acetonitrile – a well-established assay for $^1O_2$. Functionalization with iodine enhanced the intersystem crossing efficiency of the molecules, which exhibit a phosphorescence quantum yields of roughly 0.90 and, more impressively, $^1O_2$ generation quantum yields of about 0.70 (67). The authors also demonstrated that **81** was capable of $^1O_2$ generation and sufficient simultaneous PAT contrast for imaging up to 2 cm deep in chicken tissue.

Tang et al. have synthesized a 2,6-diiodo aza-BODIPY dye **83** (Fig. 39) that was used to prepare NIR absorbing micelle nanoparticles with amphiphilic DSPE-mPEG2K for photothermal imaging (PTI), PAI and PDT studies (190). An impressive 92% quantum yield of singlet oxygen was reported following 660 nm photoexcitation making this dye very attractive as a visible photosensitizer for PDT applications. Taking advantage of its NIR absorption, photoexcitation at 730 nm yielded a photothermal conversion efficiency of 38% with negligible photodegredation. PDT studies were carried out on the BODIPY doped DSPE-mPEG2K nanoparticles in HeLA cells indirectly confirming in vitro generation of singlet oxygen using the 2',7'-dichlorofluorescein reactive oxygen species probe. In vivo studies were conducted in subcutaneous HeLA derived tumor bearing mice to demonstrate dual-modal PTI/PAI as well as synergistic PDT/PTT.

Miki et al. reported the PAI properties of PEG or PEG-ylated hyaluronic acid derived nanoparticles doped with thiophene-bridged bis-BODIPY dyes (**84**, **85**) or a dimeric fused pyrrolopyrrole aza-BODIPY dye (**86**) (Fig. 40). PEG-ylated hyaluronic acid conjugated thiophene-bridged BODIPY dimer-based nanoparticles generated the strongest in vitro PA response representing an almost 2-fold increase relative to the ICG dye in Colon26 tumor bearing mice (191). The authors hypothesized that not only was BODIPY aggregation essential for PA enhancement, but also optimization of the elastic modulus of the self-assembled polymer nanomaterial. The thiophene-bridged BODIPY dimer doped PEG-ylated hyaluronic acid nanoparticle also exhibited an enhanced EPR effect in vivo relative to an analogous ICG doped nanoparticle.

In 2018, Reinhardt et al. have reported the first PA probes **87** – **90** for in vivo ratiometric nitric oxide (NO) detection based upon the aza-BODIPY chromophore (Fig. 41), whereby

the NO molecule forms an *N*-nitroso adduct at a pendant secondary amine of the dye causing a 91 nm blue shift in its $S_0 \rightarrow S_1$ absorption band (192). These NO probes exhibited a high selectivity for NO addition over a variety of biologically relevant analytes and in vivo detection of endogenous NO was successfully achieved using a murine lipopolysaccharide-induced inflammation model.

Curcumin dyes

The bright yellow curcumin pigment, which occurs naturally in the rhizomes of the curcuma longa plant, has long been touted to possess antibacterial, antiviral, antifungal, and anti-tumor properties that have attracted a lot of attention from biomedical researchers (193). In addition to the biologically active properties that has peaked interest in the curcumin pigment, it has also become of interest as a molecular contrast agent for PAI. As briefly discussed earlier, Frenette et al. first demonstrated that the borondifluoride curcumin derivative **69** exhibits a nonlinear 5-fold increase in PA response due to two-photon absorption at high laser fluences (Fig. 33) (36). This observation prompted a more comprehensive investigation where the photophysical properties of the curcumin pigment were modified by variation of its terminal functional groups. In 2018 Bellinger et al. reported on a series of quadrupolar donor-π-acceptor-π-donor curcuminBF$_2$ dyes where incorporation of π-extended aryl and tertiary arylamine electron donating substituents at the terminal position of the β-diketonate borondifluoride backbone enabled tuning of their absorption and emission spectra and ultimately their PA response (Fig. 42) (194). Absorption maxima ranged from 495 nm ($\varepsilon = 8.85 \times 10^4$ M^{-1} cm^{-1}) for the simple bis(phenyl)curcuminBF$_2$ derivative to 578 nm ($\varepsilon = 1.17 \times 10^5$ M^{-1} cm^{-1}) for the bis(triphenylamine)curcuminBF$_2$ derivative when recorded in toluene. Increasing electron-donating strength of the terminal curcuminBF$_2$ substituents had the general impact of not only red-shifting the absorption and fluorescence emission maxima but also of increasing the molar extinction coefficient with the bis(*p*-dimethylaminophenyl)curcuminBF$_2$ exhibiting an impressive absorptivity of $\varepsilon = 1.63 \times 10^5$ M^{-1} cm^{-1} at 572 nm. Fluorescence emission quantum yields Φ_{fl} ranged from 0.23 for the bis(pyrene)curcuminBF$_2$ dye to 0.77 for bis(*p*-dimethylaminophenyl)curcuminBF$_2$ also recorded in toluene, however all dyes exhibited strong solvatochromism with a sharp drop in Φ_{fl} upon switching to acetonitrile. Limited to 532 nm laser excitation and using by PA coupled optical z-scan spectroscopy (aka OPAZ), a broad range of *SA*, *LA* and *RSA* type behavior was observed across the series of then curcuminBF$_2$ derivatives depending upon the excited state absorption cross-section and lifetime as well as the laser fluence. Interestingly, all curcuminBF$_2$ dyes exhibited a stronger PA response than the Cy3 cyanine-based dye, and most performed on par with the ideal *LA* crystal violet dye which was previous touted by the authors as an excellent and quantitative standard for PA studies. In particular, the bis(naphtha)curcuminBF$_2$ and bis(carbazole)curcuminBF$_2$ dyes exhibited a strong *RSA* nonlinear enhancement in their PA response upon increasing laser fluence. A result which was further corroborated by PA tomography studies (Fig. 42). Although curcumin dyes exhibit highly promising properties as potential in vivo MPACs the authors also pointed out their questionable photostability in protic solvents, thus aqueous compatability and NIR absorption are two challenges that must be met for this class of MPAC.

Miscellaneous studies

Ho et al. published the first explicitly comparative study for a series of MPACs in 2014 (140). The goal of this study was to focus only on established PDT agents such that a dual-functional PA-PDT theranostic agent could be identified. The series of five dyes investigated included zinc phthalocyanine (**96**), protoporphyrin IX (**38**), 2,4-bis[4-(N,N-dibenzylamino)-2,6-dihydroxyphenyl]squaraine (**30**), chlorin e6 (**97**) and methylene blue (**26**). While each of these dyes belong to a family of chromophores already classified above (i.e. tetrapyrrole, squaraine and xanthene), along with Brückner's prior synthetic approach to MPAC design (175, 179, 195), this represented a paradigm shift in how the scientific community was approaching the topic of MPAC choice, in contrast to earlier empirical approaches by simply choosing a poor fluorophore. Using phantom studies Ho et al. identified **96** as the most proficient MPAC from the series of dyes investigated. While PDT studies where not reported in tandem, in vivo PAI was reported for **96** confirming tumor localization in a MCF-7 tumor bearing mice (Fig. 43). This led the authors to conclude that PDT photosensitizers which exhibit a suitable EPR effect can also be used effectively as PA contrast agents to establish real-time in vivo diagnosis of cancer treatment.

In 2015 Fan et al. developed perylene-diimide (**98**) doped micelles to provide PA contrast for diagnostic imaging of deep brain tissue in glioblastoma tumor bearing mice (196). A secondary amine substituted NIR absorbing perylene diimide (λ_{max} = 700 nm) was incorporated into a 1,2-distearoyl-sn-glycero-3-phosphoethanolamine methoxy-PEG5K (DSPE-mPEG5K) based amphiphilic micelle (diameter ~ 48 – 53 nm) and exhibited excellent photostability in contrast to the reference ICG dye (Fig. 44) (196). In vivo PAI was conducted on orthotopic glioblastoma tumor models by implanting C6-Fluc cells confirming an enhanced EPR effect of the micelles 1 and 2 days post injection at 3 mm and 4 mm depth, respectively, at the tumor site.

A benzobisthiadiazole dye, specifically, benzo[1,2-c;4,5-c']bis[1,2,5]thiadiazole-4,7-bis(9,9-dioctyl-9H-fluoren-2-yl)thiophene (**99**), encapsulated in a β-caprolactone derived amphiphilic block polymer PEG-b-PCL micelle (diameter ~ 46 – 68 nm), was demonstrated by Huang et al. to exhibit theranostic properties as a MPAC and PTT agent (Fig. 45) (197). Taking advantage of its strong and broad NIR absorption at 880 nm, laser excitation (808 nm) with a photothermal conversion efficiency of 40% resulted in rapid and quantitative detail of HeLa cells. Ex vivo PAI in phantoms confirmed a 10-fold greater contrast for the benzobisthiadiazole dye-based micelles relative to an animal blood pseudo-endogenous reference. Further depth profiling established a clear PA contrast beneath chicken breast tissue at depths of up to 4 cm.

Prior to the related porphyrin-based study discussed above by Li et al. (184), the influence of the F_4-TCNQ electron-acceptor on the PA and photothermal properties of simpler diphenylacetylene click-derived dyes was reported (Fig. 46 **100** - **103**) (198). Using a secondary amine electron-donor to introduce a strong donor-π-acceptor charge-transfer electronic transition the four dyes presented impressively strong NIR absorption (ε ~ 10^4 M^{-1} cm^{-1}) in the range of 790 to 831 nm. MSOT measurements confirmed a significantly greater PA response of all four dyes relative to the ICG reference dye in the photoexcitation

range of 700 – 960 nm. The aldehyde functionalized dye **103** was subsequently sequestered into a L-α-phosphatidylcholine:cholesterol (4:1) based micelle (diameter = 79 nm) and imaged by PAT in MCF-7 tumor bearing mice.

Hatamimoslehabadi et al. have reported on the optical and PA properties for a wide range of eleven established, and readily accessible, molecular dyes whose properties varied from symmetric vs. asymmetric, organic vs. inorganic, neutral vs. cationic, fluorescent vs. phosphorescent, albeit with all dyes restricted to 532 nm excitation outside of the biological transparency window (Fig. 47) (199). Bearing the structural, and photophysical diversity of this series in mind, all dyes could be categorized according to the *LA*, *SA* and *RSA* criteria set out in the introduction of this review. The majority of dyes investigated by Hatamimoslehabadi et al. have already been reported independently as MPACS and have been discussed already in this review, i.e. rhodamine B (**23**), methylene blue (**26**), BODIPY (**67**), crystal violet (**68**), curcuminBF$_2$ (**69**). The series of dyes investigated by Hatamimoslehabadi et al. also included zinc(II) *meso*-tetraphenylporphyrin (**104**), nile red (**105**), merocyanine 540 (**106**), C$_{60}$ (**107**) and ruthenium tris(2,2'-bipyridine) (**108**) previously unreported as PA contrast agents. The excellent *LA* properties of **68** imparted it with the strongest observable PA signal under low laser fluence conditions. A concentration dependence of PA emission across the series of dyes (conducted at 13 mJ cm^{-2} and 366 mJ cm^{-2} laser fluences) demonstrated that while the PA response under a *LA* regime is still influenced by the non-radiative rate constant of each dye, the overall trend in PA amplitudes was found to be strongly correlated to the magnitude of the S$_0$ → S$_1$ molar extinction coefficient at the excitation wavelength. In the *RSA* regime at high laser fluence (366 mJ cm^{-2}) **104** exhibited the strongest nonlinear behavior with a 3.8-fold enhancement relative to the linear PA response of crystal violet. Similarly, **105** and **26** exhibited nonlinear enhancements of 2.15-fold and 1.38-fold, respectively, relative to **68**.

In 2018 Roberts et al. have reported a cell-permeable merocyanine-based PA calcium sensor which possesses a high selectivity for Ca^{2+} binding by use of the 1,2-bis(*o*-aminophenoxy)ethane-*N*,*N*,*N*′,*N*′-tetraacetic acid (BAPTA) chelator (200). The calcium-free dye exhibits a λ$_{max}$ at 590 nm (ε = 116,500 M^{-1} cm^{-1}) whose cell permeability was enhanced by incorporation of an acetoxymethyl ester group. In vitro bimodal fluorescence and PA probed calcium sensing was reported with Chinese hamster ovary (CHO) cells and human embryonic kidney (HEK 293) cells, where calcium influxe was induced by the Br-A23187 calcium-specific ionophore realizing a 50% decrease in PA contrast confirmed by two-photon PA microscopy. The calcium sensing properties of this probe were also tested in vitro using cultured heart organoids and successfully correlated with the established green fluorescent calcium indicator Fluo-4-AM. Futhermore, time-resolved fluxes in calcium concentration where also measured in vivo using with zebrafish larval brain subjects.

CONCLUSIONS

The rapidly growing field of PAI and the increasing interest in engineering advanced exogenous, molecular-based, PA contrast agents has warranted an up-to-date comprehensive review of the available literature to date. The fundamental design principles of MPACs has been presented delineating a contrast agent's PA response based upon their photophysical

properties, and properties of the excitation laser pulse. While a conventional design of MPACs is certainly applicable and most relevant to currently meet ANSI limitations for in vivo PAI (re. Eq. 1), molecular dyes with large fluorescence (Φ_{fl}), or phosphorescence (Φ_{ph}), quantum yields are capable of generating an amplified PA response via a nonlinear photon absorption and enriched non-radiative decay pathway (re. Eq. 3). Photophysical characteristics which determines MPAC classification as a linear absorber (*LA*), saturable absorber (*SA*) or reverse-saturable absorber (*RSA*) include the ground state molar extinction coefficient (ε_g), the excited state molar extinction coefficient (ε_e) and the excited state lifetime (τ). Literature examples have been highlighted which demonstrated the exciting potential of *RSA* materials for PAI, however significant progress must be made going forward to develop biologically compatible *RSA* materials that exhibit a nonlinear PA response upon photoexcitation in the biological window, whilst also increasing their optical-limiting properties for application at lower, more benign and ANSI compatible laser fluences. Although the variety of exogenous MPACs may appear diverse in design, as illustrated in this review, all but a few MPACs belong to a small recognizable family of established chromophores, i.e. cyanines, phthaleins and xanthenes, tetrapyrroles and BODIPY, squaraines and croconaines. Although, intense research is currently underway at engineering unique MPACs for enhanced NIR light absorption and PA contrast, significant steps must be taken as this research field grows to better understand and tailor the biological properties of MPACs in order to maximize their impact in in order to be approved in animal models of disease for practical applications.

ACKNOWLEDGMENTS:

REFERENCES

1. Bell AG (1880). "Upon the production and reproduction of sound by light." Telegraph Engineers, Journal of the Society of 9(34): 404–426.

2. Xu MH and Wang LHV (2006). "Photoacoustic imaging in biomedicine." Rev. Sci. Instrum. 77(4).

3. Kim C, Favazza C and Wang LHV (2010). "In Vivo Photoacoustic Tomography of Chemicals: High-Resolution Functional and Molecular Optical Imaging at New Depths." Chem. Rev. 110(5): 2756–2782. [PubMed: 20210338]

4. Ntziachristos V and Razansky D (2010). "Molecular Imaging by Means of Multispectral Optoacoustic Tomography (MSOT)." Chem. Rev. 110(5): 2783–2794. [PubMed: 20387910]

5. Luo SL, Zhang EL, Su YP, Cheng TM and Shi CM (2011). "A review of NIR dyes in cancer targeting and imaging." Biomaterials 32(29): 7127–7138. [PubMed: 21724249]

6. Mallidi S, Luke GP and Emelianov S (2011). "Photoacoustic imaging in cancer detection, diagnosis, and treatment guidance." Trends Biotechnol. 29(5): 213–221. [PubMed: 21324541]

7. Yuan L, Lin WY, Zheng KB, He LW and Huang WM (2013). "Far-red to near infrared analyte-responsive fluorescent probes based on organic fluorophore platforms for fluorescence imaging." Chem. Soc. Rev. 42(2): 622–661. [PubMed: 23093107]

8. Li K and Liu B (2014). "Polymer-encapsulated organic nanoparticles for fluorescence and photoacoustic imaging." Chem. Soc. Rev. 43(18): 6570–6597. [PubMed: 24792930]

9. Nie LM and Chen XY (2014). "Structural and functional photoacoustic molecular tomography aided by emerging contrast agents." Chem. Soc. Rev. 43(20): 7132–7170. [PubMed: 24967718]

10. Wang LV and Gao L (2014). "Photoacoustic Microscopy and Computed Tomography: From Bench to Bedside." Annu. Rev. Biomed. Eng. 16(1): 155–185. [PubMed: 24905877]

11. Wu D, Huang L, Jiang MS and Jiang HB (2014). "Contrast Agents for Photoacoustic and Thermoacoustic Imaging: A Review." Int. J. Mol. Sci. 15(12): 23616–23639. [PubMed: 25530615]

12. Zackrisson S, van de Ven SMWY and Gambhir SS (2014). "Light In and Sound Out: Emerging Translational Strategies for Photoacoustic Imaging." Cancer Res. 74(4): 979–1004. [PubMed: 24514041]

13. Weber J, Beard PC and Bohndiek SE (2016). "Contrast agents for molecular photoacoustic imaging." Nat. Methods 13(8): 639–650. [PubMed: 27467727]

14. Wang S, Lin J, Wang TF, Chen XY and Huang P (2016). "Recent Advances in Photoacoustic Imaging for Deep-Tissue Biomedical Applications." Theranostics 6(13): 2394–2413. [PubMed: 27877243]

15. Wang LHV and Yao JJ (2016). "A practical guide to photoacoustic tomography in the life sciences." Nat. Methods 13(8): 627–638. [PubMed: 27467726]

16. Zhang JC, Qiao ZY, Yang PP, Pan J, Wang L and Wang H (2015). "Recent Advances in Near-Infrared Absorption Nanomaterials as Photoacoustic Contrast Agents for Biomedical Imaging." Chin. J. Chem. 33(1): 35–52.

17. Lemons RA and Quate CF (1974). "Acoustic microscope—scanning version." Appl. Phys. Lett. 24(4): 163–165.

18. Bowen T (1981). Radiation-Induced Thermoacoustic Soft Tissue Imaging. 1981 Ultrasonics Symposium: 817–822.

19. Danielli A, Maslov K, Favazza CP, Xia J and Wang LHV (2015). "Nonlinear photoacoustic spectroscopy of hemoglobin." Appl. Phys. Lett. 106(20).

20. Maeda H (2010). "Tumor-Selective Delivery of Macromolecular Drugs via the EPR Effect: Background and Future Prospects." Bioconjugate Chem. 21(5): 797–802.

21. Reinhardt CJ and Chan J (2018). "Development of Photoacoustic Probes for in Vivo Molecular Imaging." Biochemistry 57(2): 194–199. [PubMed: 29022344]

22. Wang L, Yang PP, Zhao XX and Wang H (2016). "Self-assembled nanomaterials for photoacoustic imaging." Nanoscale 8(5): 2488–2509. [PubMed: 26757620]

23. Van Stryland EW and Sheik-Bahae M (1998). "Z-scan measurements of optical nonlinearities." Characterization techniques and tabulations for organic nonlinear materials 18.

24. Yelleswarapu CS and Kothapalli S-R (2010). "Nonlinear photoacoustics for measuring the nonlinear optical absorption coefficient." Opt. Express 18(9): 9020–9025. [PubMed: 20588748]

25. Chantharasupawong P, Philip R and Thomas J (2013). "Simultaneous optical and photoacoustic measurement of nonlinear absorption." Appl. Phys. Lett. 102(4): 041116.

26. Chandrasekharan N, Gonzales B and Cullum BM (2004). "Non-resonant multiphoton photoacoustic spectroscopy for noninvasive subsurface chemical diagnostics." Appl. Spectrosc. 58(11): 1325–1333. [PubMed: 15606938]

27. Wang LV and Hu S (2012). "Photoacoustic tomography: in vivo imaging from organelles to organs." Science 335(6075): 1458–1462. [PubMed: 22442475]

28. Zhang C, Maslov K, Yao JJ and Wang LHV (2012). "In vivo photoacoustic microscopy with 7.6-mu m axial resolution using a commercial 125-MHz ultrasonic transducer." J. Biomed. Opt. 17(11).

29. Hai P, Yao J, Maslov KI, Zhou Y and Wang LV (2014). "Near-infrared optical-resolution photoacoustic microscopy." Opt. Lett. 39(17): 5192–5195. [PubMed: 25166107]

30. Park S, Vial J-C and Kyhm K (2017). "Optical sectioning in optical resolution photo acoustic microscopy." Opt. Express 25(16): 18917–18928. [PubMed: 29041083]

31. Valluru KS and Willmann JK (2016). "Clinical photoacoustic imaging of cancer." Ultrasonography 35(4): 267–280. [PubMed: 27669961]

32. McNally LR, Mezera M, Morgan DE, Frederick PJ, Yang ES, Eltoum IE and Grizzle WE (2016). "Current and Emerging Clinical Applications of Multispectral Optoacoustic Tomography (MSOT) in Oncology." Clin. Cancer Res. 22(14): 3432–3439. [PubMed: 27208064]

33. Escobedo JO, Rusin O, Lim S and Strongin RM (2010). "NIR dyes for bioimaging applications." Curr. Opin. Chem. Biol. 14(1): 64–70. [PubMed: 19926332]

34. Knopoff L and Shapiro JN (1970). "Pseudo-Grueneisen Parameter for Liquids." Phys. Rev. B 1(10): 3893–3895.

35. Frenette M, Hatamimoslehabadi M, Bellinger-Buckley S, Laoui S, Bag S, Dantiste O, Rochford J and Yelleswarapu C (2014). "Nonlinear optical properties of multipyrrole dyes." Chem. Phys. Lett. 608(0): 303–307. [PubMed: 25242819]

36. Frenette M, Hatamimoslehabadi M, Bellinger-Buckley S, Laoui S, La J, Bag S, Mallidi S, Hasan T, Bouma B, Yelleswarapu C and Rochford J (2014). "Shining Light on the Dark Side of Imaging: Excited State Absorption Enhancement of a Bis-styryl BODIPY Photoacoustic Contrast Agent." J. Am. Chem. Soc. 136(45): 15853–15856. [PubMed: 25329769]

37. Kasha M (1950). "Characterization of electronic transitions in complex molecules." Disc. Faraday Soc. 9(0): 14–19.

38. Christodoulides DN, Khoo IC, Salamo GJ, Stegeman GI and Van Stryland EW (2010). "Nonlinear refraction and absorption: mechanisms and magnitudes." Adv. Opt. Photonics 2(1): 60–200.

39. Yamaoka Y and Takamatsu T (2009). Enhancement of multiphoton excitation-induced photoacoustic signals by using gold nanoparticles surrounded by fluorescent dyes. SPIE BiOS, SPIE. 7177: 9.

40. Yamaoka Y, Nambu M and Takamatsu T (2010). Frequency-selective multiphoton-excitation-induced photoacoustic microscopy (MEPAM) to visualize the cross sections of dense objects. SPIE BiOS, SPIE. 7564: 9.

41. Raaij M. E. v., Lee M, Chérin E, Stefanovic B and Foster FS (2010). Femtosecond photoacoustics: integrated two-photon fluorescence and photoacoustic microscopy. SPIE BiOS, SPIE. 7564: 6.

42. Shelton RL and Applegate BE (2010). "Ultrahigh resolution photoacoustic microscopy via transient absorption." Biomed. Opt. Express 1(2): 676–686. [PubMed: 21258499]

43. Yamaoka Y, Nambu M and Takamatsu T (2011). "Fine depth resolution of two-photon absorption-induced photoacoustic microscopy using low-frequency bandpass filtering." Opt. Express 19(14): 13365–13377. [PubMed: 21747492]

44. Langer G, Bouchal KD, Grun H, Burgholzer P and Berer T (2013). "Two-photon absorption-induced photoacoustic imaging of Rhodamine B dyed polyethylene spheres using a femtosecond laser." Opt. Express 21(19): 22410–22422. [PubMed: 24104130]

45. Lai Y-H, Lee S-Y, Chang C-F, Cheng Y-H and Sun C-K (2014). "Nonlinear photoacoustic microscopy via a loss modulation technique: from detection to imaging." Opt. Express 22(1): 525–536. [PubMed: 24515013]

46. Lee S-Y, Lai Y-H, Huang K-C, Chen Y-C and Sun C-K (2014). Realization of Multiphoton Photoacoustic Microscopy via a Loss Modulation Technique CLEO: 2014. San Jose, California, Optical Society of America: JW2A30.

47. Mattison SP and Applegate BE (2014). "Simplified method for ultra high-resolution photoacoustic microscopy via transient absorption." Opt. Lett. 39(15): 4474–4477. [PubMed: 25078206]

48. Sarimollaoglu M, Nedosekin DA, Menyaev YA, Juratli MA and Zharov VP (2014). "Nonlinear photoacoustic signal amplification from single targets in absorption background." Photoacoustics 2(1): 1–11. [PubMed: 24921062]

49. Shelton RL, Mattison SP and Applegate BE (2014). "Molecular specificity in photoacoustic microscopy by time-resolved transient absorption." Opt. Lett. 39(11): 3102–3105. [PubMed: 24875987]

50. Wei CW, Lombardo M, Larson-Smith K, Pelivanov I, Perez C, Xia J, Matula T, Pozzo D and O'Donnell M (2014). "Nonlinear contrast enhancement in photoacoustic molecular imaging with gold nanosphere encapsulated nanoemulsions." Appl. Phys. Lett. 104(3).

51. Yamaoka Y, Harada Y, Sakakura M, Minamikawa T, Nishino S, Maehara S, Hamano S, Tanaka H and Takamatsu T (2014). "Photoacoustic microscopy using ultrashort pulses with two different pulse durations." Opt. Express 22(14): 17063–17072. [PubMed: 25090520]

52. Goy AS and Fleischer JW (2015). "Resolution enhancement in nonlinear photoacoustic imaging." Appl. Phys. Lett. 107(21).

53. Tian C, Xie ZX, Fabiilli ML and Wang XD (2015). "Imaging and sensing based on dual-pulse nonlinear photoacoustic contrast: a preliminary study on fatty liver." Opt. Lett. 40(10): 2253–2256. [PubMed: 26393712]

54. Gao F, Bai L, Feng X, Tham HP, Zhang R, Zhang Y, Liu S, Zhao L, Zheng Y and Zhao Y (2016). "Remarkable In Vivo Nonlinear Photoacoustic Imaging Based on Near-Infrared Organic Dyes." Small 12(38): 5239–5244. [PubMed: 27490362]

55. Mark J, Schmitt FJ and Laufer J (2016). "Photoacoustic imaging of the excited state lifetime of fluorophores." J. Optics 18(5).

56. Gao F, Bai LY, Liu SY, Zhang RC, Zhang JT, Feng XH, Zheng YJ and Zhao YL (2017). "Rationally encapsulated gold nanorods improving both linear and nonlinear photoacoustic imaging contrast in vivo." Nanoscale 9(1): 79–86. [PubMed: 27911452]

57. Gao F, Feng XH, Zhang RC, Liu SY, Ding R, Kishor R and Zheng YJ (2017). "Single laser pulse generates dual photoacoustic signals for differential contrast photoacoustic imaging." Sci. Rep. 7.

58. Mattison SP, Mondragon E, Kaunas R and Applegate BE (2017). "Hybrid nonlinear photoacoustic and reflectance confocal microscopy for label-free subcellular imaging with a single light source." Opt. Lett. 42(19): 4028–4031. [PubMed: 28957189]

59. Wang DP, Wei W, Singh A, He GS, Kannan R, Tan LS, Chen GY, Prasad PN and Xia J (2017). "Nonlinear Photoacoustic Imaging by in Situ Multiphoton Upconversion and Energy Transfer." Acs Photonics 4(11): 2699–2705. [PubMed: 30246053]

60. Malekzadeh-Najafabadi J, Prakash J and Ntziachristos V (2018). "Nonlinear optoacoustic readings from diffusive media at near-infrared wavelengths." J. Biophotonics 11(1).

61. Delori FC, Webb RH and Sliney DH (2007). "Maximum permissible exposures for ocular safety (ANSI 2000), with emphasis on ophthalmic devices." J. Opt. Soc. Am. A Opt. Image Sci. Vis. 24(5): 1250–1265. [PubMed: 17429471]

62. Liu Y, Zhang C and Wang LHV (2012). "Effects of light scattering on optical-resolution photoacoustic microscopy." J. Biomed. Opt. 17(12).

63. Strohm EM, Berndl ESL and Kolios MC (2013). "High frequency label-free photoacoustic microscopy of single cells." Photoacoustics 1(3–4): 49–53. [PubMed: 25302149]

64. Mishra A, Behera RK, Behera PK, Mishra BK and Behera GB (2000). "Cyanines during the 1990s: A review." Chem. Rev. 100(6): 1973–2011. [PubMed: 11749281]

65. Taniguchi M and Lindsey JS (2018). "Database of Absorption and Fluorescence Spectra of >300 Common Compounds for use in PhotochemCAD." Photochem. Photobiol. 94(2): 290–327. [PubMed: 29166537]

66. Braslavsky SE and Heibel GE (1992). "Time-Resolved Photothermal and Photoacoustic Methods Applied to Photoinduced Processes in Solution." Chem. Rev. 92(6): 1381–1410.

67. Churio MS, Angermund KP and Braslavsky SE (1994). "Combination of Laser-Induced Optoacoustic Spectroscopy (LIOAS) and Semiempirical Calculations for the Determination of Molecular Volume Changes - The Photoisomerization of Carbocyanines." J. Phys. Chem. 98(7): 1776–1782.

68. Tocho JO, Murphy M, Rodriguez E and Cusso F (1994). "Simultaneous Photoacoustic and Luminescence Multiple Wavelength Experiments." J. Phys. IV 4(C7): 405–408.

69. Ballou B, Ernst LA and Waggoner AS (2005). "Fluorescence imaging of tumors in vivo." Curr. Med. Chem. 12(7): 795–805. [PubMed: 15853712]

70. Philip R, Penzkofer A, Baumler W, Szeimies RM and Abels C (1996). "Absorption and fluorescence spectroscopic investigation of indocyanine green." J. Photochem. Photobio. A: Chem. 96(1–3): 137–148.

71. Pauli J, Vag T, Haag R, Spieles M, Wenzel M, Kaiser WA, Resch-Genger U and Hilger I (2009). "An in vitro characterization study of new near infrared dyes for molecular imaging." Eur. J. Med. Chem. 44(9): 3496–3503. [PubMed: 19269067]

72. Kusano M, Tajima Y, Yamazaki K, Kato M, Watanabe M and Miwa M (2008). "Sentinel node mapping guided by indocyanine green fluorescence imaging: A new method for sentinel node navigation surgery in gastrointestinal cancer." Dig. Surg. 25(2): 103–108. [PubMed: 18379188]

73. Song FL, Peng XJ, Lu EH, Rong Z, Chen XY and Bo S (2004). "Syntheses, spectral properties and photo stabilities of novel water-soluble near-infrared cyanine dyes." J. Photochem. Photobio. A: Chem. 168(1–2): 53–57.

74. Lin YH, Weissleder R and Tung CH (2002). "Novel near-infrared cyanine fluorochromes: Synthesis, properties, and bioconjugation." Bioconjugate Chem. 13(3): 605–610.

75. Mordon S, Devoisselle JM, Soulie-Begu S and Desmettre T (1998). "Indocyanine green: Physicochemical factors affecting its fluorescence in vivo." Microvasc. Res. 55(2): 146–152. [PubMed: 9521889]

76. Devoisselle JM, Soulie-Begu S, Mordon S, Desmettre T and Maillols H (1998). "A preliminary study of the in vivo behaviour of an emulsion formulation of indocyanine green." Lasers in Medical Science 13(4): 279–282. [PubMed: 24710988]

77. Shi C, Wu JB and Pan D (2016). "Review on near-infrared heptamethine cyanine dyes as theranostic agents for tumor imaging, targeting, and photodynamic therapy." J. Biomed. Opt. 21(5): 050901–050901.

78. Schaafsma BE, Mieog JSD, Hutteman M, Van der Vorst JR, Kuppen PJK, Lowik C, Frangioni JV, Van de Velde CJH and Vahrmeijer AL (2011). "The Clinical Use of Indocyanine Green as a Near-Infrared Fluorescent Contrast Agent for Image-Guided Oncologic Surgery." J. Surg. Oncol. 104(3): 323–332. [PubMed: 21495033]

79. Kim G, Huang SW, Day KC, O'Donnell M, Agayan RR, Day MA, Kopelman R and Ashkenazi S (2007). "Indocyanine-green-embedded PEBBLEs as a contrast agent for photoacoustic imaging." J. Biomed. Opt. 12(4).

80. Yoon HK, Ray A, Lee YEK, Kim G, Wang XD and Kopelman R (2013). "Polymer-protein hydrogel nanomatrix for stabilization of indocyanine green towards targeted fluorescence and photoacoustic bio-imaging." J. Mater. Chem. B 1(41): 5611–5619.

81. Zhong JP, Yang SH, Zheng XH, Zhou T and Xing D (2013). "In vivo photoacoustic therapy with cancer-targeted indocyanine green-containing nanoparticles." Nanomed. 8(6): 903–919.

82. Zhong JP and Yang SH (2014). "Contrast-enhanced photoacoustic imaging using indocyanine green-containing nanoparticles." J. Innov. Opt. Health Sci. 7(1).

83. Beziere N, Lozano N, Nunes A, Salichs J, Queiros D, Kostarelos K and Ntziachristos V (2015). "Dynamic imaging of PEGylated indocyanine green (ICG) liposomes within the tumor microenvironment using multi-spectral optoacoustic tomography (MSOT)." Biomaterials 37: 415–424. [PubMed: 25453969]

84. Miki K, Inoue T, Kobayashi Y, Nakano K, Matsuoka H, Yamauchi F, Yano T and Ohe K (2015). "Near-Infrared Dye-Conjugated Amphiphilic Hyaluronic Acid Derivatives as a Dual Contrast Agent for In Vivo Optical and Photoacoustic Tumor Imaging." Biomacromolecules 16(1): 219–227. [PubMed: 25402751]

85. Chen Z, Zhao PF, Luo ZY, Zheng MB, Tian H, Gong P, Gao GH, Pan H, Liu LL, Ma AQ, Cui HD, Ma YF and Cai LT (2016). "Cancer Cell Membrane-Biomimetic Nanoparticles for Homologous-Targeting Dual-Modal Imaging and Photothermal Therapy." ACS Nano 10(11): 10049–10057. [PubMed: 27934074]

86. Tan XX, Wang JP, Pang XJ, Liu L, Sun Q, You Q, Tan FP and Li N (2016). "Indocyanine Green-Loaded Silver Nanoparticle@Polyaniline Core/Shell Theranostic Nanocomposites for Photoacoustic/Near-Infrared Fluorescence Imaging-Guided and Single-Light-Triggered Photothermal and Photodynamic Therapy." ACS Appl. Mater. Interfaces 8(51): 34991–35003. [PubMed: 27957854]

87. Wang GH, Zhang F, Tian R, Zhang LW, Fu GF, Yang LL and Zhu L (2016). "Nanotubes-Embedded Indocyanine Green-Hyaluronic Acid Nanoparticles for Photoacoustic-Imaging-Guided Phototherapy." ACS Appl. Mater. Interfaces 8(8): 5608–5617. [PubMed: 26860184]

88. Gao S, Wang GH, Qin ZN, Wang XY, Zhao GQ, Ma QJ and Zhu L (2017). "Oxygen-generating hybrid nanoparticles to enhance fluorescent/photoacoustic/ultrasound imaging guided tumor photodynamic therapy." Biomaterials 112: 324–335. [PubMed: 27776285]

89. Liang XL, Fang L, Li XD, Zhang X and Wang F (2017). "Activatable near infrared dye conjugated hyaluronic acid based nanoparticles as a targeted theranostic agent for enhanced fluorescence/CT/

photoacoustic imaging guided photothermal therapy." Biomaterials 132: 72–84. [PubMed: 28411450]

90. Thawani JP, Amirshaghaghi A, Yan LS, Stein JM, Liu J and Tsourkas A (2017). "Photoacoustic-Guided Surgery with Indocyanine Green-Coated Superparamagnetic Iron Oxide Nanoparticle Clusters." Small 13(37).

91. Laufer J, Zhang E and Beard P (2010). "Evaluation of Absorbing Chromophores Used in Tissue Phantoms for Quantitative Photoacoustic Spectroscopy and Imaging." IEEE J. Sel. Top. Quantum Electron 16(3): 600–607.

92. Guo M, Mao HJ, Li YL, Zhu AJ, He H, Yang H, Wang YY, Tian X, Ge CC, Peng QL, Wang XY, Yang XL, Chen XY, Liu G and Chen HB (2014). "Dual imaging-guided photothermal/photodynamic therapy using micelles." Biomaterials 35(16): 4656–4666. [PubMed: 24613048]

93. Temma T, Onoe S, Kanazaki K, Ono M and Saji H (2014). "Preclinical evaluation of a novel cyanine dye for tumor imaging with in vivo photoacoustic imaging." J. Biomed. Opt. 19(9).

94. Onoe S, Temma T, Kanazaki K, Ono M and Saji H (2015). "Development of photostabilized asymmetrical cyanine dyes for in vivo photoacoustic imaging of tumors." J. Biomed. Opt. 20(9).

95. Rai P, Mallidi S, Zheng X, Rahmanzadeh R, Mir Y, Elrington S, Khurshid A and Hasan T (2010). "Development and applications of photo-triggered theranostic agents." Adv. Drug Deliv. Rev. 62(11): 1094–1124. [PubMed: 20858520]

96. Liu T-M, Conde J, Lipi ski T, Bednarkiewicz A and Huang C-C (2017). "Smart NIR linear and nonlinear optical nanomaterials for cancer theranostics: Prospects in photomedicine." Prog. Mater. Sci. 88, 89–135.

97. Nani RR, Gorka AP, Nagaya T, Yamamoto T, Ivanic J, Kobayashi H and Schnermann MJ (2017). "In Vivo Activation of Duocarmycin–Antibody Conjugates by Near-Infrared Light." ACS Cent. Sci. 3(4): 329–337. [PubMed: 28470051]

98. Kanazaki K, Sano K, Makino A, Takahashi A, Deguchi J, Ohashi M, Temma T, Ono M and Saji H (2014). "Development of human serum albumin conjugated with near-infrared dye for photoacoustic tumor imaging." J. Biomed. Opt. 19(9).

99. Kanazaki K, Sano K, Makino A, Yamauchi F, Takahashi A, Homma T, Ono M and Saji H (2016). "Feasibility of poly(ethylene glycol) derivatives as diagnostic drug carriers for tumor imaging." J. Control. Release 226: 115–123. [PubMed: 26869546]

100. Huang HY, Wang DP, Zhang YZ, Zhou Y, Geng JM, Chitgupi U, Cook TR, Xia J and Lovell JF (2016). "Axial PEGylation of Tin Octabutoxy Naphthalocyanine Extends Blood Circulation for Photoacoustic Vascular Imaging." Bioconjugate Chem. 27(7): 1574–1578.

101. Huynh E, Lovell JF, Helfield BL, Jeon M, Kim C, Goertz DE, Wilson BC and Zheng G (2012). "Porphyrin Shell Microbubbles with Intrinsic Ultrasound and Photoacoustic Properties." J. Am. Chem. Soc. 134(40): 16464–16467. [PubMed: 22827774]

102. Hannah A, Luke G, Wilson K, Homan K and Emelianov S (2014). "Indocyanine Green-Loaded Photoacoustic Nanodroplets: Dual Contrast Nanoconstructs for Enhanced Photoacoustic and Ultrasound Imaging." ACS Nano 8(1): 250–259. [PubMed: 24303934]

103. Kanazaki K, Sano K, Makino A, Homma T, Ono M and Saji H (2016). "Polyoxazoline multivalently conjugated with indocyanine green for sensitive in vivo photoacoustic imaging of tumors." Sci. Rep. 6.

104. McDonald MA, Jankovic L, Shahzad K, Burcher M and Li KCP (2009). "Acoustic fingerprints of dye-labeled protein submicrosphere photoacoustic contrast agents." J. Biomed. Opt. 14(3).

105. Lin WH, Li Y, Zhang W, Liu S, Xie ZG and Jing XB (2016). "Near-Infrared Polymeric Nanoparticles with High Content of Cyanine for Bimodal Imaging and Photothermal Therapy." ACS Appl. Mater. Interfaces 8(37): 24426–24432. [PubMed: 27504738]

106. An HW, Qiao SL, Hou CY, Lin YX, Li LL, Xie HY, Wang Y, Wang L and Wang H (2015). "Self-assembled NIR nanovesicles for long-term photoacoustic imaging in vivo." Chem. Comm. 51(70): 13488–13491. [PubMed: 26214147]

107. Scarfe L, Rak-Raszewska A, Geraci S, Darssan D, Sharkey J, Huang JG, Burton NC, Mason D, Ranjzad P, Kenny S, Gretz N, Levy R, Park BK, Garcia-Finana M, Woolf AS, Murray P and Wilm B (2015). "Measures of kidney function by minimally invasive techniques correlate with

histological glomerular damage in SCID mice with adriamycin-induced nephropathy." Sci. Rep. 5.

108. Shi SY, Liu YJ, Chen Y, Zhang ZH, Ding YS, Wu ZQ, Yin J and Nie LM (2016). "Versatile pH-response Micelles with High Cell-Penetrating Helical Diblock Copolymers for Photoacoustic Imaging Guided Synergistic Chemo-Photothermal Therapy." Theranostics 6(12): 2170–2182. [PubMed: 27924155]

109. Biffi S, Petrizza L, Garrovo C, Rampazzo E, Andolfi L, Giustetto P, Nikolov I, Kurdi G, Danailov MB, Zauli G, Secchiero P and Prodi L (2016). "Multimodal near-infrared-emitting PluS Silica nanoparticles with fluorescent, photoacoustic, and photothermal capabilities." Int. J. Nanomed. 11: 4865–4874.

110. Wang JP, Guo F, Yu M, Liu L, Tan FP, Yan R and Li N (2016). "Rapamycin/DiR loaded lipid-polyaniline nanoparticles for dual-modal imaging guided enhanced photothermal and antiangiogenic combination therapy." J. Control. Release 237: 23–34. [PubMed: 27388755]

111. Mishra A, Jiang YY, Roberts S, Ntziachristos V and Westmeyer GG (2016). "Near-Infrared Photoacoustic Imaging Probe Responsive to Calcium." Anal. Chem. 88(22): 10785–10789. [PubMed: 27779396]

112. Funabiki K, Yagi K, Ueta M, Nakajima M, Horiuchi M, Kubota Y and Mastui M (2016). "Rational Molecular Design and Synthesis of Highly Thermo- and Photostable Near-Infrared-Absorbing Heptamethine Cyanine Dyes with the Use of Fluorine Atoms." Chem. Eur. J. 22(35): 12282–12285. [PubMed: 27355196]

113. Chen X, Peng X, Cui A, Wang B, Wang L and Zhang R (2006). "Photostabilities of novel heptamethine 3H-indolenine cyanine dyes with different N-substituents." J. Photochem. Photobio. A: Chem. 181(1): 79–85.

114. Song F, Peng X, Lu E, Zhang R, Chen X and Song B (2004). "Syntheses, spectral properties and photostabilities of novel water-soluble near-infrared cyanine dyes." J. Photochem. Photobio. A: Chem. 168(1): 53–57.

115. Zhang YB, Autry SA, McNamara LE, Nguyen ST, Le N, Brogdon P, Watkins DL, Hammer NI and Delcamp JH (2017). "Near-Infrared Fluorescent Thienothiadiazole Dyes with Large Stokes Shifts and High Photostability." J. Org. Chem. 82(11): 5597–5606. [PubMed: 28474519]

116. Wu X and Zhu W (2015). "Stability enhancement of fluorophores for lighting up practical application in bioimaging." Chem. Soc. Rev. 44(13): 4179–4184. [PubMed: 25175934]

117. Rurack K and Spieles M (2011). "Fluorescence Quantum Yields of a Series of Red and Near-Infrared Dyes Emitting at 600–1000 nm." Anal. Chem. 83(4): 1232–1242. [PubMed: 21250654]

118. Würth C, Grabolle M, Pauli J, Spieles M and Resch-Genger U (2011). "Comparison of Methods and Achievable Uncertainties for the Relative and Absolute Measurement of Photoluminescence Quantum Yields." Anal. Chem. 83(9): 3431–3439. [PubMed: 21473570]

119. Magde D, Wong R and Seybold PG (2002). "Fluorescence Quantum Yields and Their Relation to Lifetimes of Rhodamine 6G and Fluorescein in Nine Solvents: Improved Absolute Standards for Quantum Yields¶." Photochem. Photobiol. 75(4): 327–334. [PubMed: 12003120]

120. Boguta A and Wrobel D (2001). "Fluorescein and phenolphthalein - Correlation of fluorescence and photoelectric properties." J. Fluoresc. 11(2): 129–137.

121. Song W, Wei Q, Liu T, Kuai D, Burke JM, Jiao SL and Zhang HF (2012). "Integrating photoacoustic ophthalmoscopy with scanning laser ophthalmoscopy, optical coherence tomography, and fluorescein angiography for a multimodal retinal imaging platform." J. Biomed. Opt. 17(6).

122. Maeda A, Bu J, Chen J, Zheng G and DaCosta RS (2015). "Dual in vivo Photoacoustic and Fluorescence Imaging of HER2 Expression in Breast Tumors for Diagnosis, Margin Assessment, and Surgical Guidance." Mol. Imaging 14(1): 7290.2014.00043.

123. Field RS, Leyden DE and Murthy RSS (1986). "Quantitative Photoacoustic Spectrometry - Determination of Copper(II) and Iron(III) Complexed on Modified Silica-Gel Samples." Anal. Chim. Acta 186: 123–130.

124. Wurth C, Gonzalez MG, Niessner R, Panne U, Haisch C and Genger UR (2012). "Determination of the absolute fluorescence quantum yield of rhodamine 6G with optical and photoacoustic

methods - Providing the basis for fluorescence quantum yield standards." Talanta 90: 30–37. [PubMed: 22340112]

125. Zhang XF, Zhang YK and Liu LM (2014). "Fluorescence lifetimes and quantum yields of ten rhodamine derivatives: Structural effect on emission mechanism in different solvents." J. Lumin. 145: 448–453.

126. Rossetto N, Fortunati I, Gellini C, Feis A and Ferrante C (2016). "An optofluidic light detector based on the photoacoustic effect." Sens. Actuators B Chem. 233: 71–75.

127. Kubin RF and Fletcher AN (1982). "Fluorescence Quantum Yields of Some Rhodamine Dyes." J. Lumin. 27(4): 455–462.

128. Vilca-Quispe L, Alvarado-Gil JJ, Quintana P and Ordonez-Miranda J (2010). "Diffusion of Methylene Blue in Phantoms of Agar Using a Photoacoustic Technique." Int. J. Thermophys. 31(4–5): 987–997.

129. Song KH, Stein EW, Margenthaler JA and Wang LV (2008). "Noninvasive photoacoustic identification of sentinel lymph nodes containing methylene blue in vivo in a rat model." J. Biomed. Opt. 13(5).

130. Morgounova E, Shao Q, Hackel BJ, Thomas DD and Ashkenazi S (2013). "Photoacoustic lifetime contrast between methylene blue monomers and self-quenched dimers as a model for dual-labeled activatable probes." J. Biomed. Opt. 18(5).

131. Ashkenazi S (2010). "Photoacoustic lifetime imaging of dissolved oxygen using methylene blue." J. Biomed. Opt. 15(4).

132. Jeon M, Song WT, Huynh E, Kim J, Kim J, Helfield BL, Leung BYC, Goertz DE, Zheng G, Oh J, Lovell JF and Kim C (2014). "Methylene blue microbubbles as a model dual-modality contrast agent for ultrasound and activatable photoacoustic imaging." J. Biomed. Opt. 19(1).

133. Phan TTV, Bharathiraja S, Nguyen VT, Moorthy MS, Manivasagan P, Lee KD and Oh J (2017). "Polypyrrole-methylene blue nanoparticles as a single multifunctional nanoplatform for near-infrared photo-induced therapy and photoacoustic imaging." RSC Adv. 7(56): 35027–35037.

134. Wang JX, Lin CY, Moore C, Jhunjhunwala A and Jokerst JV (2018). "Switchable Photoacoustic Intensity of Methylene Blue via Sodium Dodecyl Sulfate Micellization." Langmuir 34(1): 359–365. [PubMed: 29232146]

135. Umezawa K, Citterio D and Suzuki K (2014). "New Trends in Near-Infrared Fluorophores for Bioimaging." Anal. Sci. 30(3): 327–349. [PubMed: 24614728]

136. Umezawa K, Citterio D and Suzuki K (2007). "Squaraine-based near-infrared dye with bright fluorescence and solvatochromic property." Chem. Lett. 36(12): 1424–1425.

137. Umezawa K, Cittierio D and Suzuki K (2008). "Water-soluble NIR fluorescent probes based on squaraine and their application for protein Labeling." Anal. Sci. 24(2): 213–217. [PubMed: 18270411]

138. An F-F, Deng Z-J, Ye J, Zhang J-F, Yang Y-L, Li C-H, Zheng C-J and Zhang X-H (2014). "Aggregation-Induced Near-Infrared Absorption of Squaraine Dye in an Albumin Nanocomplex for Photoacoustic Tomography in Vivo." ACS Appl. Mater. Interfaces 6(20): 17985–17992. [PubMed: 25223319]

139. Arunkumar E, Forbes CC, Noll BC and Smith BD (2005). "Squaraine-derived rotaxanes: Sterically protected fluorescent near-IR dyes." J. Am. Chem. Soc. 127(10): 3288–3289. [PubMed: 15755140]

140. Ho CJH, Balasundaram G, Driessen W, McLaren R, Wong CL, Dinish US, Attia ABE, Ntziachristos V and Olivo M (2014). "Multifunctional Photosensitizer-Based Contrast Agents for Photoacoustic Imaging." Sci. Rep. 4.

141. Zhang D, Qiao Z-Y, Mayerhoeffer U, Spenst P, Li X-J, Wuerthner F and Wang H (2014). "Nano-Confined Squaraine Dye Assemblies: New Photoacoustic and Near-Infrared Fluorescence Dual-Modular Imaging Probes in Vivo." Bioconjugate Chem. 25(11): 2021–2029.

142. Sreejith S, Joseph J, Lin MJ, Menon NV, Borah P, Ng HJ, Loong YX, Kang Y, Yu SWK and Zhao YL (2015). "Near-Infrared Squaraine Dye Encapsulated Micelles for in Vivo Fluorescence and Photoacoustic Bimodal Imaging." ACS Nano 9(6): 5695–5704. [PubMed: 26022724]

143. Duan ZY, Gao YJ, Qiao ZY, Fan G, Liu Y, Zhang D and Wang H (2014). "A photoacoustic approach for monitoring the drug release of pH-sensitive poly(beta-amino ester)s." J. Mater. Chem. B 2(37): 6271–6282.

144. Anees P, Joseph J, Sreejith S, Menon NV, Kang YJ, Yu SWK, Ajayaghosh A and Zhao YL (2016). "Real time monitoring of aminothiol level in blood using a near-infrared dye assisted deep tissue fluorescence and photoacoustic bimodal imaging." Chem. Sci. 7(7): 4110–4116. [PubMed: 30155054]

145. Qiao ZY, Zhao WJ, Cong Y, Zhang D, Hu ZY, Duan ZY and Wang H (2016). "Self-Assembled ROS-Sensitive Polymer-Peptide Therapeutics Incorporating Built-in Reporters for Evaluation of Treatment Efficacy." Biomacromolecules 17(5): 1643–1652. [PubMed: 27023216]

146. Lynch DE and Hamilton DG (2017). "Croconaine Dyes - the Lesser Known Siblings of Squaraines." Eur. J. Org. Chem.(27): 3897–3911.

147. Spence GT, Hartland GV and Smith BD (2013). "Activated photothermal heating using croconaine dyes." Chem. Sci. 4(11): 4240–4244.

148. Spence GT, Lo SS, Ke CF, Destecroix H, Davis AP, Hartland GV and Smith BD (2014). "Near-Infrared Croconaine Rotaxanes and Doped Nanoparticles for Enhanced Aqueous Photothermal Heating." Chem. Eur. J. 20(39): 12628–12635. [PubMed: 25146580]

149. Guha S, Shaw GK, Mitcham TM, Bouchard RR and Smith BD (2016). "Croconaine rotaxane for acid activated photothermal heating and ratiometric photoacoustic imaging of acidic pH." Chem. Comm. 52(1): 120–123. [PubMed: 26502996]

150. Harmatys KM, Battles PM, Peck EM, Spence GT, Roland FM and Smith BD (2017). "Selective photothermal inactivation of cells labeled with near-infrared croconaine dye." Chem. Comm. 53(71): 9906–9909. [PubMed: 28828431]

151. Tang LG, Zhang FW, Yu F, Sun WJ, Song ML, Chen XY, Zhang XZ and Sun XL (2017). "Croconaine nanoparticles with enhanced tumor accumulation for multimodality cancer theranostics." Biomaterials 129: 28–36. [PubMed: 28324863]

152. Futterer H, Vongoldammer E, Heihoff K and Pelzl J (1981). "Photoacoustic Spectroscopy on some Porphyrins." Biophysics of Structure and Mechanism 7(4): 256–256.

153. Voigtman E, Jurgensen A and Winefordner J (1981). "Condensed Phase Photoacoustic Spectroscopic Detection of Porphyrins and Dyes." Anal. Chem. 53(9): 1442–1446.

154. Moore TA, Benin D and Tom R (1983). "Photoacoustic Measurement of Photophysical Properties of Photosynthetic Pigments - Porphyrins and Chlorophylls." Journal De Physique 44(NC-6): 351–353.

155. Ferreira JA, Barral R, Baptista JD and Ferreira MIC (1991). "Absorption-Coefficients and Fluorescence Quantum Yields of Porphyrin Films Determiend by Optical and Photoacoustic Spectroscopies." J. Lumin. 48–9: 385–390.

156. Feitelson J and Mauzerall DC (1993). "Wide-Band, Time-Resolved Photoacoustic Study of Electron-Transfer Reactions - Photoexcited Magnesium Porphyrin and Quinones." J. Phys. Chem. 97(32): 8410–8413.

157. Feitelson J and Mauzerall D (1996). "Photoacoustic evaluation of volume and entropy changes in energy and electron transfer. Triplet state porphyrin with oxygen and naphthoquinone-2-sulfonate." J. Phys. Chem. 100(18): 7698–7703.

158. Gensch T and Braslavsky SE (1997). "Volume changes related to triplet formation of water-soluble porphyrins. A laser-induced optoacoustic spectroscopy (LIOAS) study (vol 101, pg 101, 1997)." J. Phys. Chem. B 101(15): 3012–3012.

159. Pineiro M, Carvalho AL, Pereira MM, Gonsalves A, Arnaut LG and Formosinho SJ (1998). "Photoacoustic measurements of porphyrin triplet-state quantum yields and singlet-oxygen efficiencies." Chem. Eur. J. 4(11): 2299–2307.

160. Liu W, Shi TS, An QD and Yang DZ (2001). "Synthesis of tetra (4-n-decanoyloxyphenyl)porphyrin complexes and Fourier transform infrared photoacoustic spectra." Chemical Journal of Chinese Universities-Chinese 22(1): 16–20.

161. Hanyz I and Wrobel D (2002). "The influence of pH on charged porphyrins studied by fluorescence and photoacoustic spectroscopy." Photochem. Photobiol. Sci. 1(2): 126–132. [PubMed: 12659128]

162. Bartczak A, Namiki Y, Qian DJ, Miyake J, Boguta A, Goc J, Lukasiewicz J and Frackowiak D (2003). "The interactions between tetrapyridyl porphyrin and viologen units covalently linked to polymers." J. Photochem. Photobio. A: Chem. 159(3): 259–272.

163. Wrobel D and Graja A (2006). "Modification of electronic structure in supramolecular fullerene-porphyrin systems studied by fluorescence, photoacoustic and photothermal spectroscopy." J. Photochem. Photobio. A: Chem. 183(1–2): 79–88.

164. Skrzypek D, Madejska I, Habdas J and Dudkowiak A (2008). "The spectroscopic characterisation of proline derivatives of tolyl-porphyrins and their iron and cobalt complexes." J. Mol. Struct. 876(1–3): 177–185.

165. Kruk MM and Braslavsky SE (2012). "Structural volume changes upon triplet formation of water-soluble porphyrins depend on the resonant effect of the substituents." Photochem. Photobiol. Sci. 11(6): 972–978. [PubMed: 22286746]

166. Stolik S, Tomas SA, Ramon-Gallegos E and Sanchez F (2002). "Kinetic study of delta-Ala induced porphyrins in mice using photoacoustic and fluorescence spectroscopies." J. Photochem. Photobio. B: Bio. 68(2–3): 117–122.

167. Lovell JF, Jin CS, Huynh E, Jin HL, Kim C, Rubinstein JL, Chan WCW, Cao WG, Wang LV and Zheng G (2011). "Porphysome nanovesicles generated by porphyrin bilayers for use as multimodal biophotonic contrast agents." Nat. Mater. 10(4): 324–332. [PubMed: 21423187]

168. Jin CS, Lovell JF, Chen J and Zheng G (2013). "Ablation of Hypoxic Tumors with Dose-Equivalent Photothermal, but Not Photodynamic, Therapy Using a Nanostructured Porphyrin Assembly." ACS Nano 7(3): 2541–2550. [PubMed: 23394589]

169. Ng KK, Shakiba M, Huynh E, Weersink RA, Roxin A, Wilson BC and Zheng G (2014). "Stimuli-Responsive Photoacoustic Nanoswitch for in Vivo Sensing Applications." ACS Nano 8(8): 8363–8373. [PubMed: 25046406]

170. Huynh E, Jin CS, Wilson BC and Zheng G (2014). "Aggregate Enhanced Trimodal Porphyrin Shell Microbubbles for Ultrasound, Photoacoustic, and Fluorescence Imaging." Bioconjugate Chem. 25(4): 796–801.

171. Paproski RJ, Forbrich A, Huynh E, Chen J, Lewis JD, Zheng G and Zemp RJ (2016). "Porphyrin Nanodroplets: Sub-micrometer Ultrasound and Photoacoustic Contrast Imaging Agents." Small 12(3): 371–380. [PubMed: 26633744]

172. Jian J, Liu CB, Gong YP, Su L, Zhang B, Wang ZG, Wang D, Zhou Y, Xu FF, Li P, Zheng YY, Song L and Zhou XY (2014). "India Ink Incorporated Multifunctional Phase-transition Nanodroplets for Photoacoustic/Ultrasound Dual-modality Imaging and Photoacoustic Effect Based Tumor Therapy." Theranostics 4(10): 1026–1038. [PubMed: 25161702]

173. Zhang YM, Wang DP, Goel S, Sun BY, Chitgupi U, Geng JM, Sun HY, Barnhart TE, Cai WB, Xia J and Lovell JF (2016). "Surfactant-Stripped Frozen Pheophytin Micelles for Multimodal Gut Imaging." Adv. Mater. 28(38): 8524–8530. [PubMed: 27396479]

174. Zhang YM, Jeon M, Rich LJ, Hong H, Geng JM, Zhang Y, Shi SX, Barnhart TE, Alexandridis P, Huizinga JD, Seshadri M, Cai WB, Kim C and Lovell JF (2014). "Non-invasive multimodal functional imaging of the intestine with frozen micellar naphthalocyanines." Nat. Nanotechnol. 9(8): 631–638. [PubMed: 24997526]

175. Abuteen A, Zanganeh S, Akhigbe J, Samankumara LP, Aguirre A, Biswal N, Braune M, Vollertsen A, Roeder B, Brueckner C and Zhu Q (2013). "The evaluation of NIR-absorbing porphyrin derivatives as contrast agents in photoacoustic imaging." Phys. Chem. Chem. Phys. 15(42): 18502–18509. [PubMed: 24071709]

176. Banala S, Fokong S, Brand C, Andreou C, Krautler B, Rueping M and Kiessling F (2017). "Quinone-fused porphyrins as contrast agents for photoacoustic imaging." Chem. Sci. 8(9): 6176–6181. [PubMed: 28989649]

177. Gujrati V, Mishra A and Ntziachristos V (2017). "Molecular imaging probes for multi-spectral optoacoustic tomography." Chem. Comm. 53(34): 4653–4672. [PubMed: 28387781]

178. Luciano M and Bruckner C (2017). "Modifications of Porphyrins and Hydroporphyrins for Their Solubilization in Aqueous Media." Molecules 22(6).

179. Luciano M, Erfanzadeh M, Zhou FF, Zhu H, Bornhutter T, Roder B, Zhu Q and Bruckner C (2017). "In vivo photoacoustic tumor tomography using a quinoline-annulated porphyrin as NIR molecular contrast agent." Org. Biomol. Chem. 15(4): 972–983. [PubMed: 28059409]

180. Lee C, Kim J, Zhang YM, Jeon M, Liu CB, Song L, Lovell JF and Kim C (2015). "Dual-color photoacoustic lymph node imaging using nanoformulated naphthalocyanines." Biomaterials 73: 142–148. [PubMed: 26408999]

181. Zhou Y, Wang DP, Zhang YM, Chitgupi U, Geng JM, Wang YH, Zhang YZ, Cook TR, Xia J and Lovell JF (2016). "A Phosphorus Phthalocyanine Formulation with Intense Absorbance at 1000 nm for Deep Optical Imaging." Theranostics 6(5): 688–697. [PubMed: 27022416]

182. Furuyama T, Satoh K, Kushiya T and Kobayashi N (2014). "Design, Synthesis, and Properties of Phthalocyanine Complexes with Main-Group Elements Showing Main Absorption and Fluorescence beyond 1000 nm." J. Am. Chem. Soc. 136(2): 765–776. [PubMed: 24328229]

183. Mauriello-Jimenez C, Henry M, Aggad D, Raehm L, Cattoen X, Man MWC, Charnay C, Alpugan S, Ahsen V, Tarakci DK, Maillard P, Maynadier M, Garcia M, Dumoulin F, Gary-Bobo M, Coll JL, Josserand V and Durand JO (2017). "Porphyrin- or phthalocyanine-bridged silsesquioxane nanoparticles for two-photon photodynamic therapy or photoacoustic imaging." Nanoscale 9(43): 16622–16626. [PubMed: 29082396]

184. Li LL, Wang D, Wang L, Ramella D, Wang H, Gao H, Zhang JJ, Xing Y, Li BN, Yang Z, Cao H and He WL (2018). "The photoacoustic effect of near-infrared absorbing porphyrin derivatives prepared via click chemistry." Dyes Pigm. 148: 501–507.

185. Li H, Zhang P, Smaga LP, Hoffman RA and Chan J (2015). "Photoacoustic Probes for Ratiometric Imaging of Copper(II)." J. Am. Chem. Soc. 137(50): 15628–15631. [PubMed: 26652006]

186. Ni Y, Kannadorai RK, Peng JJ, Yu SWK, Chang YT and Wu JS (2016). "Naphthalene-fused BODIPY near-infrared dye as a stable contrast agent for in vivo photoacoustic imaging." Chem. Comm. 52(77): 11504–11507. [PubMed: 27709191]

187. Ni Y, Kannadorai RK, Yu SWK, Chang YT and Wu JS (2017). "Push-pull type meso-ester substituted BODIPY near-infrared dyes as contrast agents for photoacoustic imaging." Org. Biomol. Chem. 15(21): 4531–4535. [PubMed: 28513725]

188. Hu WB, Ma HH, Hou B, Zhao H, Ji Y, Jiang RC, Hu XM, Lu XM, Zhang L, Tang YF, Fan QL and Huang W (2016). "Engineering Lysosome-Targeting BODIPY Nanoparticles for Photoacoustic Imaging and Photodynamic Therapy under Near-Infrared Light." ACS Appl. Mater. Interfaces 8(19): 12039–12047. [PubMed: 27123534]

189. Gawale Y, Adarsh N, Kalva SK, Joseph J, Pramanik M, Ramaiah D and Sekar N (2017). "Carbazole-Linked Near-Infrared Aza-BODIPY Dyes as Triplet Sensitizers and Photoacoustic Contrast Agents for Deep-Tissue Imaging." Chem. Eur. J. 23(27): 6570–6578. [PubMed: 28226192]

190. Tang Q, Si W, Huang C, Ding K, Huang W, Chen P, Zhang Q and Dong X (2017). "An aza-BODIPY photosensitizer for photoacoustic and photothermal imaging guided dual modal cancer phototherapy." J. Mater. Chem. B 5(8): 1566–1573.

191. Miki K, Enomoto A, Inoue T, Nabeshima T, Saino S, Shimizu S, Matsuoka H and Ohe K (2017). "Polymeric Self-Assemblies with Boron-Containing Near-Infrared Dye Dimers for Photoacoustic Imaging Probes." Biomacromolecules 18(1): 249–256. [PubMed: 27936606]

192. Reinhardt CJ, Zhou EY, Jorgensen MD, Partipilo G and Chan J (2018). "A Ratiometric Acoustogenic Probe for in Vivo Imaging of Endogenous Nitric Oxide." J. Am. Chem. Soc. 140(3): 1011–1018. [PubMed: 29313677]

193. Bairwa K, Grover J, Kania M and Jachak SM (2014). "Recent developments in chemistry and biology of curcumin analogues." RSC Adv. 4(27): 13946–13978.

194. Bellinger S, Hatamimoslehabadi M, Bag S, Mithila F, La J, Frenette M, Laoui S, Szalda DJ, Yelleswarapu C and Rochford J (2018). "Photophysical and Photoacoustic Properties of Quadrupolar Borondifluoride Curcuminoid Dyes." Chem. Eur. J. 24(4): 906–917. [PubMed: 29149546]

195. Guberman-Pfeffer MJ, Greco JA, Samankumara LP, Zeller M, Birge RR, Gascon JA and Bruckner C (2017). "Bacteriochlorins with a Twist: Discovery of a Unique Mechanism to Red-

Shift the Optical Spectra of Bacteriochlorins." J. Am. Chem. Soc. 139(1): 548–560. [PubMed: 27997161]

196. Fan Q, Cheng K, Yang Z, Zhang R, Yang M, Hu X, Ma X, Bu L, Lu X, Xiong X, Huang W, Zhao H and Cheng Z (2015). "Perylene-Diimide-Based Nanoparticles as Highly Efficient Photoacoustic Agents for Deep Brain Tumor Imaging in Living Mice." Adv. Mater. 27(5): 843–847. [PubMed: 25376906]

197. Huang S, Upputuri PK, Liu H, Pramanik M and Wang MF (2016). "A dual-functional benzobisthiadiazole derivative as an effective theranostic agent for near-infrared photoacoustic imaging and photothermal therapy." J. Mater. Chem. B 4(9): 1696–1703.

198. Xu A-P, Han H-H, Lu J, Yang P-P, Gao Y-J, An H-W, Zhanng D, Li L-Z, Zhang J-P, Wang D, Wang L and Wang H (2016). "Charge transfer NIR dyes for improved photoacoustic effect." Dyes Pigm. 125: 392–398.

199. Hatamimoslehabadi M, Bellinger S, La J, Ahmad E, Frenette M, Yelleswarapu C and Rochford J (2017). "Correlation of Photophysical Properties with the Photoacoustic Emission for a Selection of Established Chromophores." J. Phys. Chem. C 121(43): 24168–24178.

200. Roberts S, Seeger M, Jiang Y, Mishra A, Sigmund F, Stelzl A, Lauri A, Symvoulidis P, Rolbieski H, Preller M, Deán-Ben XL, Razansky D, Orschmann T, Desbordes SC, Vetschera P, Bach T, Ntziachristos V and Westmeyer GG (2018). "Calcium Sensor for Photoacoustic Imaging." J. Am. Chem. Soc. 140(8): 2718–2721. [PubMed: 28945084]
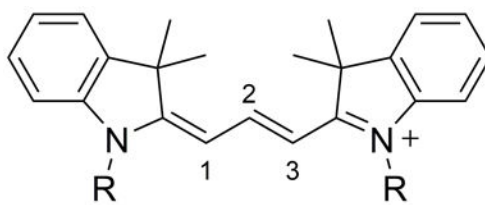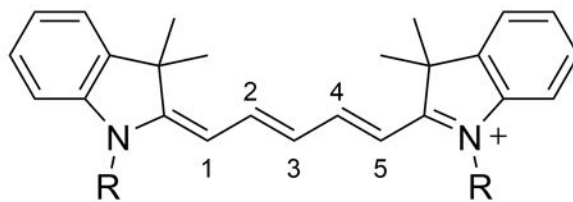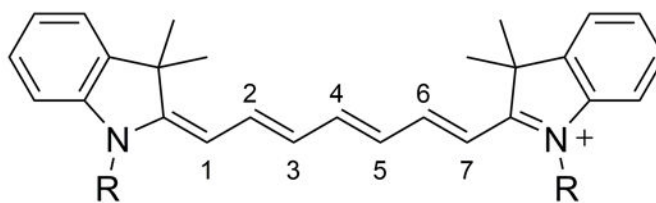
Figure 1.
Molecular structures of the Cy3 (**1**), Cy5 (**2**) and Cy7 (**3**) indocarbocyanine based dyes (65).
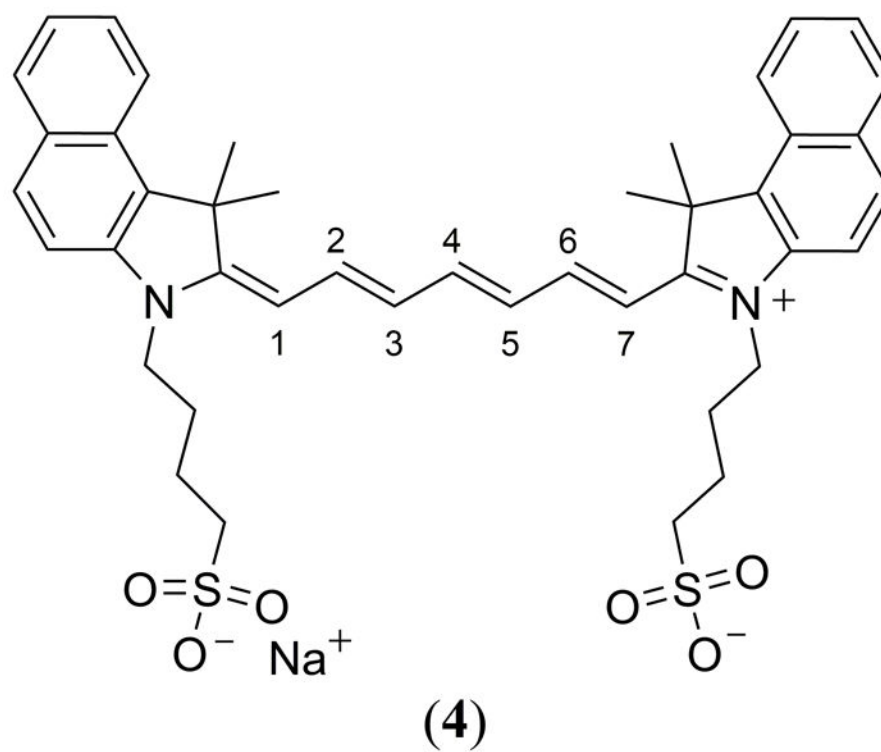
Figure 2.
Molecular structure of the FDA approved indocyanine green (ICG) dye (**4**).
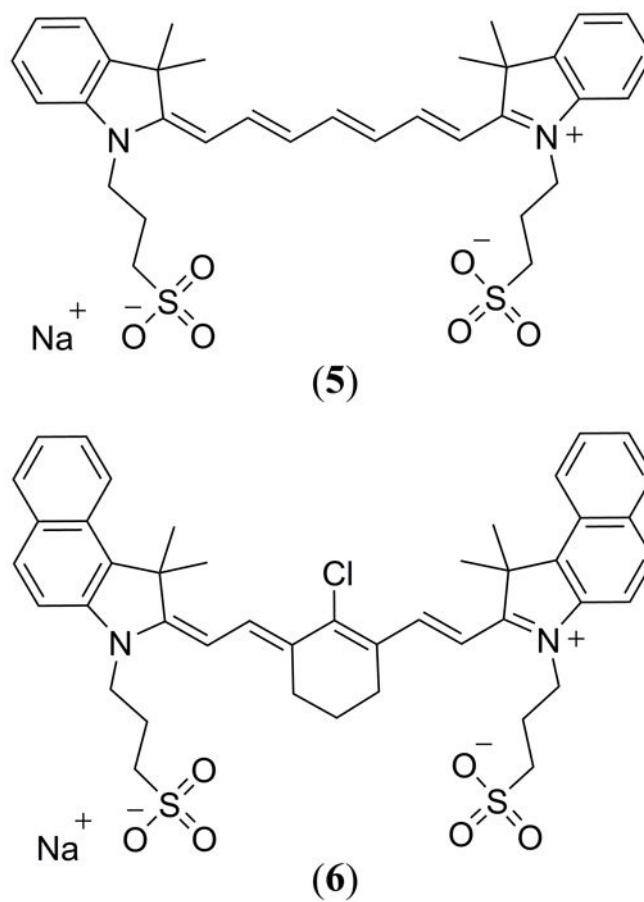
Figure 3.
Structures of the $ADS_{740}WS$ (**5**) and $ADS_{830}WS$ (**6**) cyanine-based dyes reported by Laufer et al. (91).
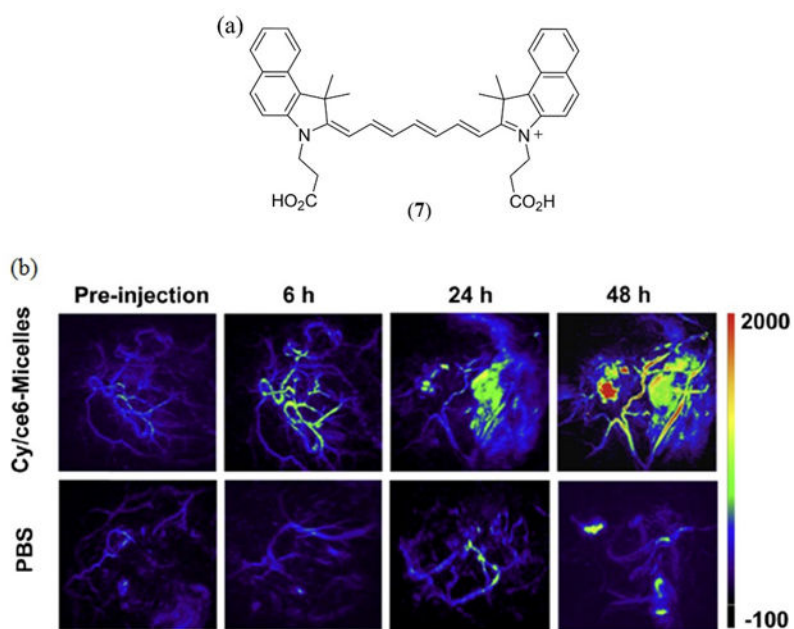
Figure 4.
(a) Molecular structure of the dicarboxy Cy7.5-based cypate cyanine dye (**7**) investigated by Guo et al. (92); (b) In vivo PAI of mice bearing the 4T1 tumor injected with PBS and **7**/Ce6-micelles (7.5 mg/kg dosage) pre-injection and 6, 24, 48 h post-injection. Reproduced with permission from ref. 92. Copyright 2014 Elsevier.
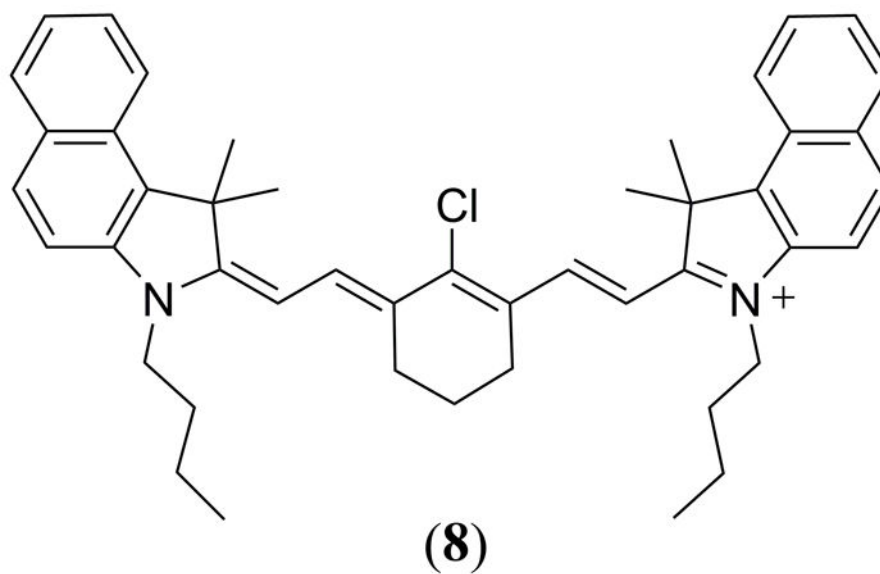
Figure 5.
Structure of the IC7–1-Bu (**8**) molecule reported by Temma et al. (93).
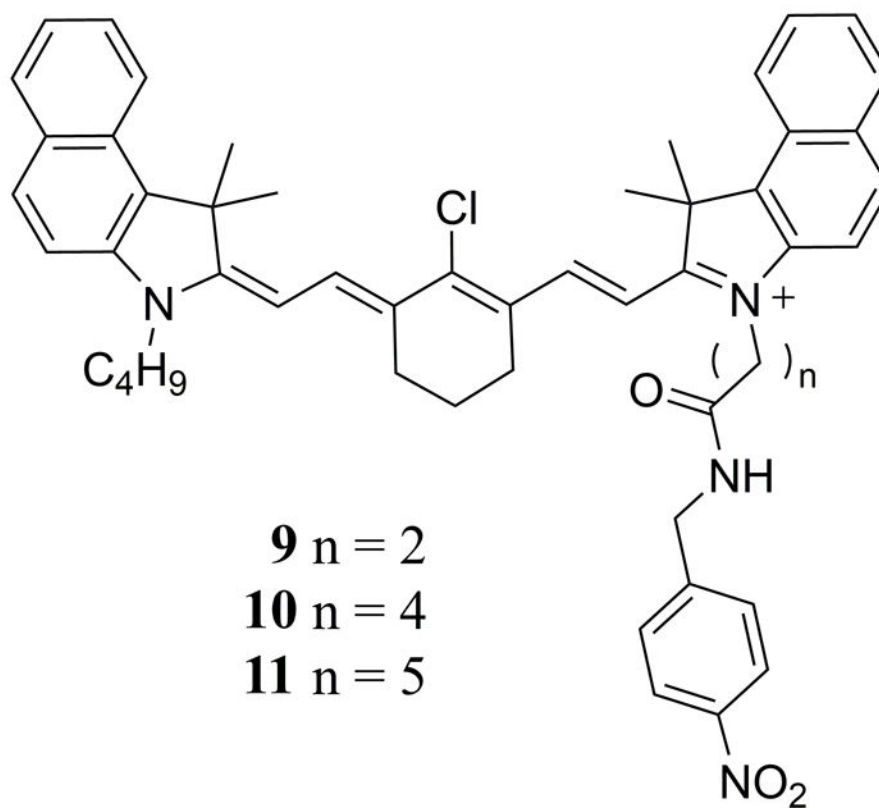
Figure 6.
Molecular structures of the asymmetrical cyanine derivatives **9** - **11** reported by Onoe et al. with enhanced photostability relative to ICG (**4**) and **8** (94).

(12)
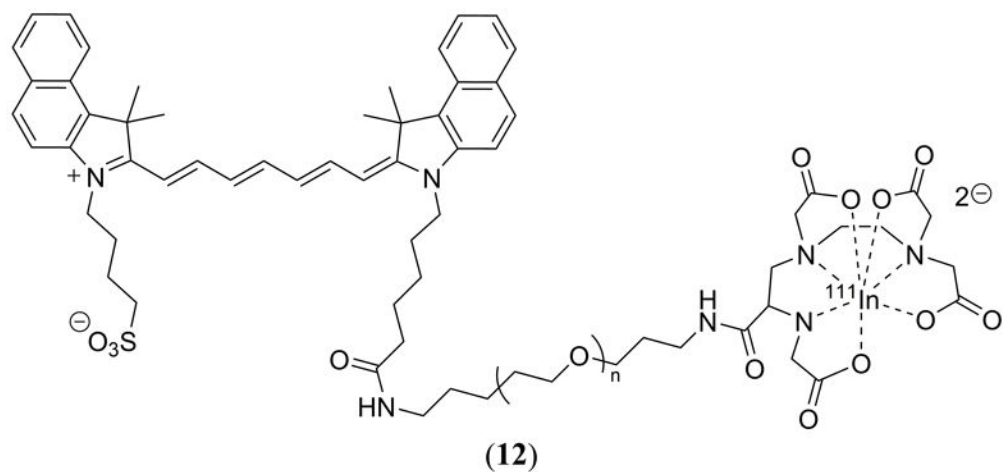
Figure 7.
Molecular structure of the PEG-ylated ICG dye **12** reported by Kanazaki et al. to enhance its permeability and retention for improved in vivo PAI of allografted tumors in mice (98). This specific structure also illustrates the covalent conjugation of a ^{111}In label for single-photon emission computed tomography (SPECT) and PAI (99).
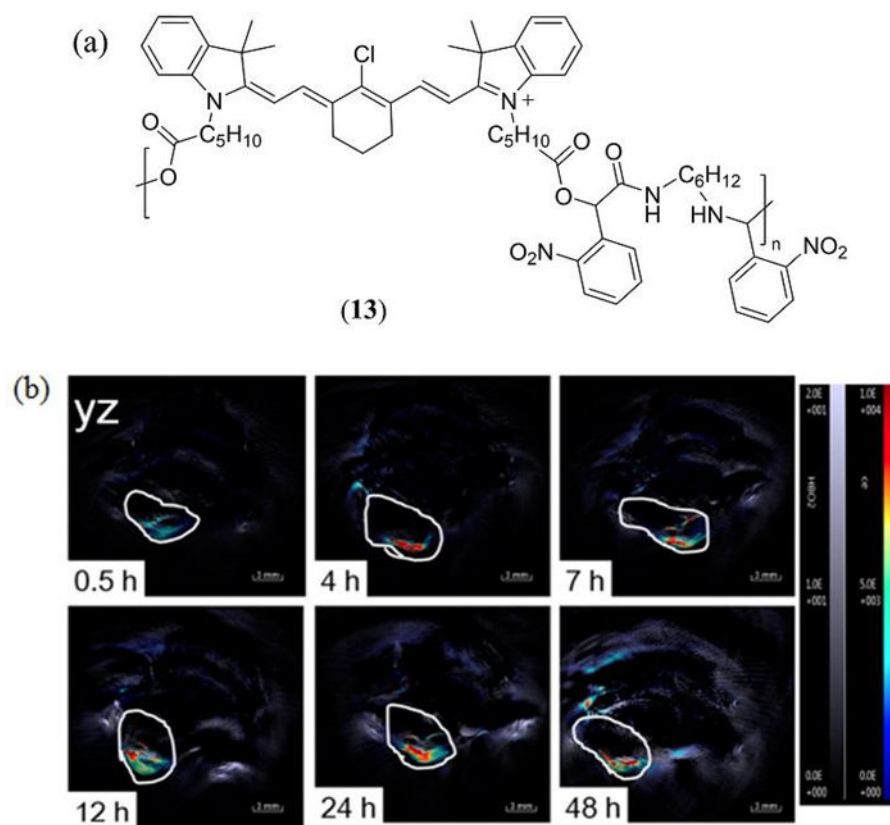
Figure 8.
(a) Molecular structure of the Cy5 containing co-polymer **13** reported by Lin et al. to form poly(ethylene glycol)$_{2k}$-*block*-poly($_{D,L}$-lactide)$_{zk}$ (PEG-PLA) based nanoparticles (105); (b) PAI of a HeLa-tumor-containing mouse administered intratumorally with nanoparticles derived from **13**. Reproduced with permission from ref. 105. Copyright 2016 American Chemical Society.
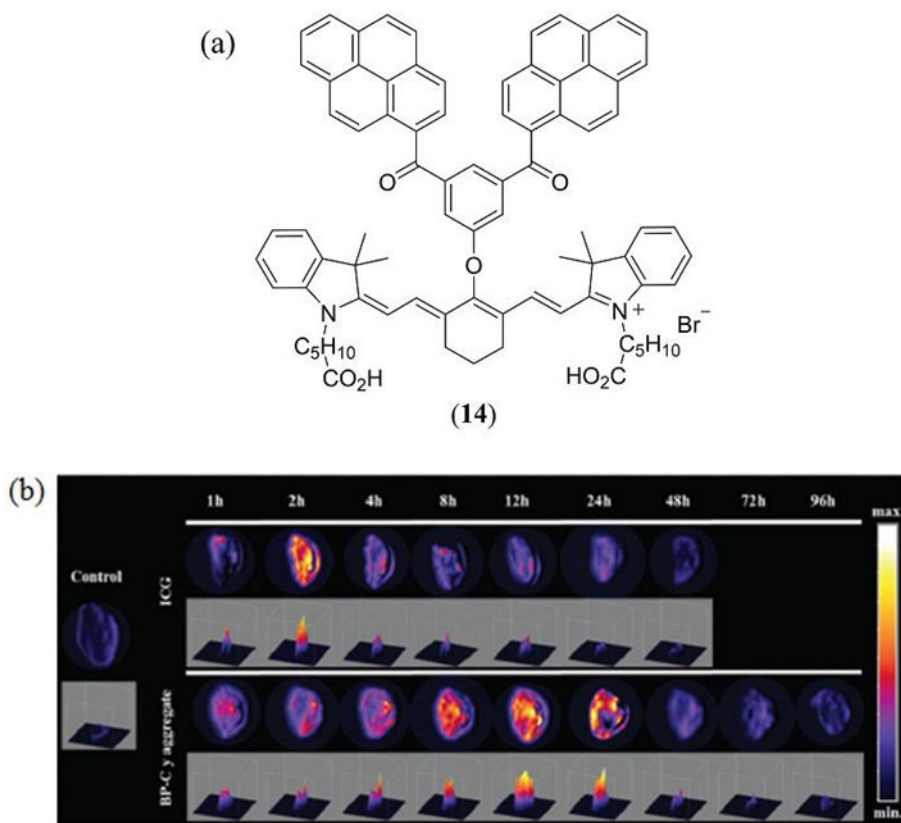
Figure 9.
(a) The supramolecular bis-pyrene cyanine dye **14** reported by An et al. (106); (b) In vivo PAI of tumor-xenografted mice with normalized ICG vs. **14** amplitudes at various time intervals post-injection. Reproduced with permission from ref. 106. Copyright 2015 Royal Society of Chemistry.

(15)

(16)
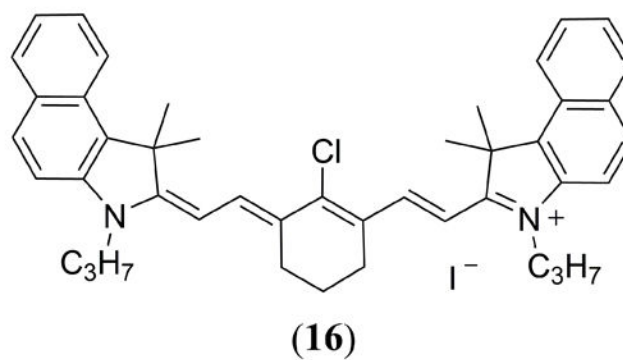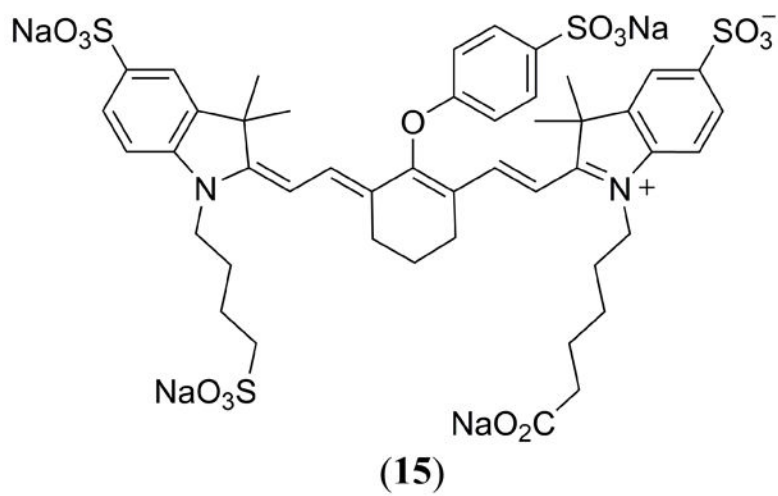
Figure 10.
Molecular structures of the IRDye800CW carboxylate (**15**) and IR-780 (**16**) cyanine dyes.
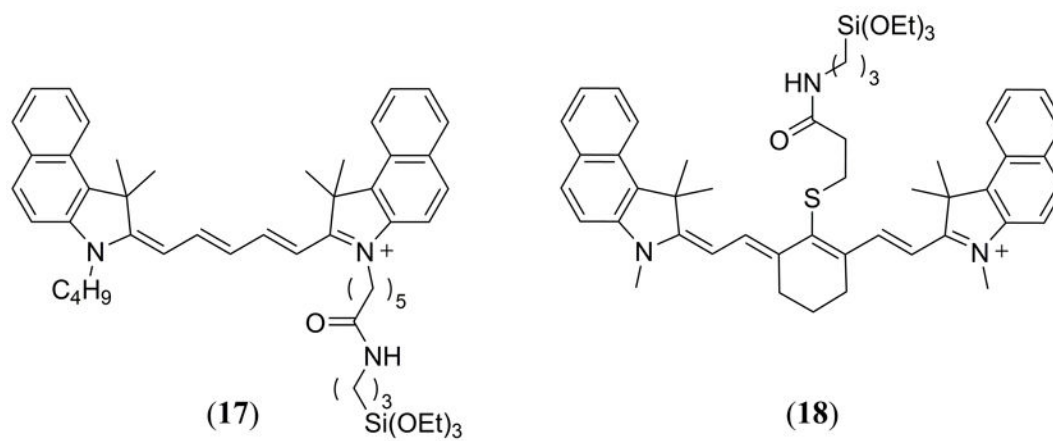
Figure 11.
Molecular structures of the triethoxysilane functionalized Cy5.5 (**17**) and Cy7.5 (**18**) dyes reported by Biffi et al. for covalent assembly of silica-PEG based nanoparticles (109).
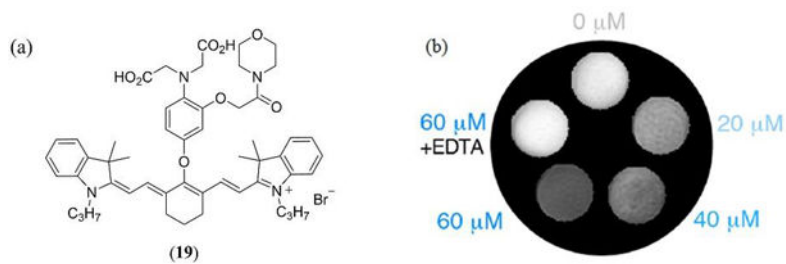
Figure 12.
(a) Structure of the PA responsive Ca^{2+} chemosensor **19** reported by Mishra et al. (111); (b) PA contrast of **19** is illustrated with varying Ca^{2+} concentrations. Irreversibility of Ca^{2+} binding is also illustrated in the presence of EDTA. Reproduced with permission from ref. 111. Copyright 2016 American Chemical Society.

fluorescein (**20**)
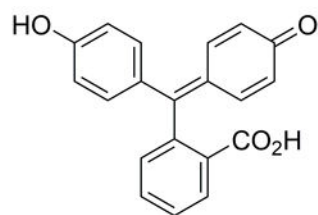
phenolphtalein (**21**)

rhodamine (**22**)
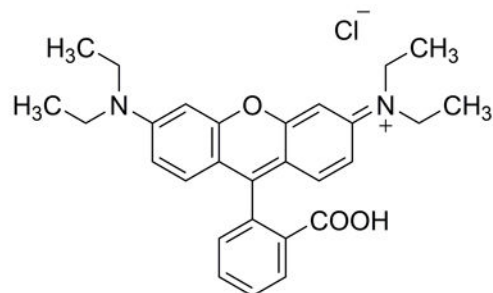
rhodamine B (**23**)
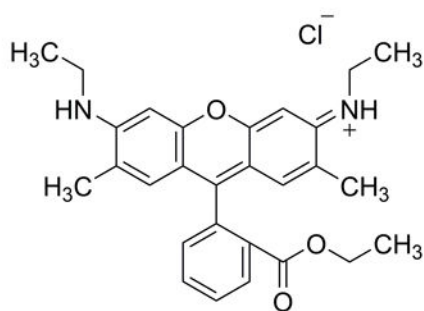
rhodamine 6G (**24**)

Figure 13.
Structures of popular, commercially available fluorescein (**20**), phenolphthalein (**21**) and rhodamine derivatives (**22** – **24**) previously used for PA studies.

Atto680 (**25**)
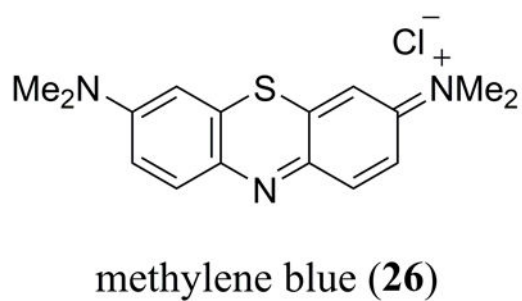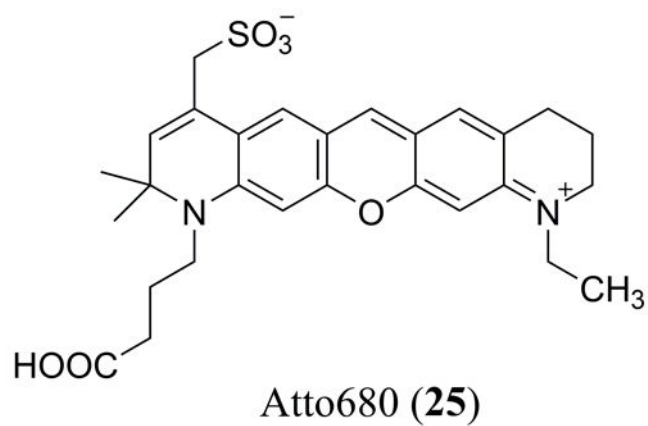
methylene blue (**26**)

Figure 14.
Molecular structure of the commercially available Atto680 dye (**25**) and methylene blue (**26**).
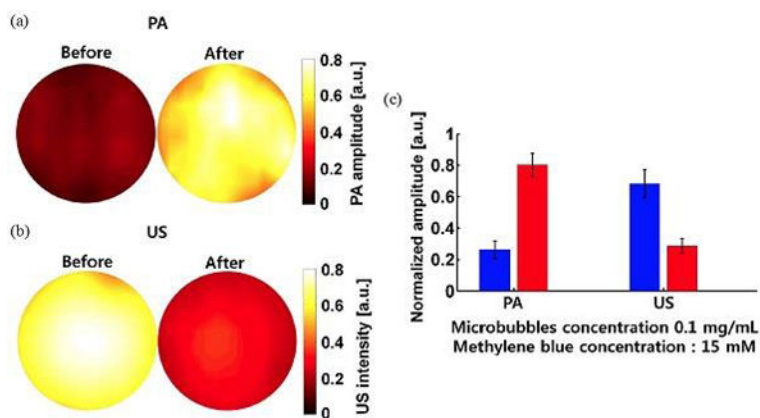
Figure 15.
(a) PA and (b) ultrasound (US) imaging before and after sonication of aqueous, methylene blue (**26**) doped, octafluoropropane microbubbles formed with a DPPC:DPPA:MPEG5000 (10:1:1.2) based lipid (132); (c) PA and US signal amplitude before and after sonication. Reproduced with permission from ref. 132. Copyright 2014 Society of Photographic Instrumentation Engineers.
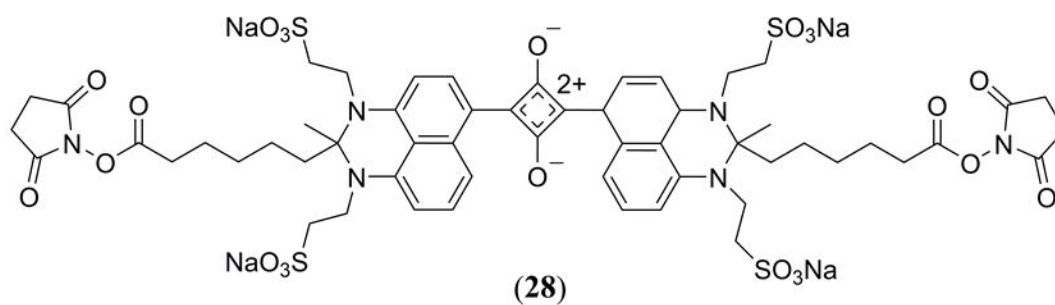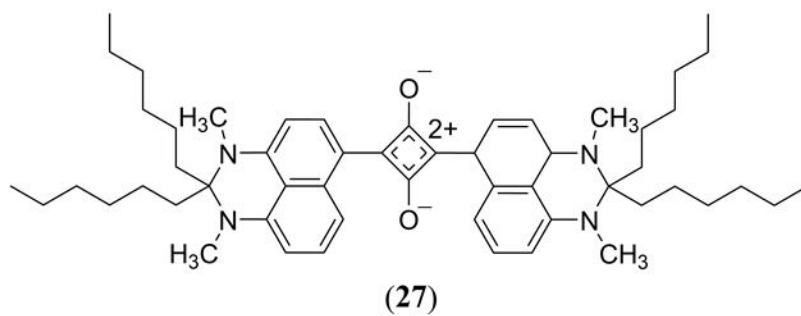
Figure 16.
Structures of the KSQ-2 (**27**) (56) and KSQ-4 (**28**) (57) squaraine dyes reported by
Umezawa and coworkers.
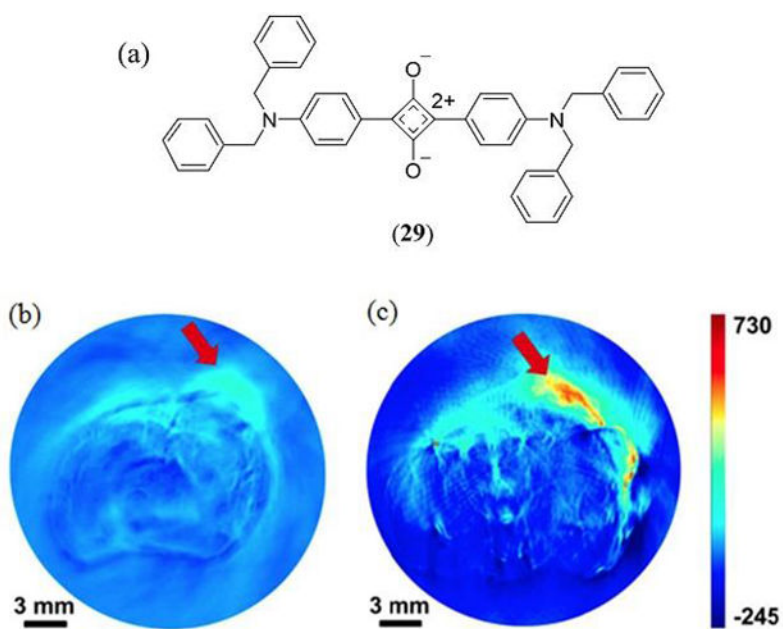
Figure 17.
(a) Molecular structure of the 4-(*N,N'*-dibenzylamino)phenyl substituted squaraine dye (**29**) used for PAI studies by An et al. (138). In vivo PAI of 4T1 tumor bearing mice (b) without and (c) with **29-**albumin nanoparticle administration. Reproduced with permission from ref. 138. Copyright 2014 American Chemical Society.

(30)
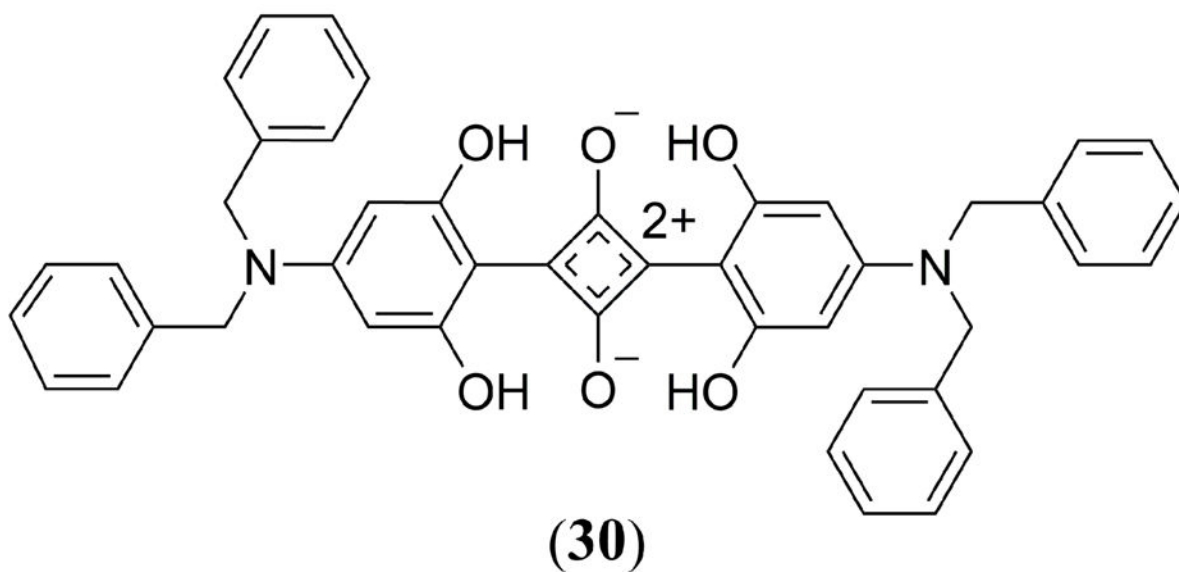
Figure 18.
Structure of the commercially available squaraine derivative, 2,4-Bis[4-(N,N-dibenzylamino)-2,6-dihydroxyphenyl]squaraine **30** investigated by Ho et al. (140).
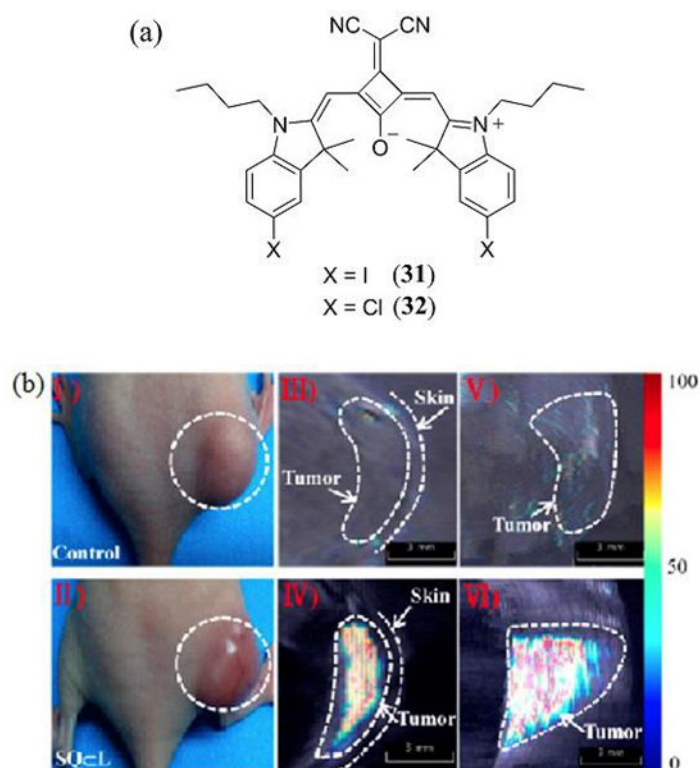
Figure 19.
(a) Molecular structures of the iodo (**31**) and chloro (**32**) substituted bis(*N*-butylindole) squaraine dyes investigated by Zhang et al. and Duan et al., respectively, for PAI (141, 143); (b) PAI of MCF-7 xenografted tumor bearing mice without (I,III, V) and with (II, IV, VI) administration of **31**:liposome. (I) and (II) are representative photos of the tumor bearing mice; (III) and (IV) show one transverse slice in the 3D PA image; (V) and (VI) show aligned images from the different transverse section. Reproduced with permission from ref. 141. Copyright 2014 American Chemical Society.

(33)
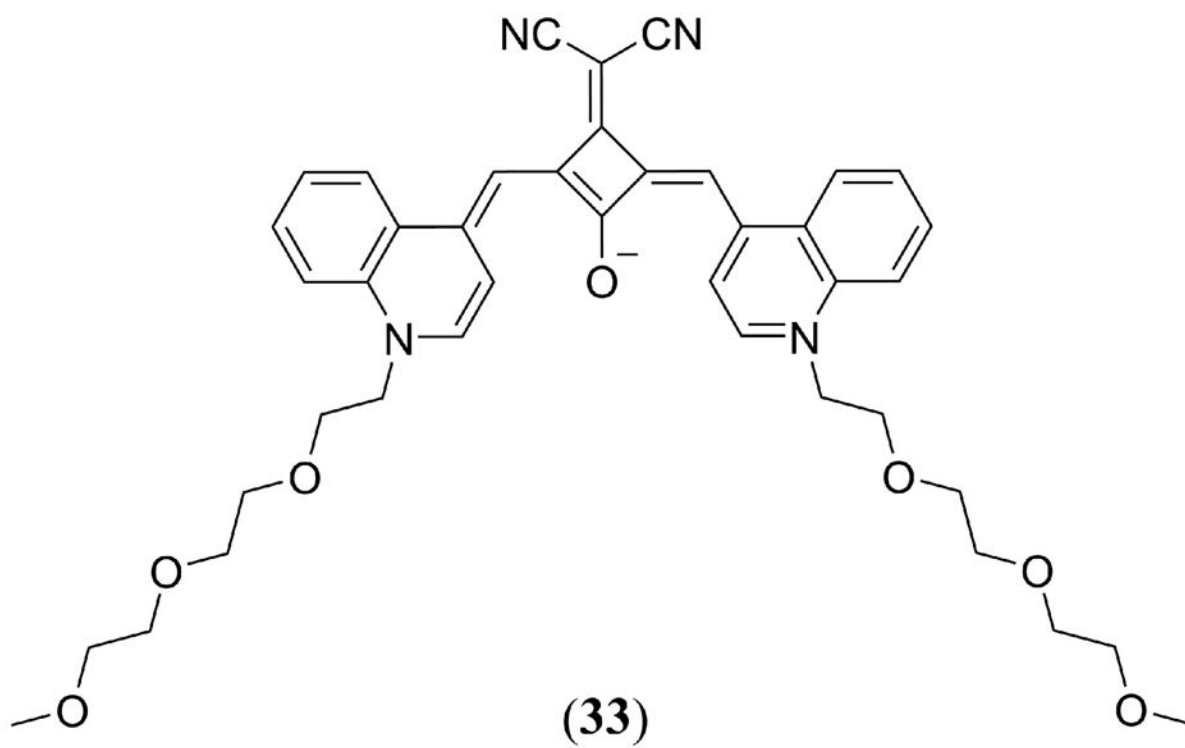
Figure 20.
A PEG-ylated squaraine dye reported by Sreejith et al. (142).
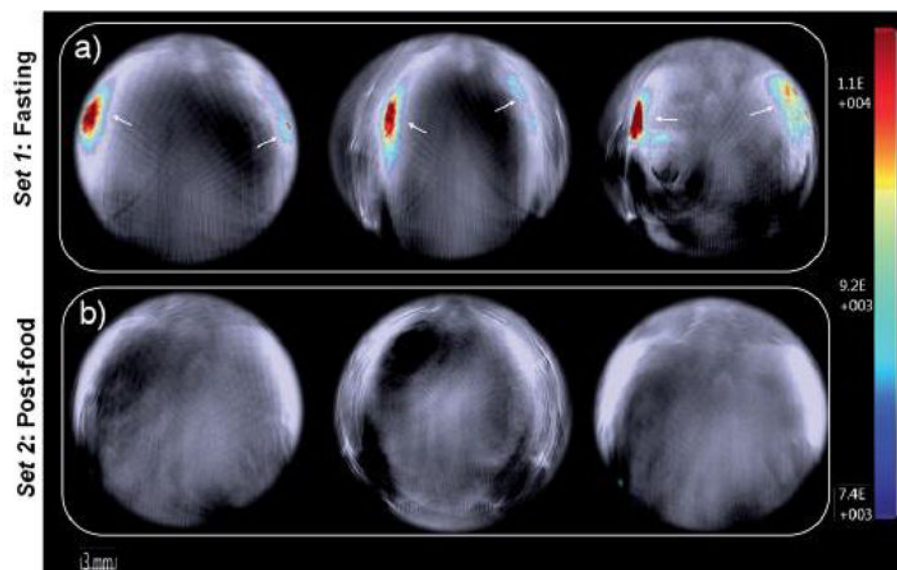
Figure 21.
PAI of live mouse anatomy 40 min post-injection of **34** for (a) fasting and (b) post-food mice. Negligible signals indicate the formation of **34**–thiol adducts in vivo. Reproduced with permission from ref. 144. Copyright 2016 Royal Society of Chemistry.

(36)
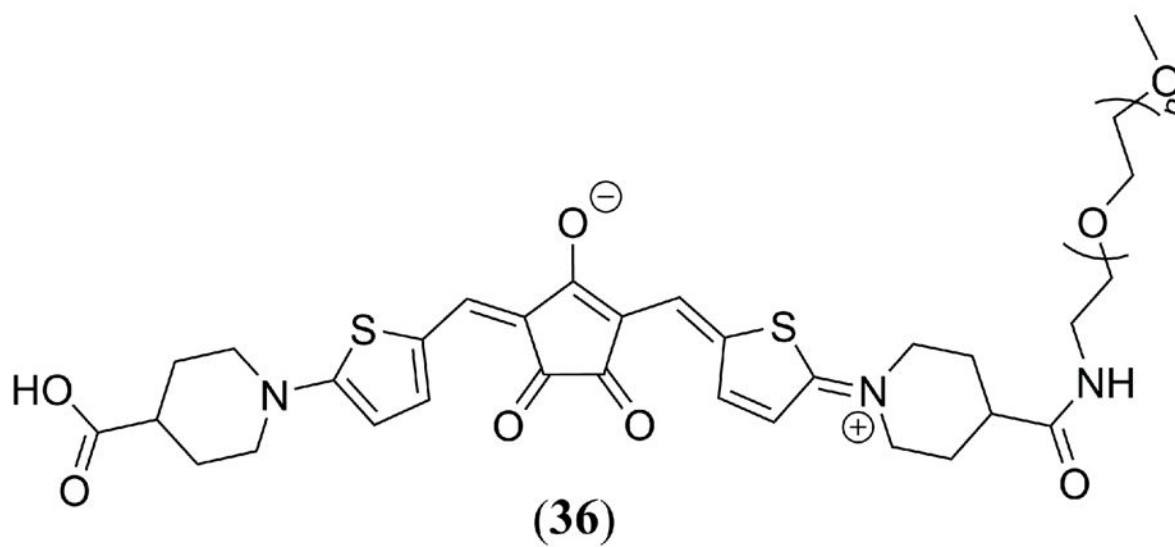
Figure 22.
Molecular structure of the PEG-ylated 2,5-bis[(4-carboxylic-piperidylamino)thiophenyl]-croconaine (**36**) dye used Tang et al. (151) for nanoparticle self-assembly and in vivo PAI studies.
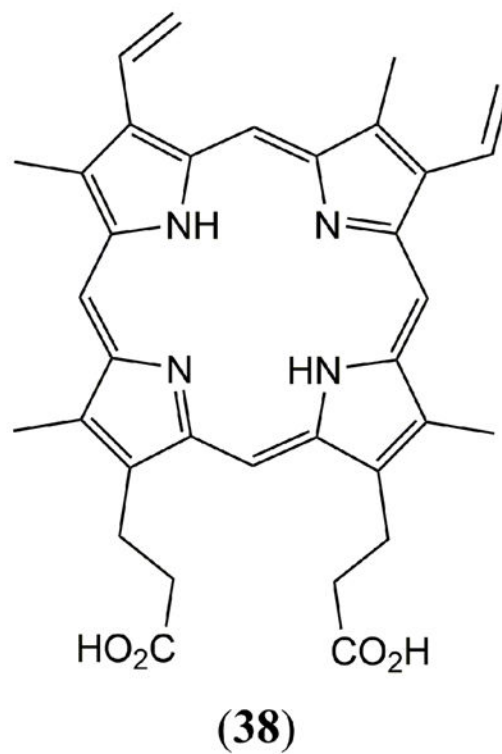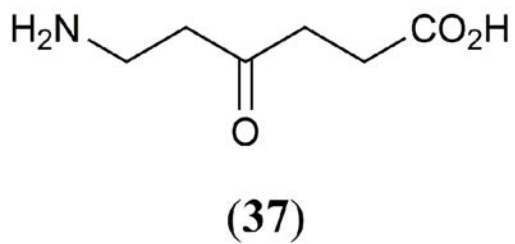
Figure 23.
Molecular structures of δ-aminolevulinic acid (**37**) and protoporphyrin IX (**38**).
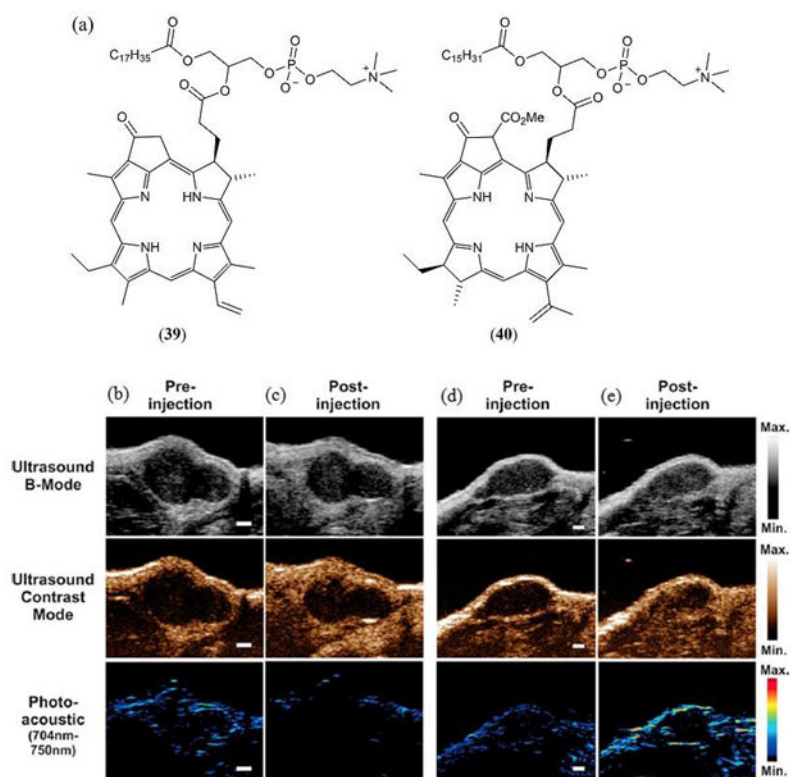
Figure 24.
(a) Molecular structures of the porphyrin–phospholipid conjugates **39** investigated by Lovell et al. (167), Jin et al. (168), Ng et al. (169) and **40** investigated by Huynh et al. (101, 170); (b - e) In vivo imaging in a KB tumor xenograft 10–30 seconds post intravenous injection of bimodal (b, c) and trimodal (d, e) microbubbles derived from **40**. US B-mode images show the soft tissue contrast of the tumor, US contrast mode and PA images illustrate the infusion of microbubbles (Scale bar 1 mm). Reproduced with permission from ref. 170. Copyright 2014 American Chemical Society.
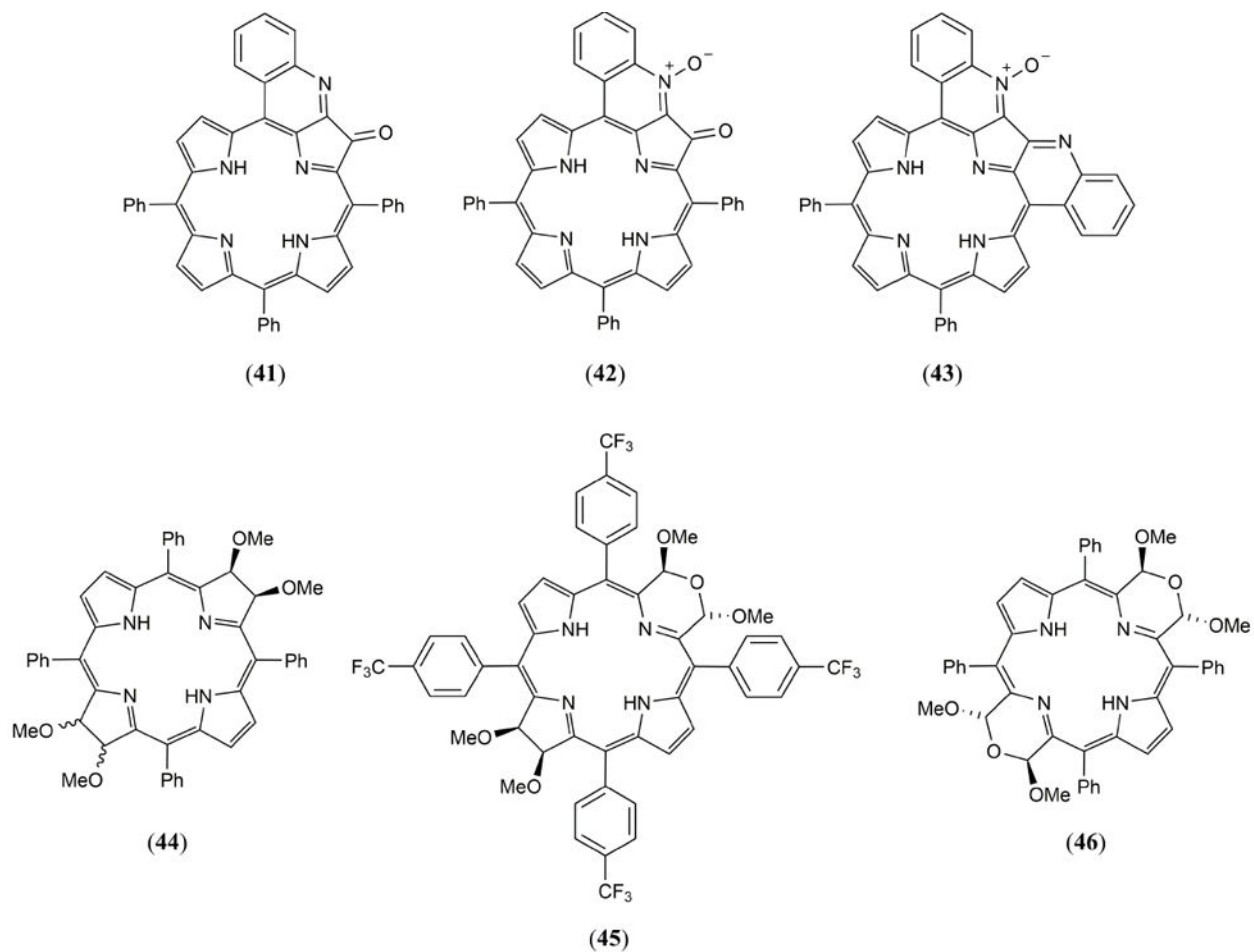
Figure 25.
Molecular structures of the quinoline-annulated porphyrin and morpholino bacteriochlorin based MPACs **41** - **46** reported by Abuteen et al. (175).
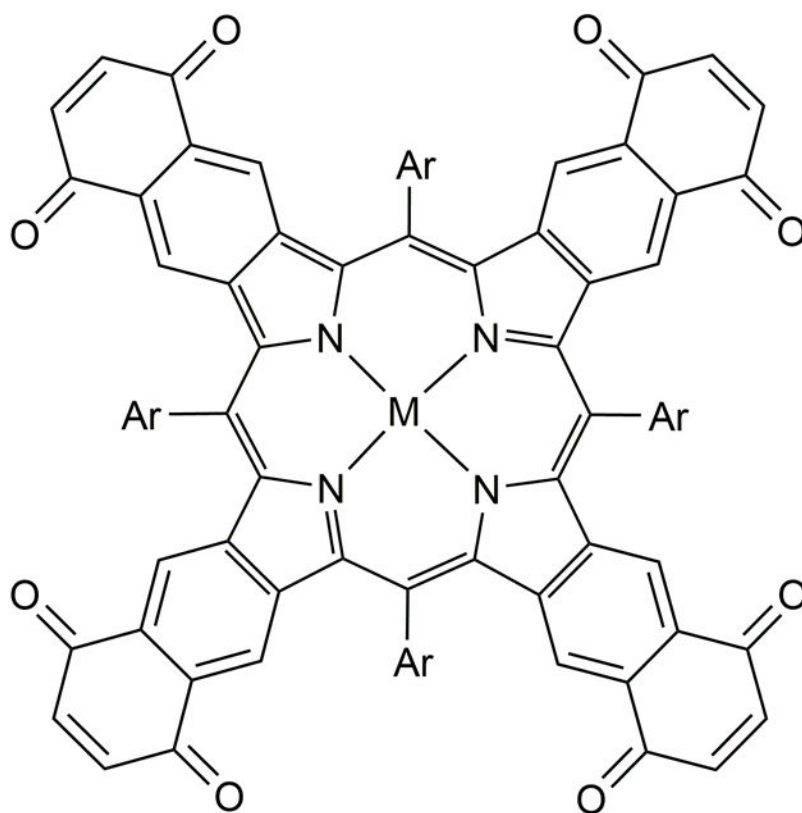
Figure 26.
Molecular structures of the metallated quinone-fused porphyrin MPACs reported by Banala et al. where M = Co(II) (**47**), Ni(II) (**48**), Cu(II) (**49**) or Zn(II) (**50**) (176).
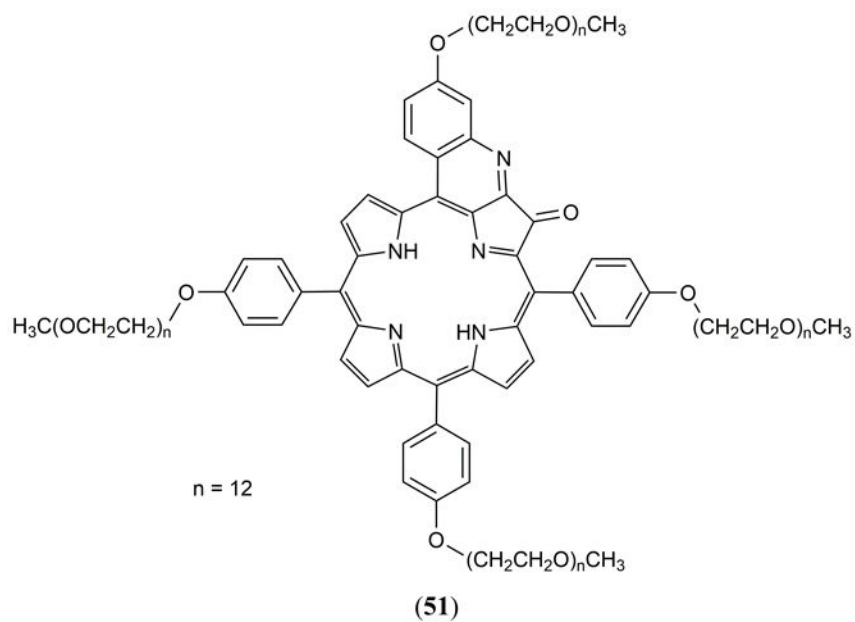
Figure 27.
Structure of the water soluble NIR absorbing tetra-PEG-ylated quinolone annulated porphyrin **51** reported by Luciano et al. (178, 179).
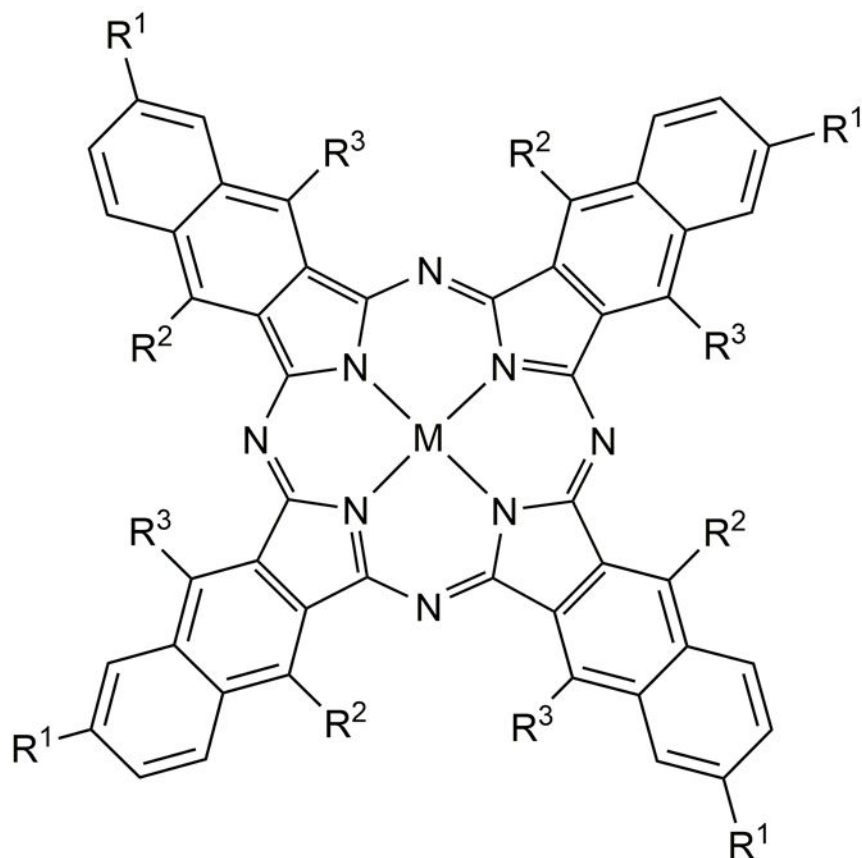
Figure 28.
Structures of the naphthalocyanine dyes studied by Lee et al. (180) and Zhang et al. (180)
where M = Zn, R^1 = t-Bu; R^2 = H (**52**) and M = 2H, R^1 = H; R^2 = O-$(CH_2)_3CH_3$ (**53**).
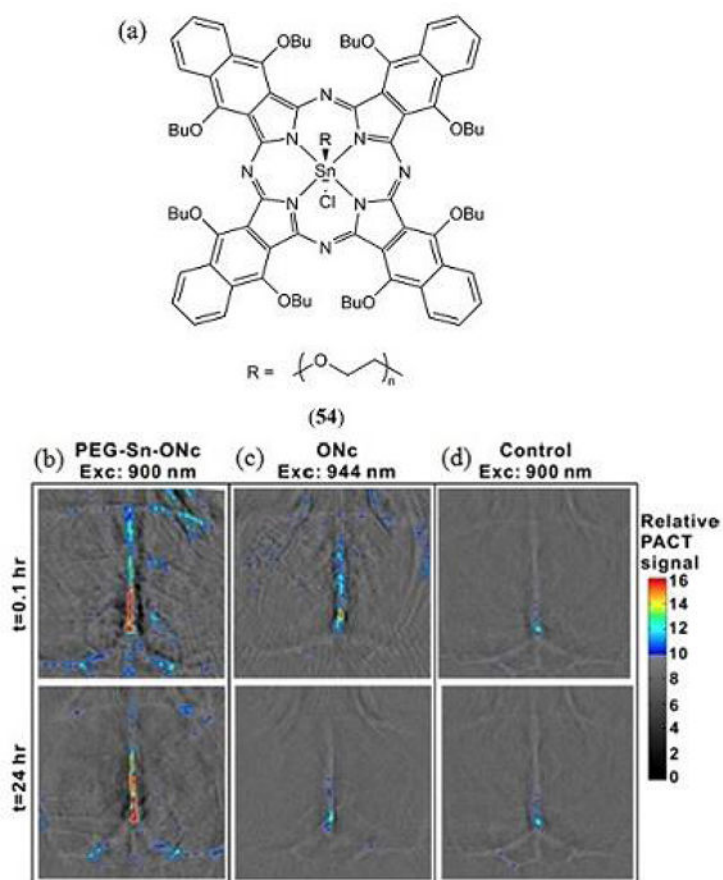
Figure 29.
(a) Structure of the PEG-ylated tin(IV) chloride octabutoxynaphthalocyanine (PEG-Sn-ONc, **54**) reported by Huang et al. (100); (b – d) Noninvasive PA computed tomography (PACT) images of brain blood vessels of mice administered with (b) **54** (c) the non-PEG-ylated derivative ONc and (d) a blank control, 1 h and 24 h post-injection. Reproduced with permission from ref. 100. Copyright 2016 American Chemical Society.
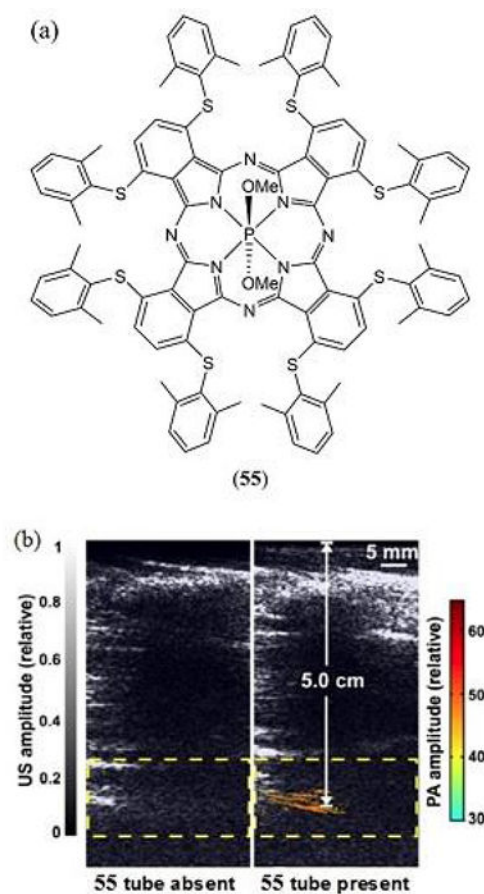
Figure 30.
(a) Molecular structure of the phosphorous phthalocyanine based MPAC **55** utilized for PAI by Zhou et al. (181); (b) Trans-limb PA computed tomography (PACT) for 2 different adult human volunteers with overlaid PA (color) and US (gray) images. Reproduced with permission from ref. 181. Copyright 2016 Ivyspring International Publisher.
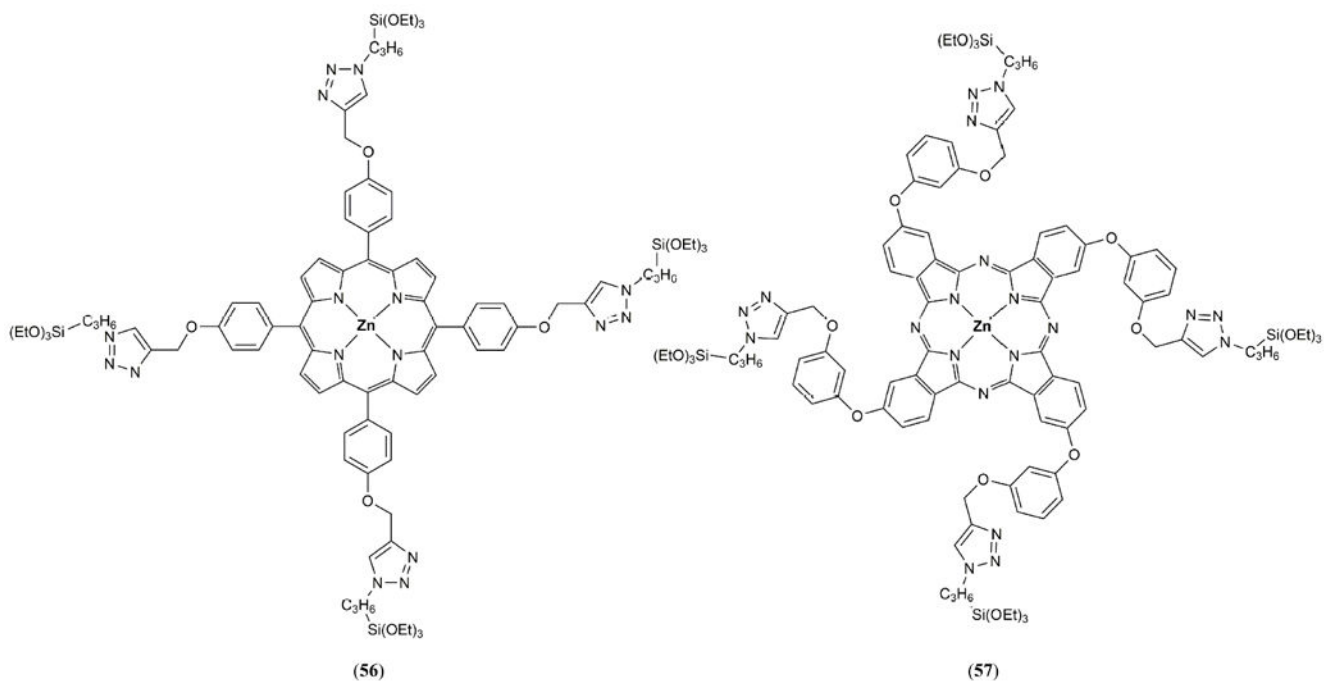
Figure 31.
Molecular structures of monomeric porphyrin (**56**) and phthalocyanine (**57**) dyes utilized for silsesquioxane bridged nanoparticle synthesis by Mauriello-Jimenez et al. (183).
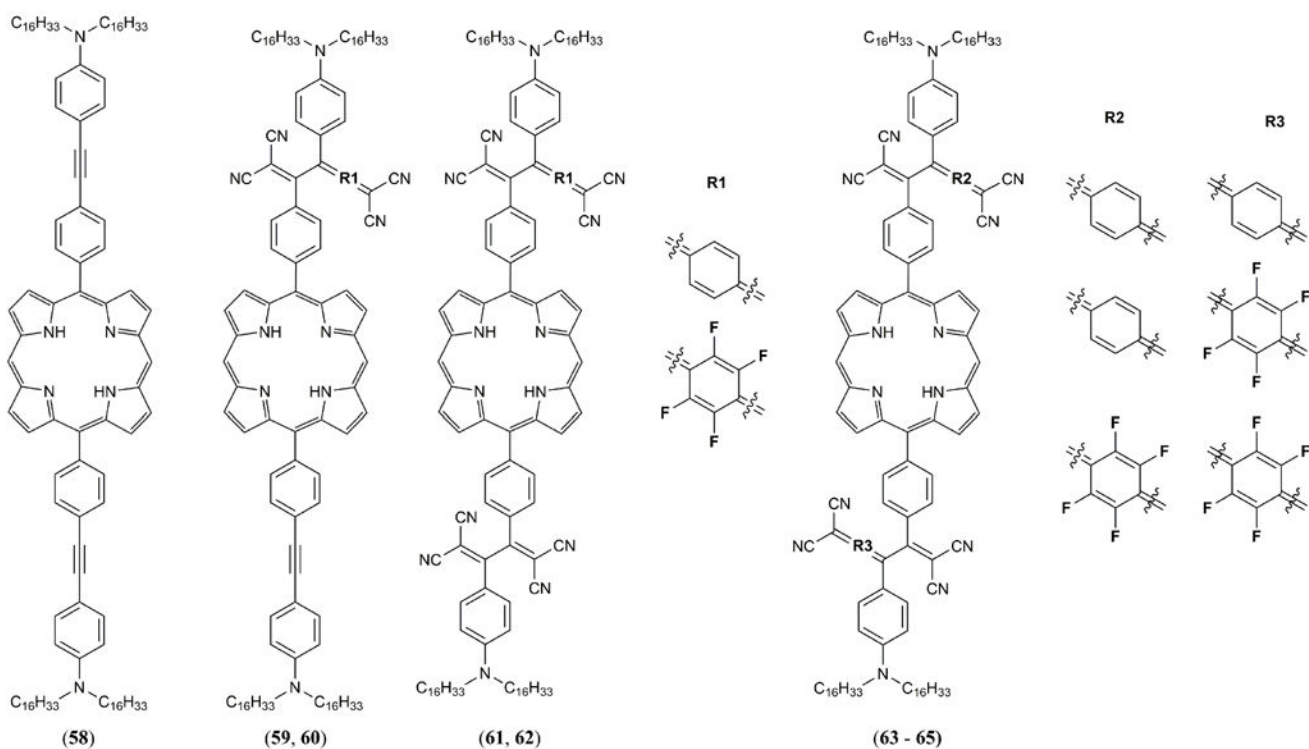
Figure 32.
Structures of the NIR absorbing free-base porphyrin derivatives **58** – **65** reported by Li et al. using the tetracyanoethene(TCNE), 7,7,8,8-tetracyanoquiodimethane (TCNQ) and 2,3,5,6-tetrafluoro-7,7,8,8-tetracyanoquiodimethane (F_4-TCNQ) electron-withdrawing click-reagents (184).
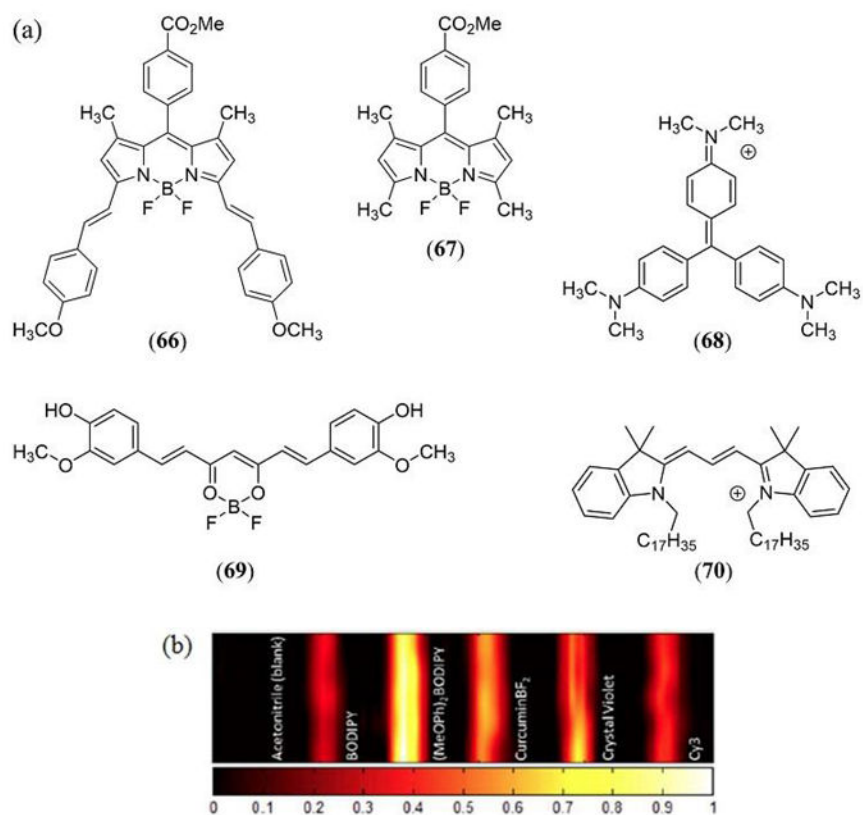
Figure 33.
(a) Structures of the 3,5-bis-styryl (MeOPh)$_2$BODIPY dye **66**, the non-styryl *meso*-(4-methoxycarbonylphenyl)BODIPY analogue **67**, crystal violet (**68**), curcuminBF$_2$ (**69**) and Cy3 (**70**) investigated by Frenette et al. (36). (b) PAI (dimension = 26.40 mm × 6.65 mm) of the same dyes recorded with a 10 MHz US transducer following 532 nm laser irradiation at a fluence of 366 mJ cm^{-2}. Samples are dissolved in acetonitrile in sealed glass capillary tubes (1 mm internal diameter) housed in a room temperature water bath. The color scale represents the normalized acoustic intensity. Reproduced with permission from ref. 36. Further permissions related to the material excerpted should be directed to the American Chemical Society (https://pubs.acs.org/doi/abs/10.1021%2Fja508600x).
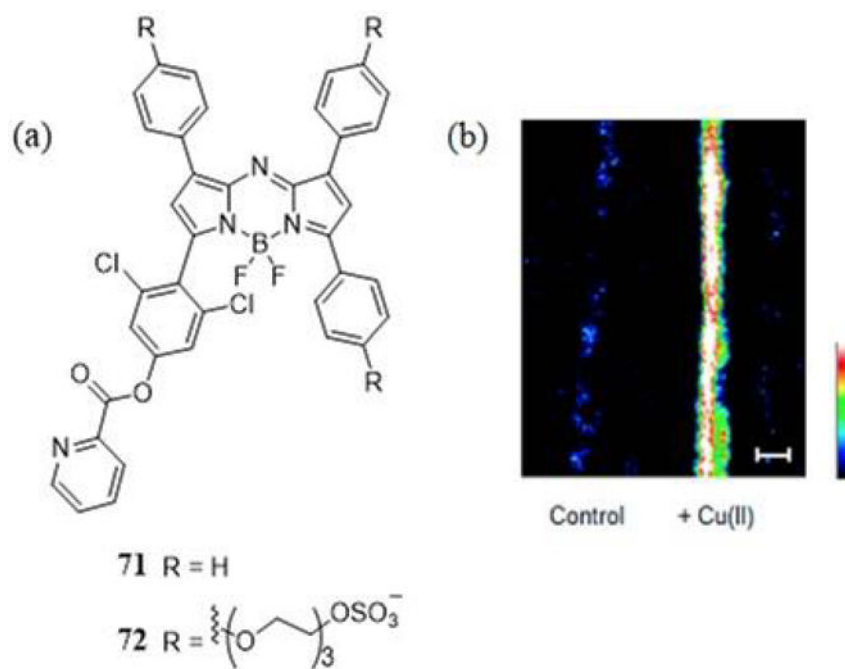
Figure 34.
(a) Molecular structures for the ratiometric aza-BODIPY PA responsive Cu(II) probes reported by Li et al. (185). (b) PA images of **72** (10 μM in PBS + 0.1% Cremophor EL, pH 7.4) in fluorinated ethylene propylene tubing overlaid with a 1 cm thick phantom treated with 0 and 10 equiv of Cu(II), with excitation at 767 nm. Highest and lowest intensity PA amplitudes are indicated by white and black, respectively. Scale bar represents 2 mm. Reproduced with permission from ref. 185. Copyright 2015 American Chemical Society.
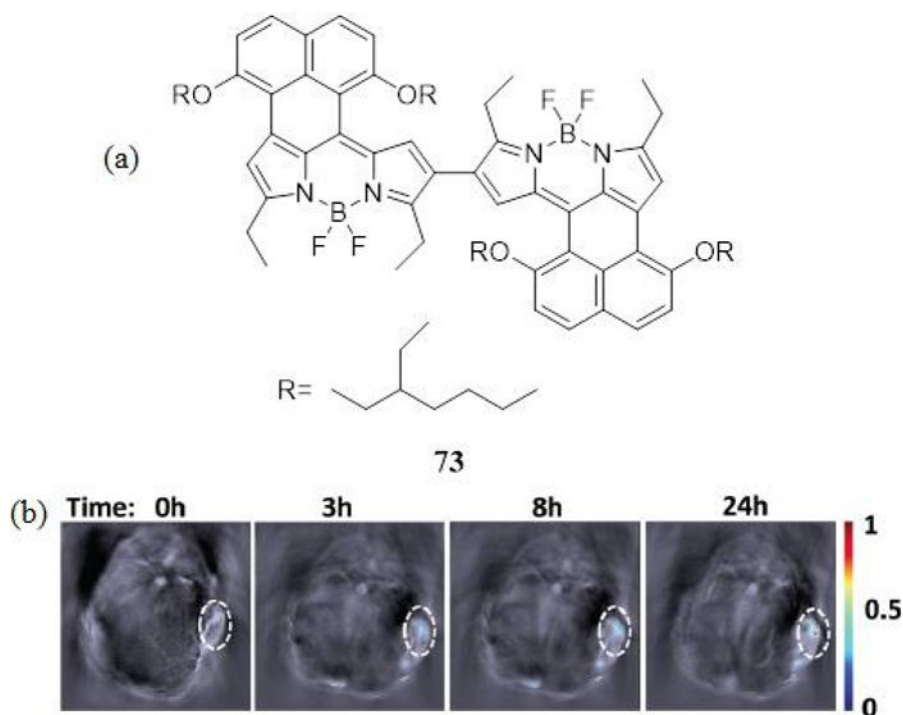
Figure 35.
(a) Structure of the NIR absorbing naphthalene fused BODIPY dimer **73** reported by Ni et al. that demonstrated high photostability and a greater PA response than the ICG cyanine dye (186). (b) Time-dependent in vivo PA images of a Hep-G2-tumor bearing mouse anatomy after intravenous injection of **73** loaded (2.5 WT%) BSA nanoparticles. Reproduced with permission from ref. 186. Copyright 2016 Royal Society of Chemistry.

Figure 36.
Structures of the NIR absorbing 3,5-bis(vinylaryl) BODIPY dyes reported by Ni et al. (187).
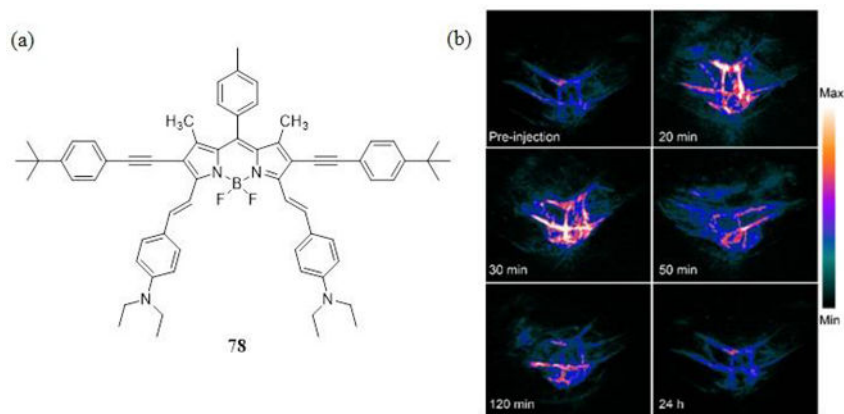
Figure 37.
(a) Structure of the 2,6-bis-ethynyl 3,5-bis-vinyl-4-diethylaminophenyl BODIPY dye **78** used as a PAI based theranostic agent reported by Hu et al. (188). (b) In vivo PAI of A549 tumor-bearing mice at a different times after intravenous injection of **78** doped micelles. Reproduced with permission from ref. 188. Copyright 2016 American Chemical Society.
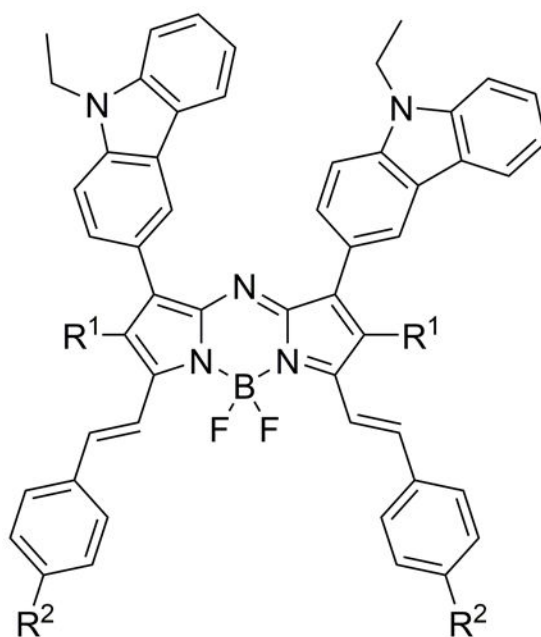
Figure 38.
Structures of the 1,7-bis(*N*-ethylcarbazole)-3,5-bis(vinylphenyl) halogen substituted aza-BODIPY dyes **79** - **82** reported by Gawele et al. (189).
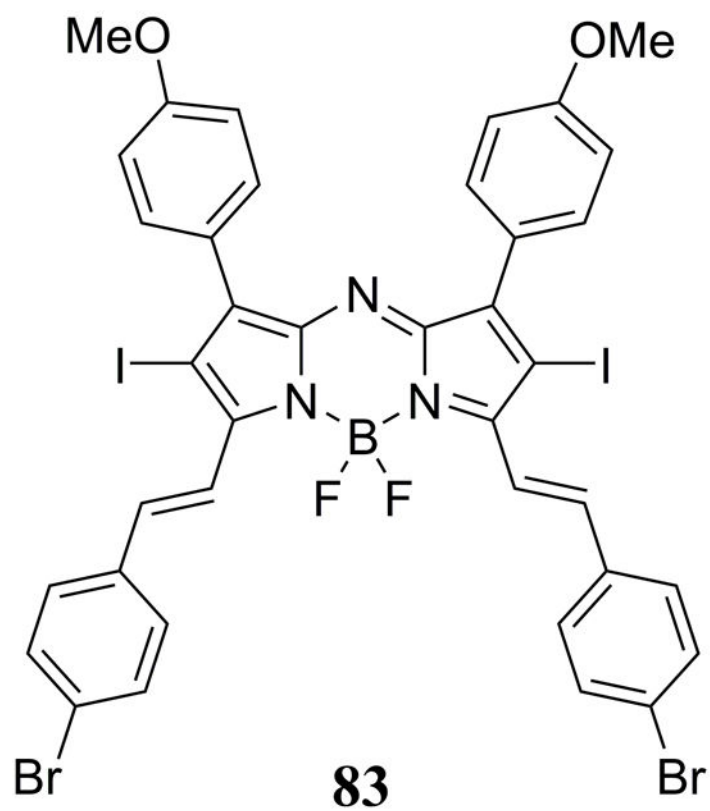
Figure 39.
Structure of the NIR absorbing theranostic aza-BODIPY dye **83** reported by Tang et al. used to prepare micelle nanoparticles for photothermal imaging (PTI), PAI and PDT/PTT studies. (190).
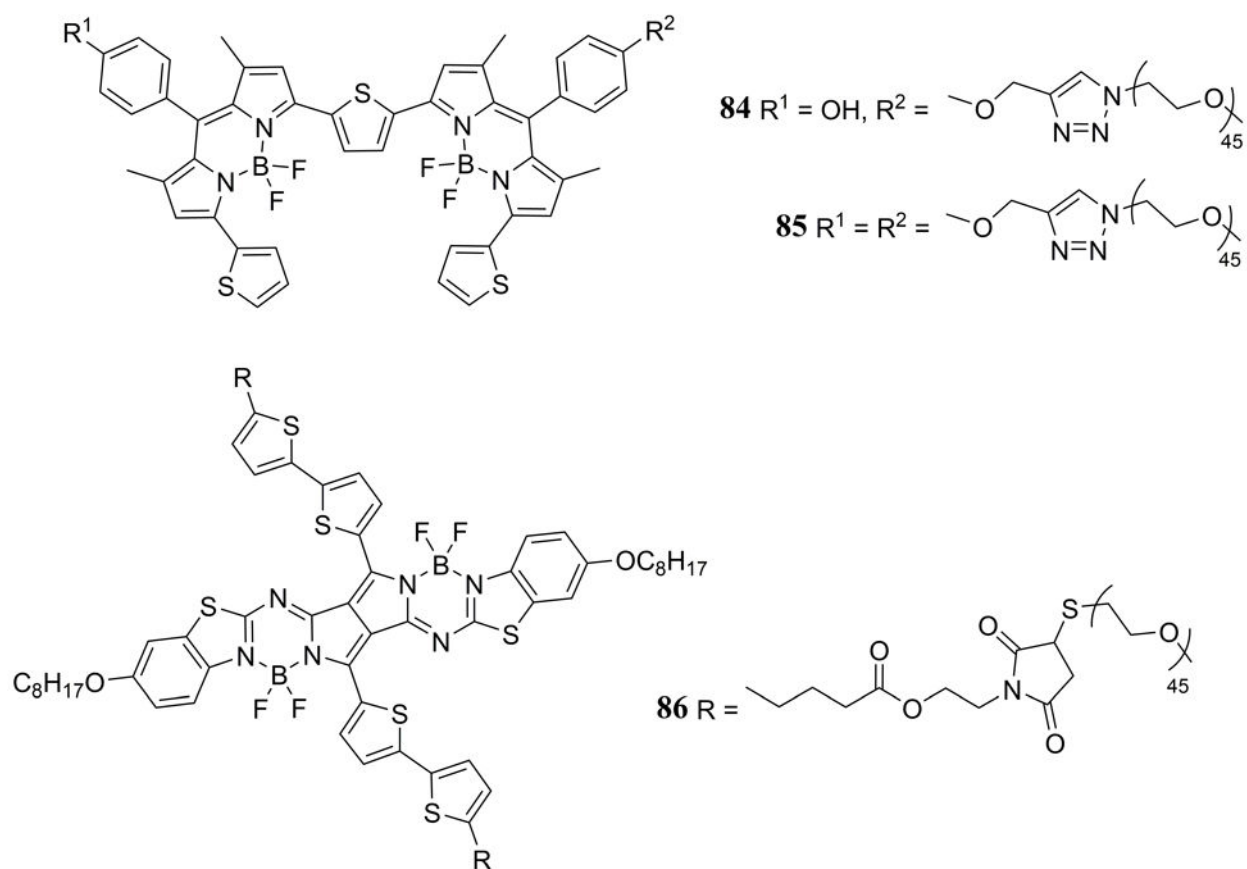
Figure 40.
Structures of NIR absorbing dimeric thiophene-bridged BODIPY (**84**, **85**) and pyrrolopyrrole aza-BODIPY (**86**) dyes reported by Miki et al. (191).
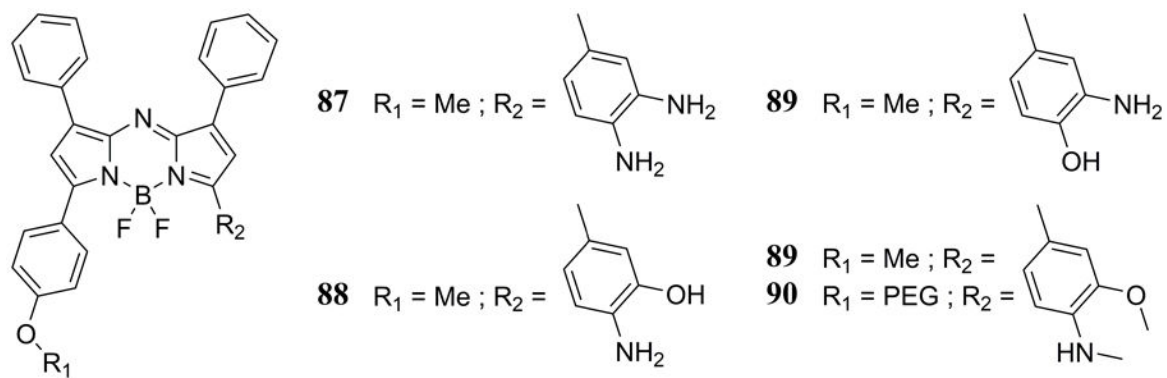
Figure 41.
Molecular structures of the PA nitric oxide probes reported by Reinhardt et al. (192).
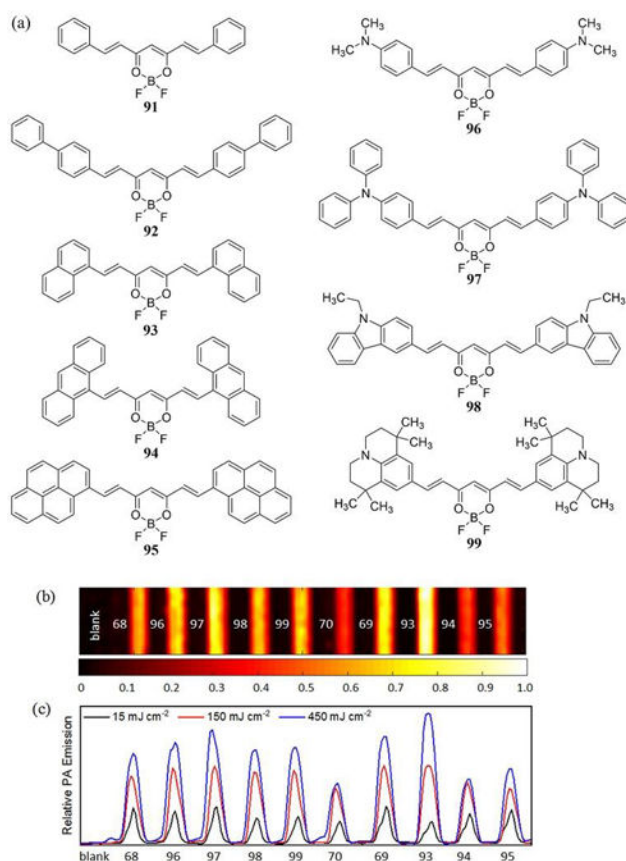
Figure 42.
(a) Molecular structures of difluoroboron curcumin dyes **91** - **99** reported by Bellinger et al. where a nonlinear *reverse saturable absorber* (*RSA*) PA response was tuned by modification of the terminal substituent (194). (b) PAT image recorded with a high laser fluence (450 mJ cm^{-2}, λ_{exc} = 532 nm) and a 10 MHz US transducer including a solvent blank, crystal violet (**68**), curcuminBF$_2$ (**69**) and Cy3 (**70**) for reference. Samples are dissolved in acetonitrile in sealed glass capillary tubes (1 mm internal diameter) housed in a room temperature water bath. The color scale represents the normalized acoustic intensity. (c) Plot of PAT amplitudes for all dyes at low (15 mJ cm^{-2}), intermediate (150 mJ cm^{-2}) and high (450 mJ cm^{-2}) laser fluence illustrating the *linear absorber* (*LA*), *saturable absorber* (*SA*), and *RSA* behavior.
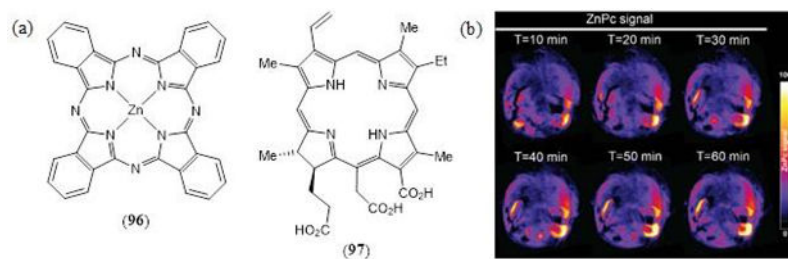
Figure 43.
(a) Molecular structures of the zinc(II) phthalocyanine (**96**) and chlorin e6 (**97**) studied by Ho et al. (140) (b) Time lapse of PAI within 1h post injection of **96** in a MCF-7 xenograft mice model, demonstrating peak localization of **96** at the tumor site. Reproduced with permission from ref. 140. Copyright 2016 Macmillan Publishers Limited.
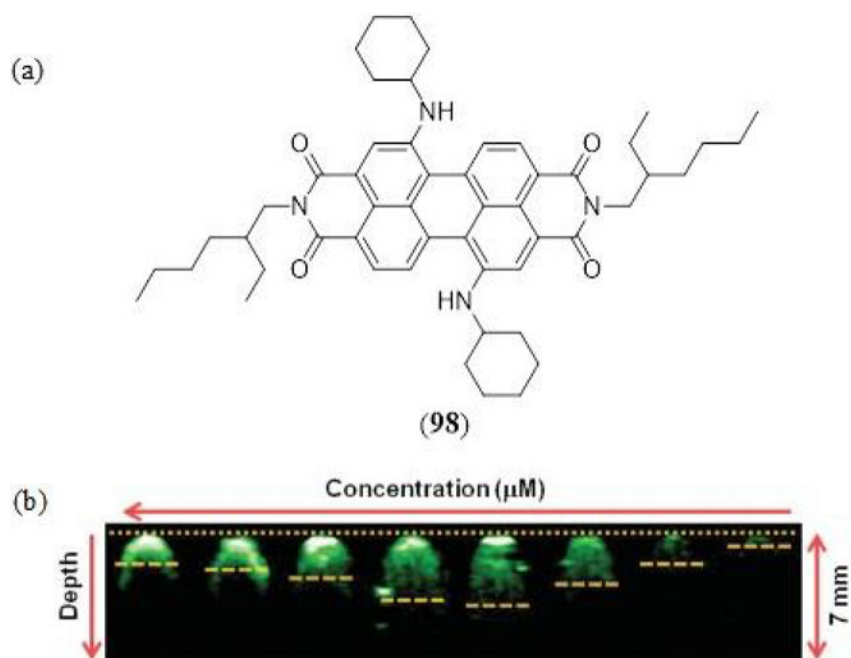
Figure 44.
(a) Structure of the NIR absorbing perylene diimide MPAC reported by Fan et al. (196), (b) PAI coronal sections of **98** doped micelles with different concentrations (50 to 0.390625 nM) in agarose gel phantoms.
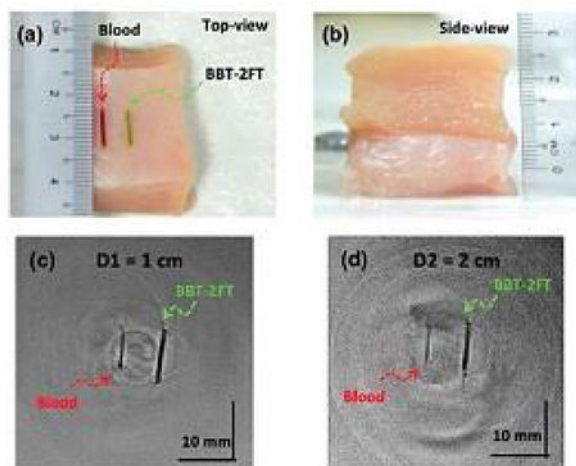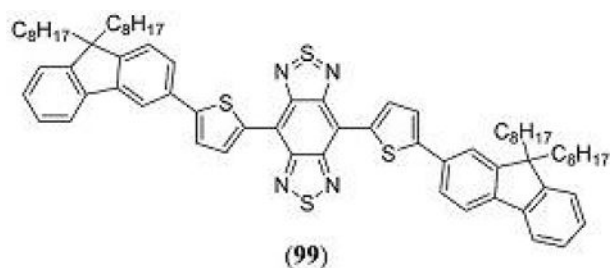
Figure 45.
Structure of the benzobisthiadiazole dye, encapsulated in a β-caprolactone derived amphiphilic block polymer PEG-*b*-PCL micelle by Huang et al. to for PAI and PTT applications (197). Photograph of LDPE tubes with blood and BBT-2FT (a) on chicken tissue, (b) inside a stack of chicken tissue layers, (c) PAI acquired using a 2.25 MHz transducer at 1 cm and (d) 2 cm depth. Reproduced with permission from ref. 197. Copyright 2016 Royal Society of Chemistry.

(100) R = H,
(101) R = N(C$_4$H$_9$)$_2$
(102) R = C$_5$H$_{11}$
(103) R = CHO
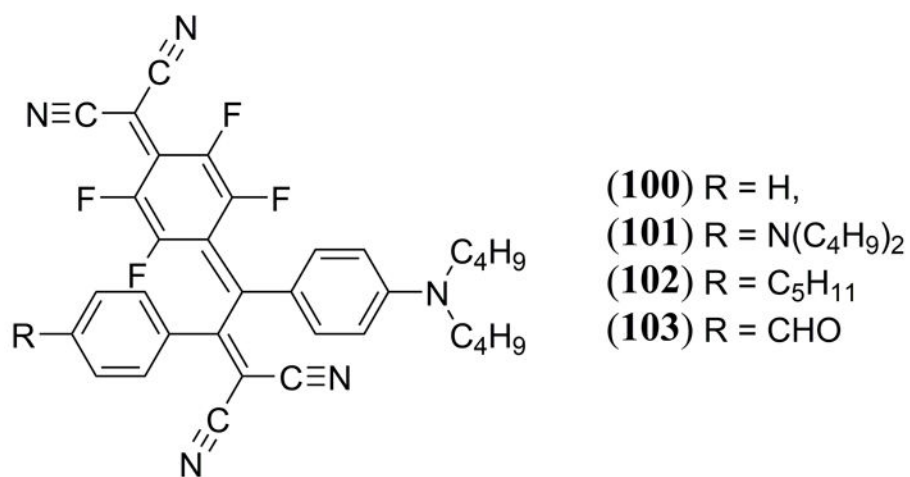
Figure 46.
Structures of the diphenylacetylene click-derived dyes used in tandem with the F$_4$-TCNQ electron-acceptor by Li et al. to tune PA and photothermal properties (198).
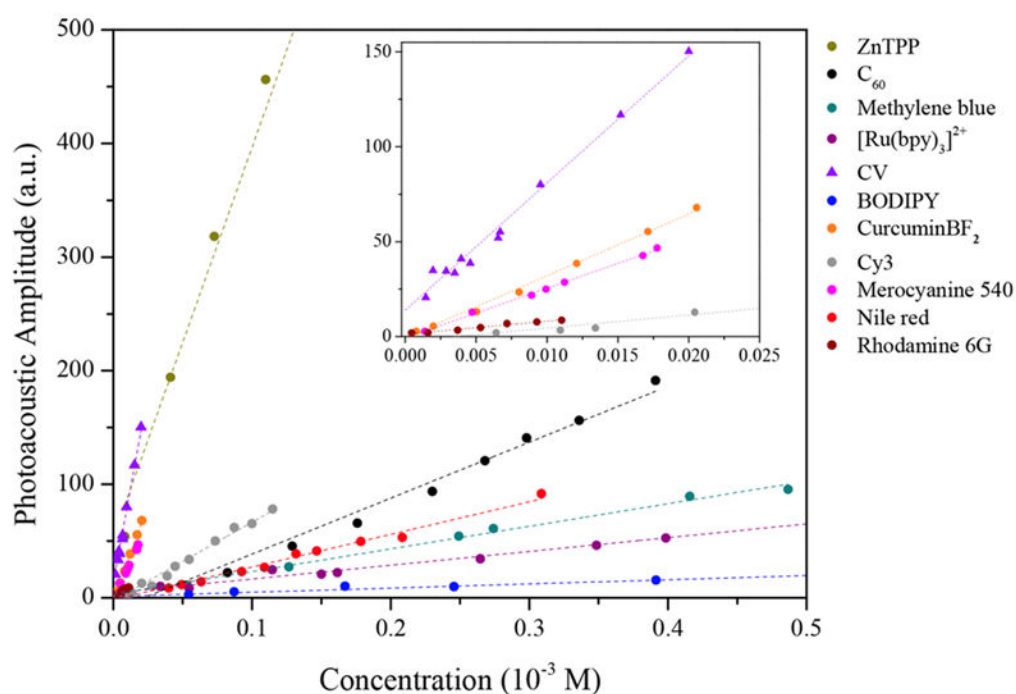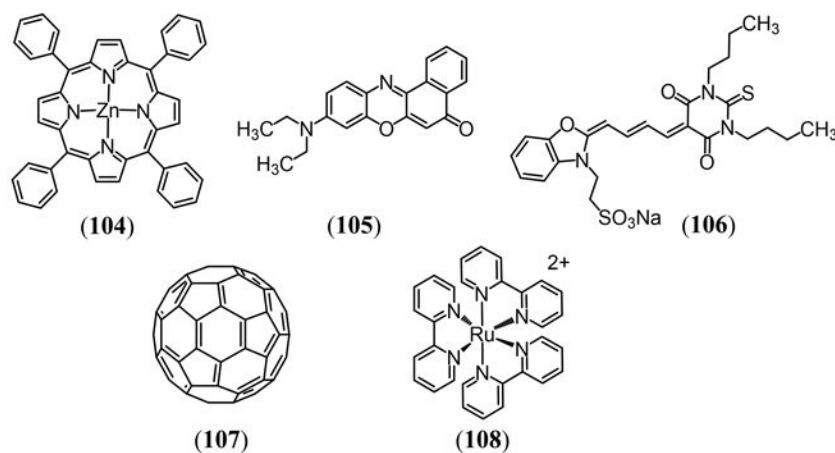
Figure 47.
(a) Molecular structures of the additional MPACs investigated by Hatamimoslehabadi et al. including zinc(II) *meso*-tetraphenylporphyrin (**104**), nile red (**105**), merocyanine 540 (**106**), C$_{60}$ (**107**) and ruthenium tris(2,2'-bipyridine) (**108**). (b) PA emission of all MACs investigated by Hatamimoslehabadi et al. in tetrahydrofuran as a function of concentration measured at a high laser fluence (360 mJ cm^{-2}, λ_{exc} = 532 nm) (199). Reproduced with permission from ref. 199. Copyright 2017 American Chemical Society.
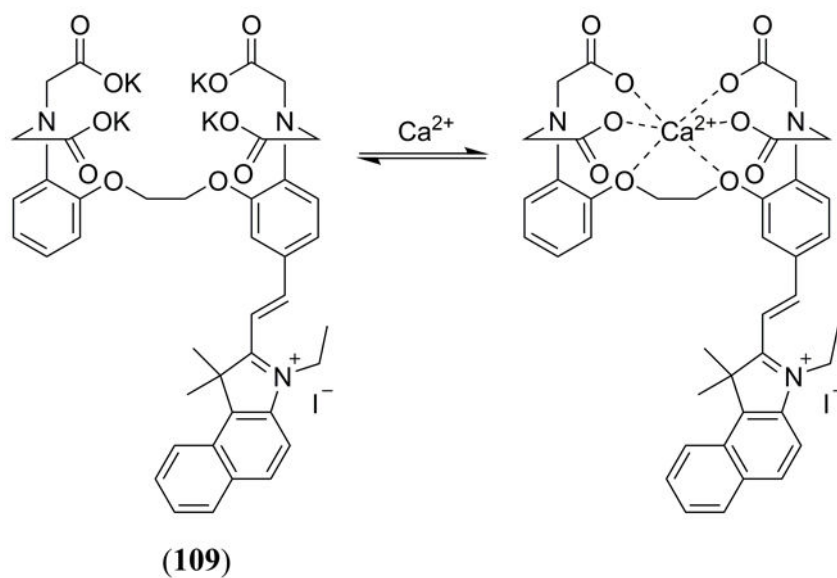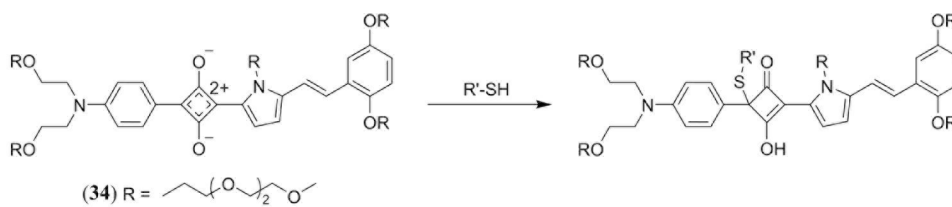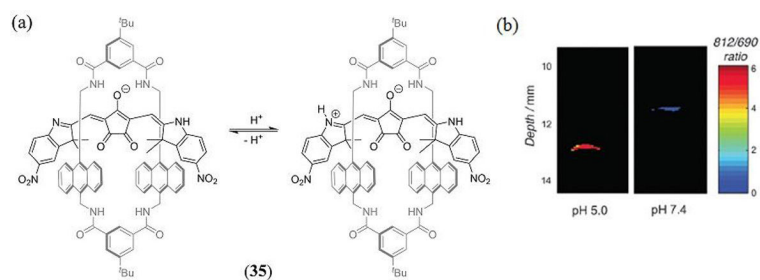
(109)

Figure 48.
Structures of the cell-permeable BAPTA-merocyanine-based PA calcium sensor (**109**)
reported by Roberts et al. (200).

Scheme 1.

Thiol addition at the cyclobutene ring of the NIR absorbing squaraine **34** reported by Anees et al. for bimodal fluorescene and PA detection of biologically relevant thiols (144).

Scheme 2.
(a) Acid-based equilibrium of the pH sensitive, rotaxane encapsulated, croconaine dye **35** reported by Guha et al. (149); (b) Ratiometric PA images of two **35** containing phantoms in pH 5.0 and pH 7.4 buffer at 11–13 mm depth in light scattering media. Reproduced with permission from ref. 149. Copyright 2016 Royal Society of Chemistry.